LENNART CHRISTIAAN KARSSEN

TRAPPING COLD ATOMS WITH ULTRASHORT LASER PULSES

Karssen, Lennart C.

Trapping cold atoms with ultrashort laser pulses
L.C. Karssen - Utrecht
Universiteit Utrecht
Faculteit Bètawetenschappen
Departement Natuur- en Sterrenkunde
Thesis Universiteit Utrecht - With a summary in Dutch
ISBN: 978-90-393-4906-9
Subject heading: atomic physics / laser cooling and trapping /
ultrashort laser pulses
Druk: PrintPartners Ipskamp, Enschede

TRAPPING COLD ATOMS WITH ULTRASHORT LASER PULSES

Koude atomen vangen met behulp van ultrakorte laserpulsen

(met een samenvatting in het Nederlands)

PROEFSCHRIFT

ter verkrijging van de graad van doctor
aan de universiteit utrecht op gezag van
de rector magnificus, prof.dr. j.c. stoof,
ingevolge het besluit van het college voor promoties
in het openbaar te verdedigen
op woensdag 8 oktober 2008
des middags te 2:30 uur

door

lennart christiaan karssen

geboren op 25 november 1977 te Harderwijk

Promotoren: Prof.dr. J.I. Dijkhuis
Prof.dr. P. van der Straten

This work is part of the research programme of the 'Stichting voor Fundamenteel Onderzoek der Materie (FOM)', which is financially supported by the 'Nederlandse Organisatie voor Wetenschappelijk Onderzoek (NWO)'.

CONTENTS

1

INTRODUCTION

1.1 COLD ATOMS

In 1970 Ashkin showed that small particles could be accelerated and trapped by the radiation pressure from a continuous-wave laser, the so-called optical tweezers [1]. Later that year he proposed a similar setup for atoms by using near-resonant light [2]. Approximately half a year after I was born Ashkin proposed a three-dimensional trap for neutral atoms based on two couterpropagating focused laser beams [3]. In the same paper he also described the simplest optical dipole trap: one focused Gaussian TEM_{00} laser beam. Later that year Bjorkholm et al. [4] demonstrated the optical dipole force by deflecting and focusing a beam of sodium atoms. It is this optical dipole force that stands at the heart of the atom trap discussed in this thesis.

The field of trapping and cooling of neutral atoms by optical means culminated in 1987 with the paper by Raab et al. on the magneto-optical trap (MOT), in which atoms can both be cooled and trapped [5]. Using this technique it became possible to store atoms at temperatures in the microKelvin range allowing for novel high-resolution experiments, like the atomic clocks based on a fountain of cold atoms. In 1997 the Nobel prize was awarded to S. Chu, C. Cohen-Tannoudji and W.D. Philips "for development of methods to cool and trap atoms with laser light". Using evaporative cooling in a magnetic trap loaded from a MOT resulted in the first experimental observation of a Bose-Einstein condensate (BEC) by Anderson et al. [6], which resulted in the 2001 Nobel prize being awarded to E.A. Cornell, W. Ketterle and C.E. Wieman "for the achievement of Bose-Einstein condensation in dilute gases of alkali atoms, and for early fundamental studies of the properties of the condensates". Later BEC was reached in an all-optical manner by loading atoms in a crossed dipole trap [7]. Recently, a trap for neutral atoms based on ac electric fields has been shown [8].

From these ideas and experiments emerged several fields of physics, including Bose-Einstein condensation, degenerate Fermi gases, atom optics, optical lattices, and quantum information.

Optical dipole traps (ODTs) are based on the off-resonance ac Stark shift of the

atomic levels in an inhomogeneous laser light field, in contrast to laser cooling that relies on the scattering of near resonant photons. In 1986 Chu et al. loaded their cold atoms into an ODT detuned only several hundred GHz from resonance [9]. Depending on the magnitude of the detuning ODTs are classified into far-off-resonance traps (FORTs) [10] or quasi-electrostatic traps (QUESTs) [11, 12]. FORTs are usually made at a detuning of several nanometers to a few hundreds of nanometers; QUESTs are operated at a much larger detuning.

1.2 ULTRAFAST LASERS

Ultrafast lasers, i. e. lasers that generate very short pulses of 10^{-12}–10^{-15} s, are a useful tool in many physics and chemistry experiments [13–16]. The first laser, built in 1960, was pulsed [17]. It used a strong flash lamp to create population inversion in the gain medium. However, modern pulsed lasers are usually mode-locked lasers [18]. In a mode-locked (ML) laser the phases of the longitudinal modes are locked, which leads to repetitive constructive interference and pulses spaced by the round-trip time of the laser cavity. Using mode-locking to generate pulses has the advantage of leading to extremely short pulses. Recently pulses of several hundred attoseconds (10^{-18} s) have been produced using X-rays, since such pulses are shorter than one optical cycle in visible light [19, 20].

Ultrafast lasers have also found applications in atomic physics. Frequency combs, for example, earned J.L. Hall and T.W. Hänsch their Nobel prize in 2005 [21–24]. Furthermore, ultrashort pulses have been used for cold molecule formation [25–27], coherent control [28, 29], frequency measurements in cesium and calcium [30, 31] and other experiments [32–35].

This thesis aims to describe the physics that arises from combining the fields of ultrashort pulses with traps for ultracold atoms. Previous work showed the deceleration and cooling of an atomic beam using ML lasers for pulse durations down to picoseconds [36–39]. More recently a pulsed standing wave was used to focus an atom beam [40]. One step further is the trapping of atoms using pulsed lasers. In 1995 an optical trap based on two counterpropagating pulsed laser beams was proposed [41]. As a step towards making such a trap we have built a FORT using a picosecond ML laser and will compare the results with a continuous-wave (CW) FORT.

1.3 THESIS LAYOUT

The work described in this thesis is presented as follows. In the next chapter we will explain some of the choices made when setting up this research project. In Chapter 3 the basics of laser cooling and trapping will be reviewed. Chapter 4 gives a detailed description of our experimental setup. A detailed comparison of the FORTs made with a CW and a ML laser is presented in Chapter 5, followed by

a chapter on the parametric excitation of atoms in a FORT. Chapter 7 describes the measurements of the dependency of the number of trapped atoms on the polarisation of the trapping laser light.

Appendix A shows details of the calculation of the minimum beam waist from two measurements at different positions, and Appendix B provides a summary of characteristic data of rubidium for easy reference.

The appendices are followed by a table of acronyms used in this thesis (in the electronic version of this work these acronyms are clickable links) and a table that lists the most used-symbols and their meaning.

2

MOTIVATION

In this chapter we will explain our motivation for performing the research presented in this thesis. The heart of this work is formed by the comparison of a far-off-resonance trap (FORT) made with a continuous-wave (CW) laser with one made using a mode-locked (ML) laser. The element of choice is rubidium.

2.1 WHY A PULSED TRAP?

The idea that lies at the origin of this research is that of the interaction of so-called π-pulses and atoms, which was already proposed by Kazantsev in the era before laser cooling [42]. The concept of a π-pulse can be traced back to the world of magnetic resonance, where the formalism of the Bloch vector and the Bloch sphere was developed.

For a phenomenological description of this idea consider the 1D model of a two-level atom moving in the field of two counterpropagating laser beams with wave vector $\boldsymbol{k}_\pm$ ($|\boldsymbol{k}_+| = |\boldsymbol{k}_-| = k$) tuned close to the atomic resonance. In the case of CW lasers this setup is identical to the setup used to create optical molasses (cf. § 3.3.1) in which atoms can be cooled to mK level, but not trapped. The maximum force that can be exerted on the atom in optical molasses is limited by the rate at which photons can be absorbed and it saturates at $\hbar k\gamma/2$, where γ is the natural linewidth of the transition.

If the lasers are replaced by ML lasers with a Rabi frequency $\Omega(t)$, the pulse envelope area θ can be defined as

$$\theta \equiv \int \Omega(t)\,\mathrm{d}t, \tag{2.1}$$

where the integration is performed over the duration of one pulse. If the parameters of a laser are set such that $\theta = \pi$, it emits so-called π-pulses. A π-pulse completely excites an atom from the ground state to the excited state and *vice versa*. Furthermore, if the repetition rate of the laser

$$f_{\mathrm{rep}} = \frac{c}{2L}, \tag{2.2}$$

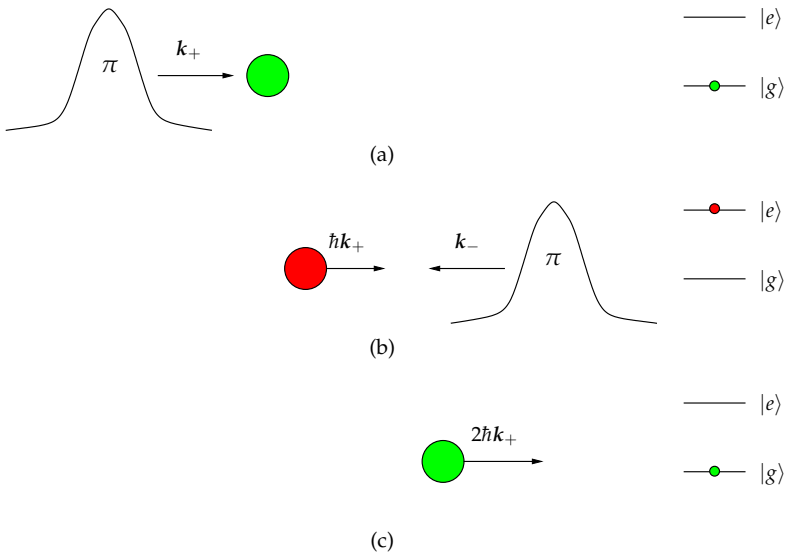

Figure 2.1: Schematic representation of the interactions of counterpropagating π-pulses and an atom. On the right side the levels marked $|g\rangle$ and $|e\rangle$ denote the ground state and the excited state, respectively.

with L the cavity length, is chosen larger than the natural linewidth of the atom, i. e. a repetition time shorter than the lifetime of the transition ($\tau_{\text{rep}} < \tau_{\text{atom}}$), the atom will be hit by the next pulse, before undergoing spontaneous emission.

If the timing of the laser pulses coming from the left and the right is chosen such that they overlap at the centre of the trap, an atom in the ground state that is initially positioned to the left of the centre will first be 'hit' by a pulse from the left beam, as illustrated in Fig. 2.1a. Since it is a π-pulse the atom will be excited and gain momentum by an amount $\hbar\boldsymbol{k}_+$ (Fig. 2.1b). The pulse from the other direction will then deexcite the atom by stimulated emission, resulting in another momentum gain $-\hbar\boldsymbol{k}_- = \hbar\boldsymbol{k}_+$ and leave the atom in the ground state, ready for another cycle (Fig. 2.1c). Thus after one absorption-emission cycle the atom has gained a total momentum of $2\hbar\boldsymbol{k}$ in the direction towards the centre of the trap. If the atoms crosses $z = 0$, the time ordering of the interactions with the pulses is reversed, and the force is again pointing towards the centre. Since this pulse scheme uses stimulated emission instead of the spontaneous emission used in traditional cooling an trapping experiments, the force is not limited by the natural decay rate of the transition, but by the repetition rate of the laser. Therefore, the force can be much higher than in an optical molasses.

Using a similar scheme with longer pulses atomic beams have been deflected [36–40, 43]. This π-pulse scheme has many similarities with bichromatic cooling demonstrated earlier [44–47].

The work presented in this thesis is an onset to the implementation of this trapping scheme that provides a large, position dependent force. Other advantages of using ML lasers for atom traps include the large frequency spectrum that is available, which may allow more elements to be trapped. The high intensities obtained with ML lasers, in combination with modern efficient frequency doubling and tripling techniques, allows trapping of atoms with transitions in the blue part of the optical spectrum. Furthermore, the high intensities allow for larger trap volumes, since the beam waist can be made larger for a given potential depth. Moreover, since this scheme does not require a closed transition, it could be used to trap molecules as well.

2.2 CHOOSING A TRAP

Most atom traps made using atom optics techniques are made with CW lasers. A rubidium MOT can be made with several mW of laser light, an ODT requires several hundreds of mW. Since we want to study the mechanical effects of ultrashort pulses on cold atoms a way has to be found to monitor these interactions. A FORT is a good candidate for several reasons. First of all it provides long storage times and small losses. Secondly, modelling the behaviour of the atoms in the trap is less complex than in other traps, since a dipole trap is conservative and there is no cooling by the laser light. Furthermore FORTs allow trapping of neutral atoms. Moreover, atoms can be trapped in an arbitrary ground state or spin state, contrary to magnetic traps. Finally, these traps are easily implemented in the lab as well.

2.3 PROPERTIES OF RUBIDIUM

Many chemical elements can be manipulated in atom optics experiments. Hydrogen [48, 49] and noble gasses like neon and helium (in their metastable state) have been used [50–53], as well as more "exotic" elements like ytterbium [54], iron [55] and the radioactive radium [56]. Recently an ODT was used to create an all-optical BEC of chromium [57]. Molecules have been trapped as well, both by starting with molecules [58] and by creating them from laser cooled atoms (cf. e. g. [26, 27, 59–61])

However, alkali metals are used most commonly in laser cooling and trapping experiments. Sodium atoms were used in the optical molasses experiments of Chu et al. [62] and the first MOT [5]. The first BEC was made with rubidium [6]. Furthermore, most alkalis have bosonic and fermionic isotopes, allowing for mixtures of quantum degenerate gases resulting in many new phenomena (cf. e. g. [63–65]). The main reason for choosing alkalis lies in their strong D-lines. These lines are usually within range of modern day's tunable lasers and offer (nearly) closed transitions which are necessary for efficient laser cooling. Further-

more, the D-lines of rubidium, at 795 nm and 780 nm, are compatible with cheap and relatively simple diode lasers.

In our experiments the two naturally occurring isotopes of rubidium are used, both of which are bosons. The only stable one is $^{85}_{37}$Rb with a natural abundance of 72.17 %. The other one is $^{87}_{37}$Rb with a lifetime of $4.88 \cdot 10^{10}$ years, which makes up for the other 27.83 % of naturally occurring rubidium. All other isotopes can only be made synthetically and have decay times ranging from 0.11 s to 86 days [66]. The first MOT with ^{82}Rb was made by Guckert et al. and recently this isotope has been trapped in an ODT [67, 68]. Crane et al. have trapped ^{84}Rb [63]. In 2001 Roberts was the first to Bose-condense ^{85}Rb [69].

Rubidium was discovered in 1891 by Bunsen and Kirchhoff. At room temperature it is a soft silvery metallic solid, but it already melts at 39 °C [70]. It reacts violently with air and water and is usually stored in an inert Ar atmosphere. The vapour pressure of rubidium at room temperature is $5.23 \cdot 10^{-7}$ mbar [70, 71]. A comprehensive list of the properties of rubidium necessary for our experiments is summarised in Appendix B. It includes figures of the hyperfine splittings, transition strengths and tables listing some relevant properties. An even more complete compilation of Rb data can be found in Refs. [72, 73].

3

THEORETICAL CONCEPTS FOR LASER COOLING AND TRAPPING OF ATOMS

The basic theoretical framework necessary to understand the optical forces harnessed in this thesis is presented in this chapter. For extensive coverage of the field consult Refs. [74–76]. For our explanation of the dipole force and the radiation pressure force two different points of view are chosen. For the former a more or less classical approach is taken, whereas for the latter a slightly more quantum-mechanical picture involving photons is used. This is done in order to give the most natural explanation for each of the forces.

3.1 INTRODUCTION

The optical force on atoms caused by the three fundamental processes of photon absorption, spontaneous emission and stimulated emission, is generally separated into two components [77, 78] which will be described in more detail in the next two sections. First, the so-called scattering force or radiation-pressure force, which is based on the absorption and spontaneous emission of photons and therefore related to the imaginary part of the atomic polarisability will be treated. It is only present in optical fields with running wave components, and will be described in § 3.3. This force has a dissipative character and can therefore potentially cool atoms.

The second component of the optical force is usually called the dipole force. It is related to the absorption and stimulated emission of photons. It has a reactive character and is related to the potential energy of the atomic dipole in an ac electric field. It therefore depends on the real part of the polarisability. As will be shown in the following section this component of the optical force attracts atoms to regions of high intensity in case the light is tuned below the atomic resonance.

3.2 OPTICAL DIPOLE TRAPPING

Optical dipole traps (ODTs) are at the heart of the research presented in this thesis. Atoms interacting with a spatially inhomogeneous light field, such as a

focused laser beam, will experience a so-called optical dipole force because of the interaction of the induced dipole moment of the atom with the intensity gradient of the electric field. It is a stimulated effect in which a photon is absorbed from one plane wave component of the light followed by stimulated emission into another component. This redistribution of photons is a reversible process and therefore makes the dipole trap potential a (nearly) conservative one. If the laser frequency is detuned further and further from resonance, the absorption of photons becomes less and less important and the dipole interaction allows for stable traps.

3.2.1 *The classical Lorentz oscillator model*

A simple but accurate model for optical dipole trapping can be constructed using the classical Lorentz oscillator model [75, 76]. In this model one considers a monochromatic linearly polarised electric field $\boldsymbol{E}(\boldsymbol{r},t) = \boldsymbol{E}_0(\boldsymbol{r})\,\mathrm{e}^{-i\omega t} + c.c.$ with $\boldsymbol{E}_0(\boldsymbol{r}) = \hat{\varepsilon}E_0\mathrm{e}^{i\boldsymbol{k}\cdot\boldsymbol{r}}$. When an atom experiences such a driving field a dipole moment $\boldsymbol{d}$ will be induced which will oscillate at the frequency of the field

$$\boldsymbol{d} = \alpha(\omega)\boldsymbol{E}(\boldsymbol{r},t), \tag{3.1}$$

where α is the complex polarisability of the atom. Using its real and imaginary components the interaction can be described as consisting of a potential and a photon scattering rate. The potential energy of the dipole in this electric field is given by

$$\begin{aligned} U_{\mathrm{dip}}(\boldsymbol{r}) &= -\frac{1}{2}\left\langle \boldsymbol{d}\cdot\boldsymbol{E}(\boldsymbol{r},t)\right\rangle && \text{(3.2a)}\\ &= -\frac{1}{2}\Big\langle \big(\boldsymbol{d}+c.c.\big)\cdot\big(\boldsymbol{E}(\boldsymbol{r},t)+c.c.\big)\Big\rangle \\ &= -\mathrm{Re}\,(\alpha)\,|\boldsymbol{E}_0(\boldsymbol{r})|^2 \\ &= -\frac{\mathrm{Re}\,(\alpha)}{2\epsilon_0 c}I(\boldsymbol{r}). && \text{(3.2b)} \end{aligned}$$

Here $I = 2\epsilon_0 c|\boldsymbol{E}_0(\boldsymbol{r})|^2$ is the intensity of the light field, the angular brackets denote the time average which is needed because we are dealing with an ac field, and the terms rotating at twice the frequency are dropped in the time average. The factor $\frac{1}{2}$ in Eq. (3.2a) accounts for the fact that the dipole moment is an induced one and not a permanent one. Equation (3.2b) clearly separates the interaction into a field part ($I(\boldsymbol{r})$) and an in-phase atomic response part ($\mathrm{Re}\,(\alpha)$). From this dipole potential the conservative dipole force can be calculated and, as stated earlier, it is proportional to the intensity gradient:

$$\boldsymbol{F}_{\mathrm{dip}}(\boldsymbol{r}) = -\nabla U_{\mathrm{dip}}(\boldsymbol{r}) = -\frac{\mathrm{Re}\,(\alpha)}{2\epsilon_0 c}\nabla I(\boldsymbol{r}). \tag{3.3}$$

The imaginary part of the complex polarisability (the in-quadrature component) is responsible for absorption of radiation, which is then re-emitted as dipole radiation. For photons with an energy $\hbar\omega$ the scattering rate is

$$\Gamma_{\mathrm{sc}} = \frac{P_{\mathrm{abs}}}{\hbar\omega} = \frac{\mathrm{Im}\,(\alpha)}{\hbar\epsilon_0 c} I(\boldsymbol{r}), \tag{3.4}$$

because the power absorbed by the oscillator is given by [76]

$$P_{\mathrm{abs}} = \left\langle \dot{\boldsymbol{d}} \cdot \boldsymbol{E} \right\rangle = 2\omega\,\mathrm{Im}\,(|d||E_0^*|) = \frac{\omega\,\mathrm{Im}\,(\alpha)}{\epsilon_0 c} I. \tag{3.5}$$

Using the damped classical Lorentz oscillator model of an electron bound elastically to the core, the frequency-dependent polarisability $\alpha(\omega)$ of an atom can be found. In the dipole approximation the equation of motion of the electron is

$$m_{\mathrm{e}}\,\ddot{\boldsymbol{x}} + m_{\mathrm{e}}\,\Gamma\,\dot{\boldsymbol{x}} + m_{\mathrm{e}}\,\omega_0^2\,\boldsymbol{x} = -e\boldsymbol{E}(t), \tag{3.6}$$

in which m_{e} is the (reduced) mass of the electron, e is the elementary charge, and Γ is the damping rate due to the charge acceleration. From quantum-mechanical calculations it is found that it corresponds to the Einstein A_{21} rate coefficient for spontaneous emission. The solution to this equation is

$$\boldsymbol{x}(t) = \frac{eE(\boldsymbol{r},t)}{m_{\mathrm{e}}} \frac{1}{\omega^2 - \omega_0^2 - i\omega\Gamma}. \tag{3.7}$$

Combining the fact that the dipole moment of the Lorentz atom is given by

$$\boldsymbol{d} = -e\boldsymbol{x}, \tag{3.8}$$

with Eq. (3.1) we find that

$$\alpha(\omega) = \frac{e^2}{m_{\mathrm{e}}} \frac{1}{\omega_0^2 - \omega^2 - i\omega\Gamma}. \tag{3.9}$$

This classical result needs to be patched in order to be in agreement with the quantum-mechanical calculation. Therefore we introduce

$$\Gamma = \frac{e^2}{m_{\mathrm{e}}} \frac{\omega^2}{6\pi\epsilon_0 c^3} \tag{3.10}$$

for the damping coefficient and the on-resonance damping rate

$$\gamma = \Gamma \left(\frac{\omega_0}{\omega}\right)^2 = \frac{e^2\omega_0^2}{m_{\mathrm{e}} 6\pi\epsilon_0 c^3}. \tag{3.11}$$

Careful analysis shows that γ is the natural linewidth of the atomic transition. Substituting these equations into Eq. (3.9) results in

$$\alpha(\omega) = 6\pi\epsilon_0 c^3 \frac{\gamma/\omega_0^2}{\omega_0^2 - \omega^2 + i(\omega^3/\omega_0^2)\gamma}. \tag{3.12}$$

Eq. (3.12) is only valid for low saturation. However, since dipole traps are generally tuned sufficiently far from the atomic resonance in order to suppress photon scattering, this requirement can easily be fulfilled. By combining Eq. (3.12) with Eqs. (3.2) and (3.4) for the dipole potential and the scattering rate the following expressions can be derived for sufficiently large detunings ($\omega - \omega_0 \gg \gamma$):

$$U_{\mathrm{dip}}(\boldsymbol{r}) = \frac{3\pi c^2 \gamma}{\omega_0^2} \frac{1}{\omega^2 - \omega_0^2} I(\boldsymbol{r}), \tag{3.13a}$$

$$\Gamma_{\mathrm{sc}}(\boldsymbol{r}) = \frac{6\pi c^2 \gamma^2}{\hbar\omega_0} \left(\frac{\omega}{\omega_0}\right)^3 \left(\frac{1}{\omega^2 - \omega_0^2}\right)^2 I(\boldsymbol{r}). \tag{3.13b}$$

This can be rewritten as

$$U_{\mathrm{dip}}(\boldsymbol{r}) = \frac{3\pi c^2 \gamma}{2\omega_0^3} \left(\frac{1}{\omega - \omega_0} - \frac{1}{\omega + \omega_0}\right) I(\boldsymbol{r}), \tag{3.14a}$$

$$\Gamma_{\mathrm{sc}}(\boldsymbol{r}) = \frac{3\pi c^2 \gamma^2}{2\hbar\omega_0^3} \left(\frac{\omega}{\omega_0}\right)^3 \left(\frac{1}{\omega - \omega_0} - \frac{1}{\omega + \omega_0}\right)^2 I(\boldsymbol{r}). \tag{3.14b}$$

These expressions can be simplified again by applying the rotating wave approximation (RWA) in which terms that oscillate at twice the frequency of the electric field are neglected, since the atom will not be able to follow them. In most experiments the laser is far detuned from the atomic transition; however, this detuning usually is still small compared to the frequency itself ($\delta = \omega - \omega_0 < \omega_0$, $\omega/\omega_0 \approx 1$), so the RWA can be applied [79], resulting in

$$U_{\mathrm{dip}}(\boldsymbol{r}) = \frac{3\pi c^2 \gamma}{2\omega_0^3} \frac{1}{\delta} I(\boldsymbol{r}), \tag{3.15a}$$

$$\Gamma_{\mathrm{sc}}(\boldsymbol{r}) = \frac{3\pi c^2 \gamma^2}{2\hbar\omega_0^3} \frac{1}{\delta^2} I(\boldsymbol{r}). \tag{3.15b}$$

Using these equations the following simple relation between the dipole potential and the scattering rate is found:

$$\Gamma_{\mathrm{sc}}(\boldsymbol{r}) = \frac{\gamma}{\delta} \frac{U_{\mathrm{dip}}(\boldsymbol{r})}{\hbar}. \tag{3.16}$$

From Eqs. (3.15) one can now easily see that when red-detuned light ($\delta < 0$) is used atoms will be attracted to places with high field intensities. Furthermore,

since the scattering rate falls off with δ^2, whereas the trapping potential decreases with δ, one immediately sees why ODTs are generally made at large detunings. It is also possible to make ODTs with blue detuned light. This is usually done using hollow laser beams with a doughnut-shaped Laguerre-Gaussian mode (cf. e. g. [75, 80–82]). The most important advantage of a blue detuned dipole trap is the fact that atoms are stored in a dark area so that there is no trap loss due to light-induced processes.

Optical dipole traps that operate within the validity of the RWA, but with low scattering rates are called far-off-resonance traps or FORTs [10]. ODTs that operate at such large detunings that the light field can be considered as a quasi-static field are called quasi-electrostatic traps or QUESTs [11, 12, 65, 83, 84]. In this work only FORTs will be considered.

This classical description of dipole-force interaction can of course be supplemented by a quantum-mechanical treatment as described by Dalibard and Cohen-Tannoudji [78, 85] where the dipole potential is described as the shift of the atomic ground state resulting from the "dressing" of the atoms with the quantised light field, the so-called ac Stark shift. However, as long as the number of photons in the field is large the classical description of the field is still valid.

3.2.2 *Multilevel atoms*

The derivation of Eqs. (3.15) is based on a two-level system. This model usually works well because one usually works relatively close to one transition which therefore dominates the interactions. However, if the system under investigation has a more elaborate level structure as is the case for an alkali atom, all relevant transitions must be taken into account. In our case this means that at least the fine-structure splitting must be taken into account. The existence of multiple levels in the model of the previous section leads to state-dependent polarisabilities. By treating the effect of the laser light as a second-order perturbation, the shift of the ground state energy of level i is given by [75, 78]

$$\Delta E_i(\boldsymbol{r}) = \frac{3\pi c^2 \gamma}{2\omega_0^3} I(\boldsymbol{r}) \sum_j \frac{C_{ij}^2}{\delta_{ij}}, \tag{3.17}$$

where C_{ij} are the Clebsch-Gordan coefficients of the transition between ground state level $|g_i\rangle$ and excited state level $|e_j\rangle$ with a detuning δ_{ij}.

In our experiments the trapping laser detunings generally are in the order of a few nanometers, i. e. the ground state and excited state hyperfine structure splittings are not resolved, but the fine structure is: $\Delta\omega_{\mathrm{FS}'} \gtrsim |\delta| \gg \Delta\omega_{\mathrm{HFS}}, \Delta\omega_{\mathrm{HFS}'}$ (where the primes refer to the excited state). If the hyperfine splitting is resolved for the ground state but not for the excited state, we find, incorporating the

polarisation of the light into Eq. (3.17), the following expressions for the dipole potential and the scattering rate of a ground state $|F, m_F\rangle$ [75, 86]:

$$U_{\mathrm{dip}}(\boldsymbol{r}) = \frac{\pi c^2 \gamma}{2\omega_0^3}\left(\frac{2+\mathcal{P}\,g_F\,m_F}{\delta_2} + \frac{1-\mathcal{P}\,g_F\,m_F}{\delta_1}\right) I(\boldsymbol{r}) \text{ and} \tag{3.18a}$$

$$\Gamma_{\mathrm{sc}}(\boldsymbol{r}) = \frac{\pi c^2 \gamma^2}{2\hbar\omega_0^3}\left(\frac{2+\mathcal{P}\,g_F\,m_F}{\delta_2^2} + \frac{1-\mathcal{P}\,g_F\,m_F}{\delta_1^2}\right) I(\boldsymbol{r}). \tag{3.18b}$$

Here δ_1 and δ_2 refer to the detuning from the D_1 and the D_2 line, respectively. The hyperfine state is designated by m_F and the polarisation of the light by $\mathcal{P}$, with $\mathcal{P} = 0, \pm 1$ for linearly or $\sigma^{\pm}$ polarised light, respectively. The constant g_F is the ground state Landé factor [72, 73, 87]

$$g_F \approx g_J \frac{F(F+1) - I(I+1) + J(J+1)}{2F(F+1)}, \tag{3.19}$$

with

$$g_J \approx 1 + \frac{J(J+1) + S(S+1) - L(L+1)}{2J(J+1)}, \tag{3.20}$$

where F refers to the hyperfine level quantum number, I is the nuclear spin (cf. tables B.1 and B.2) and S, L and J are the well-known electron spin, electron orbital, and total angular momentum quantum numbers, respectively. Since the rubidium ground state is a $^2S_{1/2}$ state, $g_J = 2$.

3.2.3 *Multi-frequency laser light*

So far only light from a CW laser, i. e. monochromatic or narrow band light has been considered. Extending the model to pulsed light is simple for the case that the detuning of the laser is larger than the bandwidth of the laser pulse. As specified in § 4.5, the laser we use to make our FORT has a pulse duration of $\tau_p = 1.2\,\mathrm{ps}$ which corresponds to a FWHM bandwidth of $\Delta\lambda = 0.65\,\mathrm{nm}$ near 810 nm where we usually operate our laser. Therefore this assumption is valid for our experiments. For sufficiently large detunings, the interaction of the ML laser light with the atom can be assumed as separate interactions of the atom with each of the laser modes in the frequency comb. Consequently, the trap depth and the scattering rate are the average of these quantities for each individual mode as long as the excitation remains low and no saturation takes place [88].

3.2.4 *Typical FORT characteristics*

Now that the theoretical framework has been established some typical properties of a FORT under our experimental conditions can be specified. In the experiments

PROPERTY	SYMBOL	VALUE
Wavelength	λ	810 nm
Average laser power	P	0.3 W
Beam waist	w_0	20 µm
Rayleigh range	z_R	1.6 mm
Trap depth	U_0	−0.59 mK
Scattering rate	Γ_{sc}	50 Hz
Radial trap frequency	$\omega_\rho/2\pi$	3.8 kHz
Axial trap frequency	$\omega_z/2\pi$	35 Hz

Table 3.1: Typical FORT characteristics for our experimental conditions.

discussed in this thesis a Gaussian laser beam is used. The intensity for such a beam is given by

$$I(\boldsymbol{r}) = I(\rho, z) = \frac{2P}{\pi\, w(z)^2}\, \mathrm{e}^{-2\rho^2/w(z)^2}, \tag{3.21}$$

with P the laser power, $w(z) = w_0\sqrt{1+(z/z_R)^2}$ the beam waist at a certain position, w_0 the e^{-2} beam radius and $z_R = \pi\, w_0^2/\lambda$ the Rayleigh range. We define the trap depth U_0 of a FORT as the potential depth at the centre:

$$U_0 \equiv |U_{\mathrm{dip}}(0,0)|. \tag{3.22}$$

Usually the trap depth is expressed in units of temperature: U_0/k_B. If $U_{\mathrm{dip}}(\rho, z)$ is approximated by a harmonic potential, the trap frequencies in both the axial and the radial direction can be derived:

$$\omega_\rho = \sqrt{\frac{4U_0}{m\, w_0^2}}, \tag{3.23a}$$

$$\omega_z = \sqrt{\frac{2U_0}{m\, z_R^2}}. \tag{3.23b}$$

Table 3.1 shows typical numbers and Fig. 3.1 shows a figure of the FORT potential according to Eq. (3.18a) for a red detuned Gaussian beam. In Fig. 3.2 the FORT depth $U_{\mathrm{dip}}(0,0)$ is plotted as a function of the wavelength of the trapping laser. Note the D_1 and the D_2 lines at 795 nm and 780 nm, respectively. Also note that in part of the region between the D-lines trapping is still possible.

In order to find the regions of trapping, a simulation was made. In this simulation the MOT is modelled as a collection of atoms with a Maxwell-Boltzmann

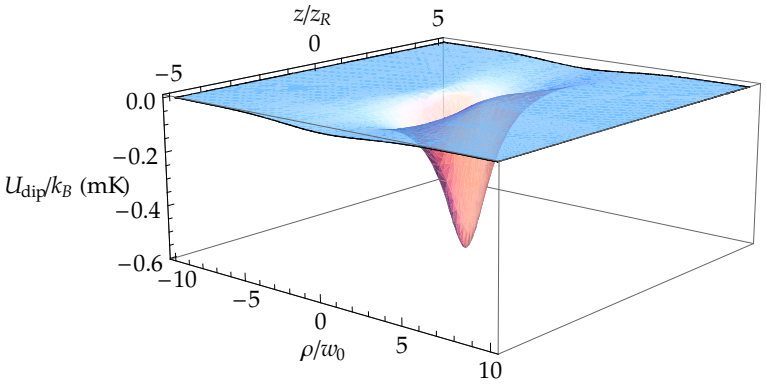

Figure 3.1: The FORT potential of a red detuned Gaussian beam for the properties listed in table 3.1. Note that the aspect ratio of the ρ and z axis is not 1 : 1. Figure C.1 on page 110 is a colour print of this figure.

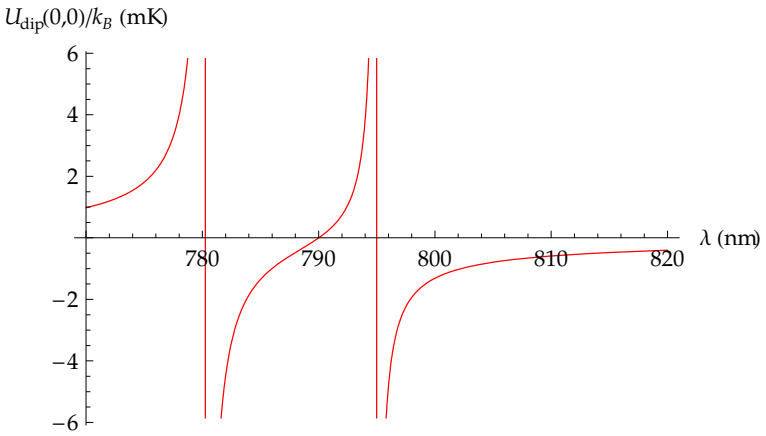

Figure 3.2: The FORT potential depth at the centre of the trap $U_{\mathrm{dip}}(0,0)$ as a function of the laser wavelength for linear polarisation. The experimental parameters are $P = 0.3\,\mathrm{W}$, $w_0 = 20\,\mu\mathrm{m}$.

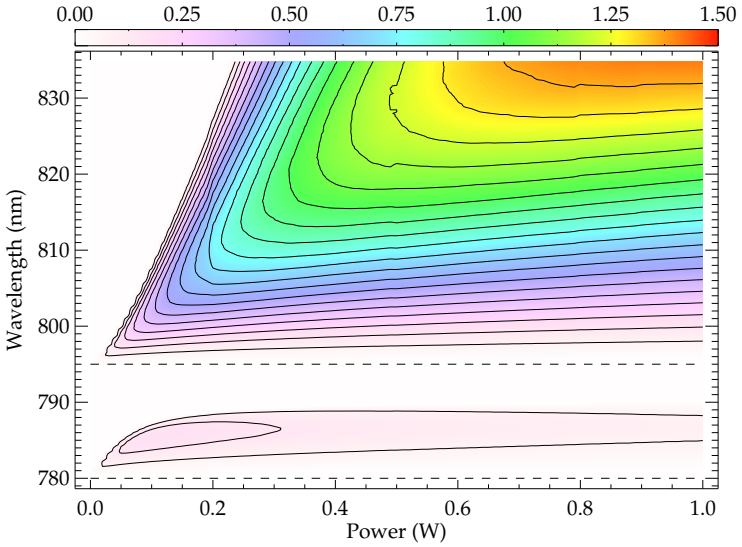

Figure 3.3: Simulation of the lifetime of a FORT as a function of the wavelength and the power of the FORT laser. The colour bar indicates the 1/e lifetime in seconds. The positions of the D-lines are indicated by the dashed lines. Figure C.2 on page 110 is a colour print of this figure.

distributed velocity according to the MOT temperature in a random direction. The atoms are positioned according to a Gaussian distribution. Subsequently the atoms are placed in the FORT potential. The 1/e lifetime is determined by monitoring the scattering of atoms out of the trap, both due to the FORT laser light and the background gas atoms. The results are shown in Fig. 3.3. Clearly trapping close to the D-lines is not possible, but depending on the power of the FORT laser, short lifetimes may be achieved in the inter-D-line region. As is to be expected the lifetime increases as the wavelength recedes from the D_1 line and the power increases.

3.3 LASER COOLING

From the previous discussion it is clear that light can exert a force on atoms. However, in order to be able to trap atoms from a room temperature vapour the (nearly) conservative potential of a FORT is not enough since the attainable trap depths are limited to the mK range. The number of atoms in the low velocity tail of the Maxwell-Boltzmann distribution of a room-temperature gas is very low. It is therefore necessary to cool the atoms in order for them to be captured in an ODT. Using the radiation-pressure force it turns out to be possible to trap atoms

and cool them down to μK level.

3.3.1 *Optical molasses*

Consider the following simple model for the radiation-pressure force. A two-level atom is located in a monochromatic laser beam which has a small detuning δ to the red of the atomic resonance at ω_0, and a wavevector $\boldsymbol{k}$. If the intensity is sufficiently low the atom will absorb light from the laser beam and will decay to the ground state at some later time due to spontaneous emission. Each time a photon is absorbed, the momentum of the atom decreases by an amount equal to the photon momentum. The recoil velocity associated with such a photon recoil is

$$v_\mathrm{r} = \frac{\hbar k}{m}, \tag{3.24}$$

which is of the order of several mm/s for Rb (cf. table B.3). After each spontaneous emission event the momentum of the atom is changed by the momentum of the emitted photon. However, since these emissions happen in a random direction and average out, the net momentum change is directed along $\boldsymbol{k}$. Therefore the force of the light exerted on the atom is given by the change of momentum due to one photon absorption multiplied by the average rate of absorption [74]:

$$\boldsymbol{F}_\mathrm{rad} = \hbar \boldsymbol{k}\, \gamma \rho_{ee}, \tag{3.25}$$

where ρ_{ee} is the fraction of atoms in the excited state given by

$$\rho_{ee} = \frac{1}{2}\frac{s}{s+1}, \tag{3.26}$$

with s the off-resonance saturation parameter at detuning δ:

$$s = \frac{s_0}{1 + (2\delta/\gamma)^2}. \tag{3.27}$$

Here s_0 is the on-resonance saturation parameter defined as

$$s_0 \equiv \frac{2|\Omega|^2}{\gamma^2} = \frac{I}{I_\mathrm{sat}}, \tag{3.28}$$

with Ω and I the Rabi frequency and the intensity of the laser light, respectively. The on-resonance saturation intensity I_sat is defined by

$$I_\mathrm{sat} \equiv \frac{\pi h c \gamma}{3\lambda^3}, \tag{3.29}$$

with h Planck's constant and λ the wavelength of the transition. Values for I_sat for rubidium transitions used in our experiments are given in Appendix B.1.

More information on calculating I_{sat} can be found in Refs. [72, 73]. The radiation-pressure force can now be written in its well-known form

$$\boldsymbol{F}_{\text{rad}} = \frac{\hbar \boldsymbol{k} \gamma}{2} \frac{s_0}{1 + s_0 + (2\delta/\gamma)^2}. \tag{3.30}$$

From this expression one easily sees that the spontaneous force saturates at $\hbar k\gamma/2$ for large intensities.

In order to show how the radiation-pressure force gives rise to cooling consider a 1D model of an atom moving with velocity $\boldsymbol{v}$ in the field of two counterpropagating laser fields with wavevectors $\pm\boldsymbol{k}$. The force $\boldsymbol{F}_{\pm}$ of each beam is given by Eq. (3.30) but with the detuning modified to account for the Doppler shift:

$$\boldsymbol{F}_{\pm} = \pm \frac{\hbar \boldsymbol{k} \gamma}{2} \frac{s_0}{1 + s_0 + [(2\delta \mp \boldsymbol{k} \cdot \boldsymbol{v})/\gamma]^2}. \tag{3.31}$$

Again, this is for low intensities ($\Omega \ll \delta, \gamma$) and ignores interference. For a stationary atom the net force $\boldsymbol{F}_{\text{mol}} = \boldsymbol{F}_{+} + \boldsymbol{F}_{-}$ is zero. For an atom with a small velocity $kv \ll \delta$, γ a series expansion of the force in v can be made, resulting in

$$\boldsymbol{F}_{\text{mol}} \approx \frac{8\hbar k^2 \, \delta \, s_0}{\gamma[1 + s_0 + (2\delta/\gamma)^2]^2} \boldsymbol{v} \equiv -\beta \boldsymbol{v}. \tag{3.32}$$

Thus for small velocities and negative detunings the force leads to deceleration of the atom, giving this configuration the name optical molasses [62, 89], with β the viscosity. Figure 3.4 shows the 1D optical molasses force of Eq. (3.31) for negatively detuned lasers as a function of the velocity of the atom. Also shown are the components due to the individual laser beams and the approximation for small velocities of Eq. (3.32). Because the absorption of light does not stop when the atomic speed approaches zero, and because every absorption is followed by spontaneous emission with a recoil energy $E_{\text{r}} = \hbar^2 k^2 / 2m$, the atom will never come to a true stand still but will undergo a random walk in momentum space with step size $\hbar k$. This leads to heating as will be discussed in the following section.

3.3.2 *Temperature*

Using Boltzmann's law the mean kinetic energy can be related to temperature according to the relation

$$\frac{1}{2} m \langle v^2 \rangle = \frac{1}{2} k_{\text{B}} T \tag{3.33}$$

for a system with one degree of freedom. This implies that the velocities are distributed according to a Maxwell-Boltzmann distribution. Even if this is not

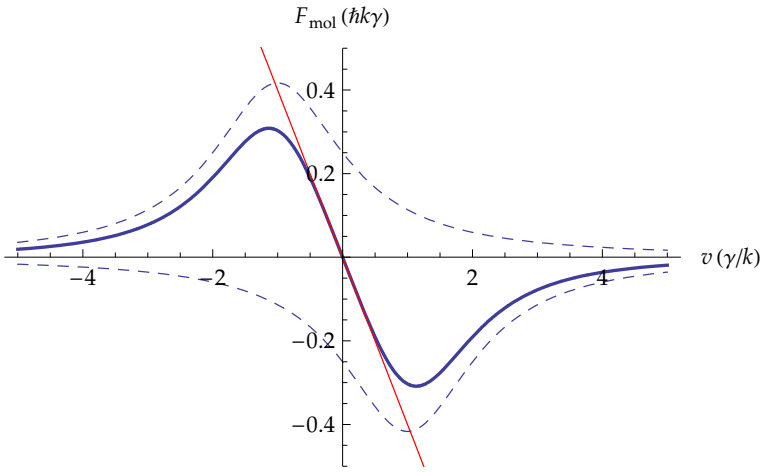

Figure 3.4: The optical molasses force in 1D. The dashed curves represent the forces of the individual laser beams, the straight line shows the approximation of Eq. (3.32).

the case, the temperature derived from this expression is nevertheless a good parametrisation of the mean kinetic energy. To arrive at an expression for the temperature of a laser-cooled gas, we first calculate the cooling rate in the 1D model:

$$\left(\frac{\mathrm{d}E}{\mathrm{d}t}\right)_{\mathrm{cool}} = \langle \boldsymbol{v} \cdot \boldsymbol{F}_{\mathrm{mol}} \rangle = \beta \langle v^2 \rangle. \tag{3.34}$$

The heating due to the spontaneous emission can be calculated by using the fact that the energy change in one absorption-emission cycle is given by [89, 90]

$$\Delta E = \frac{\hbar^2 k^2}{m}, \tag{3.35}$$

where the fact that the distribution of the emitted photons is point-symmetric has been taken into account. Since this energy change occurs at the rate of the photon scattering, the heating rate is given by

$$\left(\frac{\mathrm{d}E}{\mathrm{d}t}\right)_{\mathrm{heat}} = 2\Gamma_{\mathrm{sc}} \frac{\hbar^2 k^2}{m}, \tag{3.36}$$

with $\Gamma_{\mathrm{sc}} = F_{\mathrm{rad}}/\hbar k$ the scattering rate of one laser beam. Here we assumed that the total scattering rate of the two laser beams is twice that of a single laser beam, which holds for low intensities. The minimum attainable temperature can be

found by looking at the steady state, where the cooling and heating rates are equal. Combining Eqs. (3.33), (3.34) and (3.36) gives

$$\begin{aligned} 2\Gamma_{\mathrm{sc}} \frac{\hbar^2 k^2}{m} &= \beta \langle v^2 \rangle \\ &= \beta \frac{k_{\mathrm{B}} T}{m}. \end{aligned} \tag{3.37}$$

For low intensities this leads to

$$k_{\mathrm{B}} T = -\frac{\hbar \gamma}{4} \frac{\gamma}{2\delta} \left[1 + \left(\frac{2\delta}{\gamma} \right)^2 \right]. \tag{3.38}$$

This function has a minimum for $\delta = -\gamma/2$, which leads to

$$k_{\mathrm{B}} T_{\mathrm{D}} = \frac{\hbar \gamma}{2}, \tag{3.39}$$

which is the definition of the Doppler temperature, the minimum temperature that can be reached in the framework of the above model of Doppler cooling. However, in practice temperatures well below the Doppler temperature are easily obtained. This can be explained by effects like polarisation gradient cooling and Sisyphus cooling (cf. e. g. [74, 85]). The Doppler temperature for rubidium is 143 µK (cf. Table B.3).

3.4 THE MAGNETO-OPTICAL TRAP

Compared to other traps, e. g. magnetic traps, the potential depths of ODTs are relatively small, in the order of a few milliKelvins. Consequently, to load atoms in a dipole trap one has to start with a sample of cold atoms. In our case atoms are loaded from a magneto-optical trap (MOT) [5]. The MOT is the most commonly used trap for neutral atoms. It is based on the cooling principles outlined in the previous section. Although atoms can be cooled using optical molasses there is no position dependency in the molasses force and therefore no confinement. By introducing a magnetic field gradient this problem can be overcome.

The simplest one-dimensional model for a MOT consists of an atom with a $|J = 0\rangle$ ground state and a $|J' = 1\rangle$ excited state with three magnetic sub-levels with quantum numbers $m_{J'} = 0, \pm 1$. The light field consists of the same two counterpropagating laser beams propagating along the $\hat{z}$-axis as in the case of optical molasses. By applying a linearly increasing magnetic field $\boldsymbol{B} = Bz$ along the $\hat{z}$-axis the $m_{J'} = \pm 1$ levels are shifted due to the Zeeman effect. Choosing a $\sigma^+\sigma^-$ configuration as depicted in Fig. 3.5 will result in a shifting of the levels in such a way that an atom in the area of positive z will absorb more light from the σ^--beam and less light from the beam coming from the opposite direction, resulting in a net force towards the centre.

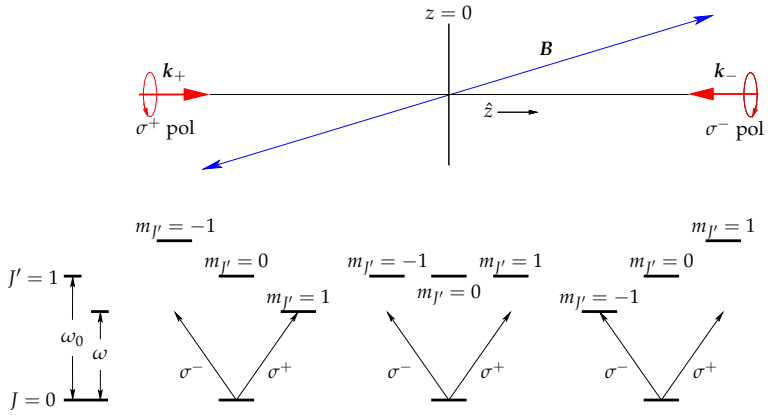

Figure 3.5: Schematic 1D MOT configuration with the corresponding level shifts at different positions along the $\hat{z}$-axis.

Similar to the optical molasses case, the force of the two counterpropagating laser beams on a moving atom is the sum of the forces of the two individual laser beams: $\boldsymbol{F}_{\mathrm{MOT}} = \boldsymbol{F}_+ + \boldsymbol{F}_-$. The individual forces are now slightly modified compared to Eq. (3.30) by the introduction of the magnetic field:

$$\boldsymbol{F}_{\mathrm{MOT}} = \frac{\hbar \boldsymbol{k} \gamma}{2} \frac{s_0}{1 + s_0 + (2\delta_\pm/\gamma)^2}, \tag{3.40}$$

with

$$\delta_\pm = \delta \mp \boldsymbol{k} \cdot \boldsymbol{v} \pm \mu_{\mathrm{eff}} B/\hbar. \tag{3.41}$$

The last term is the Zeeman shift of the levels for a magnetic field B, with μ_{eff} the effective magnetic moment for the transition defined by $\mu_{\mathrm{eff}} = \mu_{\mathrm{B}}(g_e m_e - g_g m_g)$. Here g_i is the Landé factor of Eq. (3.19) and m_i the magnetic quantum number for the excited state and the ground state, respectively. Using the same assumptions as in the molasses case, the force can be approximated by

$$\boldsymbol{F} = -\beta \boldsymbol{v} - \kappa \boldsymbol{r}, \tag{3.42}$$

with

$$\kappa = \frac{\mu_{\mathrm{eff}}}{\hbar k} \beta \frac{\mathrm{d}B}{\mathrm{d}z}. \tag{3.43}$$

So we now effectively have a force that can both cool and trap atoms.

This 1D model can be extended to three dimensions by taking six laser beams in three orthogonal directions and using two coils in anti-Helmholtz configuration to generate the desired magnetic field gradient. This setup is shown in Fig. 3.6.

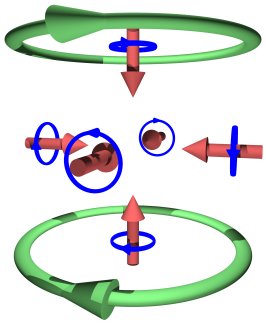

Figure 3.6: Schematic 3D representation of the MOT fields. The large circles represent the currents through the coils, the arrows represent the laser beams together with their polarisations.

So far the discussion is based on a two-level atom. Because cooling and trapping depend on the presence of a closed transition for the cycles of absorption and spontaneous emission, the presence of other levels will decrease the effectiveness of the mechanism. The hyperfine structure of the alkali atoms effectively adds a second ground state to the model (cf. Fig. B.2). Because the linewidth of the MOT lasers is much less than the level splitting (less than 1 MHz vs. a few GHz) the atoms will be optically pumped to the dark state, i. e. the hyperfine ground state that does not communicate with the laser, and are lost from the process. This pumping can be counterbalanced by using a second laser tuned to the unwanted transition, the so-called repump laser. This laser pumps the atoms from the dark state to one of the excited state hyperfine levels from where they can decay to the ground state and take part in the cooling transition. For ^{85}Rb the cooling or trapping transition is $F = 3 \rightarrow F' = 4$ and the repump transition is $F = 2 \rightarrow F' = 3$. For ^{87}Rb these transitions are $F = 2 \rightarrow F' = 3$ and $F = 1 \rightarrow F' = 2$.

General properties like the number of atoms trapped in the MOT and their temperature will be discussed in § 4.10.

4

THE EXPERIMENTAL SETUP

In this chapter the details will be discussed of the experimental setup used for the work described in this thesis. First the vacuum system and the MOT magnetic field are described, followed by the laser systems (Sections 4.3 - 4.5). Subsequently the imaging optics and the beam shutters are specified. In Sections 4.8 and 4.9 the computer control hardware and software needed for the timing of the experiments are presented. Finally the basic MOT characteristics are discussed.

4.1 VACUUM SYSTEM

A stainless steel vacuum chamber is used in the experiments. Figure 4.1 shows a schematic overview of the chamber. All windows in the setup have an antireflection coating for 780 nm light. A 230 l/s turbo pump and a foreline pump[a] maintain a background pressure below $5 \cdot 10^{-9}$ mbar[b]. When rubidium vapour is admitted from the reservoir R, the pressure rises to approximately $1 \cdot 10^{-8}$ mbar. The reservoir is separated from the main chamber by a manually operated valve. It contains an ampule with 1 g of Rb in its natural abundance (cf. § 2.3). It is heated to 65 °C to increase the rubidium flow into the central chamber. To increase the rubidium pressure in the central chamber the cross-piece between the chamber and the reservoir can be heated further, thus aiding the alignment of the MOT and FORT beams thanks to increased fluorescence. However, the crosspiece is not heated during experiments to maximise FORT storage times.

a Balzers TPU 240 and Edwards Two Stage E2M 12, respectively.
b Measured with a Balzers Compact Full Range Gauge, type PKR251. The lowest measurable pressure for this gauge is $4.5 \cdot 10^{-9}$ mbar.

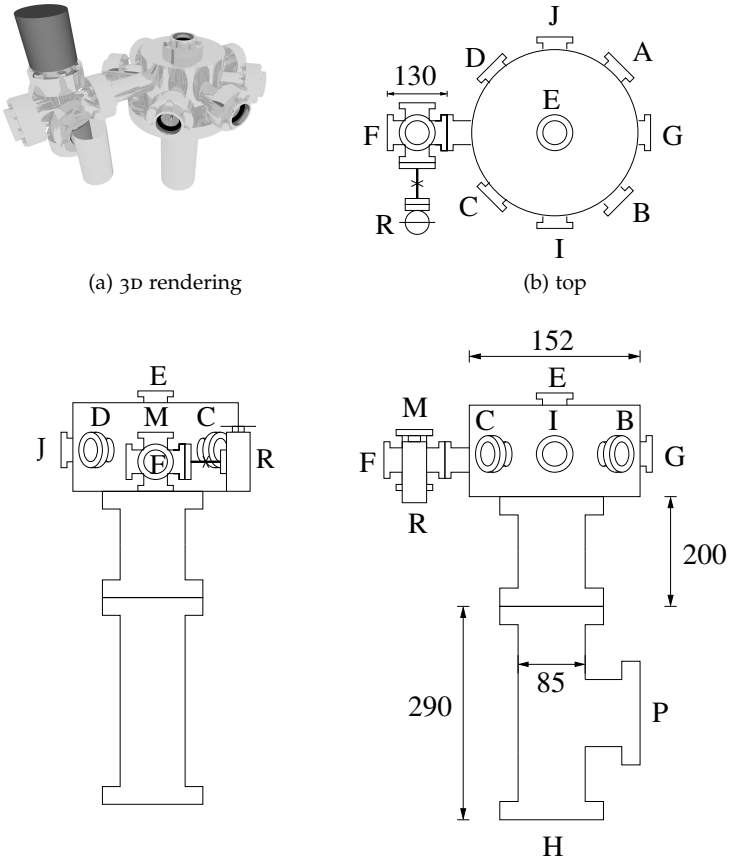

(a) 3D rendering (b) top

(c) left (d) front

Figure 4.1: A schematical representation of the vacuum chamber. A-J are windows with AC the MOT x-axis, BD the y-axis and EH the z-axis. The FORT beam passes through windows IJ. Windows F and G are used for detection with the CCTV and CCD camera, respectively (cf. § 4.6). Port M is connected to the PKR251 pressure gauge and port P is connected to the turbo pump. R is the Rb reservoir. All dimensions are in mm.

4.2 MAGNETIC FIELD

The quadrupole magnetic field of the MOT is produced by two coils with a diameter of 230 mm mounted in the anti-Helmholtz configuration. The height of the coils is 60 mm. Both coils consist of 207 windings. The distance between the top of the lower coil and the bottom of the upper one is 76 mm. The maximum allowed stationary current through the coils is 13.5 A in which case the coils reach an operating temperature of 153 °C [91]. The coils have a resistance of 0.9 Ω, an inductance of 1.9 mH and are water-cooled on the outside, allowing for experiments beyond the maximum current. During MOT alignment, for example, the current is temporarily increased to approximately 20 A. Each of the coils is powered by a separate current supply[c] that can provide a maximum current of 20 A at 35 V. In order to be able to switch off the MOT coils within a few milliseconds a switch based on an insulated gate bipolar transistor (IGBT) was implemented. Figure 4.2 shows a simplified diagram of the wiring of the power supply, the coil and the IGBT.

Figure 4.3 shows a measurement of the magnetic field in the vertical direction. Here, the current I in each coil is 6.0 A. The solid line is a fit to the calculated magnetic field based on a simple model for the field on the axis of two solenoids of radius r and height d:

$$B(z) = \frac{1}{2}\mu_0 n I \left\{ \left(\frac{h + \frac{d}{2} - z}{\sqrt{(h + \frac{d}{2} - z)^2 + r^2}} - \frac{h - \frac{d}{2} - z}{\sqrt{(h - \frac{d}{2} - z)^2 + r^2}} \right) + \left(\frac{h - \frac{d}{2} + z}{\sqrt{(h - \frac{d}{2} + z)^2 + r^2}} - \frac{h + \frac{d}{2} + z}{\sqrt{(h + \frac{d}{2} + z)^2 + r^2}} \right) \right\}, \quad (4.1)$$

where n is the number of windings divided by the height of the coils. The centres of the solenoids are at $z = \pm h$. The fit parameters are the amplitude of the signal

c Delta Elektronica SM 7020-D

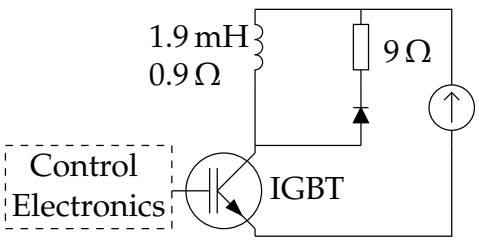

Figure 4.2: A simplified wiring diagram of one of the the MOT magnetic field switches with an IGBT.

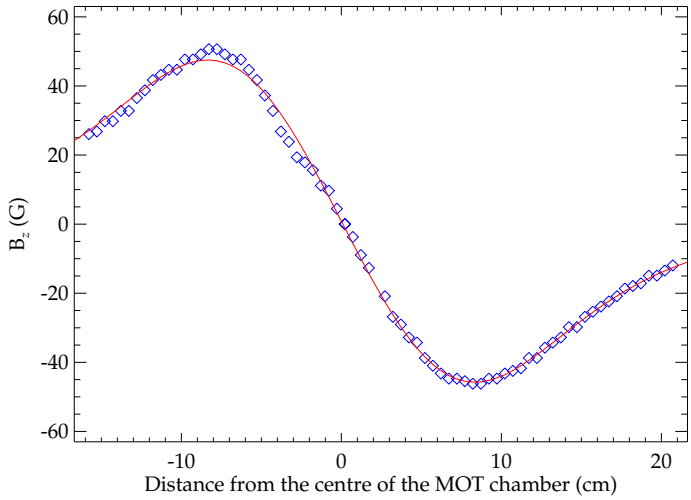

Figure 4.3: Measurement of the MOT magnetic field in the z-direction for a current of 6.0 A. The solid line is a fit to the calculated field (Eq. (4.1)).

(to correct for errors in the current and the calibration of the Hall probe) and a horizontal and vertical offset. The gradient as function of the current through the coils is found to be $I \times 1.50 \pm 0.01\,\mathrm{G{\cdot}A^{-1}{\cdot}cm^{-1}}$. The typical current during the experiments is 8.1 A for the upper coil and 8.0 A for the lower coil, resulting in a gradient of 12.0 G/cm in the vertical direction. In the horizontal directions the gradient is half of that because $\boldsymbol{\nabla} \cdot \boldsymbol{B} = 0$. The difference in current between the upper and lower coil increases for higher currents in order to keep the MOT positioned in the centre of the overlapping laser beams (cf. § 4.3). This is probably caused by the fact that the upper coil lies on top of the vacuum chamber and therefore encloses less steel. This difference in current is unfortunate and also means that it is impossible to connect the two coils in series for equal shutdown characteristics. As a result it is not possible to implement a true molasses cooling phase in the experimental runs since the zero point of the magnetic field moves in the vertical direction during the current shutdown.

4.3 DIODE LASERS

The MOT employs two extended cavity diode lasers[d] in the Littrow setup with an output power of approximately $20 - 30$ mW. One laser is used for the cycling transition and is henceforth referred to as the trapping or cycling laser. The

d Toptica Photonics DL100

other diode laser acts as a repumper (cf. § 3.4). Each DL100 is controlled by a separate temperature controller and current controller[e] in a DC100 supply rack. The diode in the trapping laser was replaced by a diode[f] bought at Thorlabs after the original one died. This diode is not wavelength selected and therefore needs to be cooled approximately 5 °C below the previous Toptica diode. Typical currents and temperatures are 100 mA (−90 mA) and 15 °C (20 °C) for the cycling (repump) laser. Both diode lasers are frequency stabilised using polarisation spectroscopy which will be discussed in § 4.4.

Figure 4.4 shows the optical paths of the two diode laser beams. An anamorphic prism pair[g] is used to compress the long axis of the elliptical beam cross-section in order to make the beam pass through the acousto-optic modulators (AOMs) 'downstream'. The half-wave plate in front of it is necessary to align the polarisation to the Brewster angle of the prisms and avoid losses.

A 39.8 dB optical isolator (OI)[h] is placed in the trapping beam to protect the diode from retro-reflected light. An optical isolator is not inserted in the repump beam, since the repump beam can easily be misaligned a bit without affecting the MOT. However, when directing the beam to the Fabry-Pérot interferometer (FPI) one must be careful not to introduce sidebands or damage the laser diode by reflecting the light back into the diode.

Following the initial beam shaping optics a flip-mounted mirror is inserted to send light to a very simple home-made scanning FPI and check whether the light is single mode or not. The FPI was made of a Thorlabs holder and two coated mirrors from Ekspla. In one of the corners a piezo stack[i] was mounted. The free spectral range is 23 ± 2 GHz and the finesse is 27 ± 1.

The half-wave plate behind the flip-mounted mirror in the path of the repump beam is used to control the light intensity that is split off towards the spectroscopy setup. The AOM in the main path of the repump beam is used as a shutter. To compensate for the inherent frequency shift of 80 MHz another fixed-frequency AOM is inserted before the spectroscopy setup. All AOMs are type 1205C-2 from Isomet, unless mentioned otherwise. They are operated with custom driver boxes based on the Isomet 232-A drivers with an RF output power of approximately 1.2 W. The control boxes are equipped with connectors for a TTL inhibit signal and an analog input for the RF power modulation. Depending on the functionality required for a specific AOM an analog input for the frequency may also be provided, in which case the control box is based on a homemade design based on a Mini Circuits power amplifier and a voltage-controller oscillator (VCO).

Following the AOM, the repump beam is expanded to a 1/e-radius of 9.85 ± 0.04 mm using a Keplerian telescope, and directed to the vacuum chamber. The

e Toptica Photonics DTC100 and Toptica Photonics DCC100, respectively
f Sharp GH0781JA2C
g Toptica APP J
h Optics for Research IO-3D-780-VLP
i Thorlabs AE0203D04F

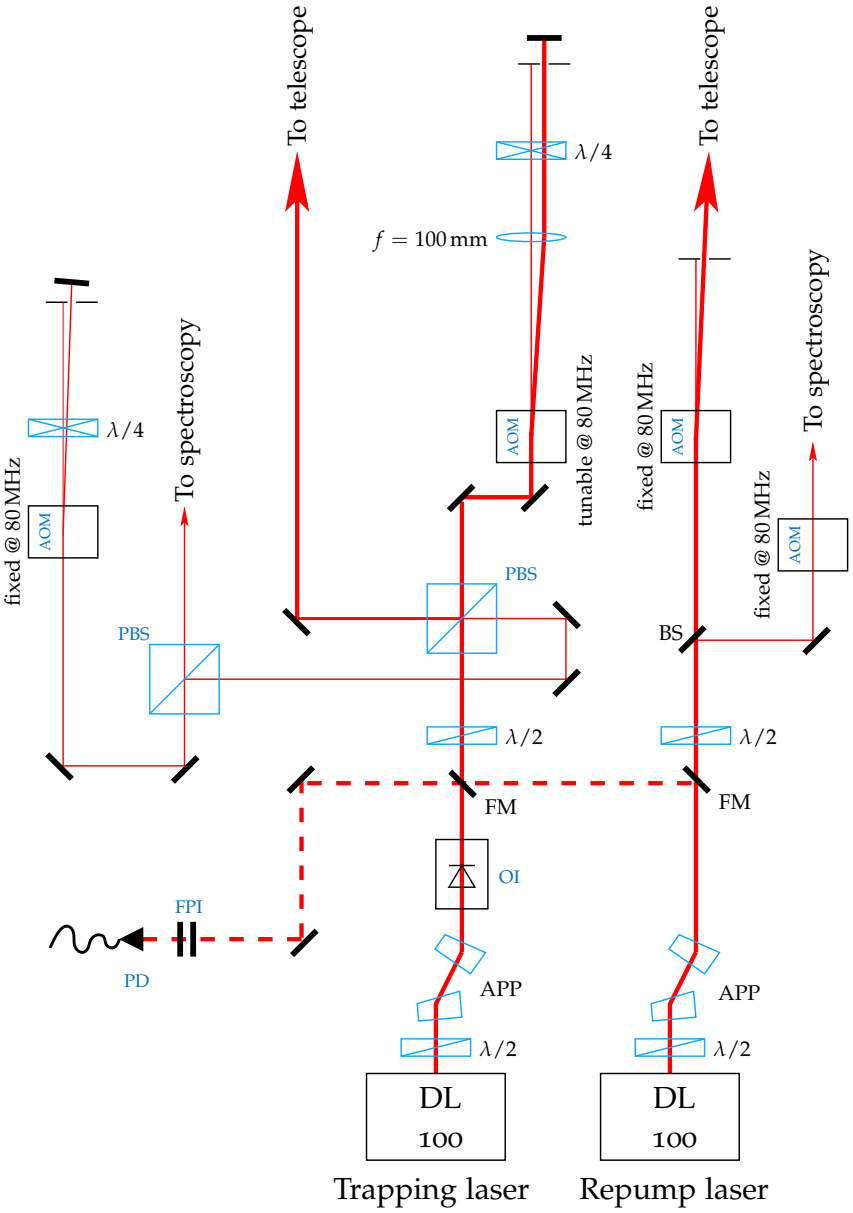

Figure 4.4: Schematic overview of the diode laser beam paths. The spectroscopy setup is shown in detail in Fig. 4.8. The dashed line represents the alternative beam path to the FPI when a flip-mounted mirror is in the upright position. APP: Anamorphic prism pair, BS: beam splitter, FM: Flip-mounted mirror, FPI: Fabry-Pérot interferometer, OI: optical isolator, PBS: polarising beamsplitter cube, PD: photodiode.

power in front of the telescope is 11 mW.

In the trapping beam the half-wave plate reestablishes horizontal polarisation after the optical isolator. The polarising beamsplitter cube (PBS) subsequently splits off a fraction of the light intensity for the spectroscopy, but most of the light is double-passed through an 80 MHz tunable AOM followed by a cat's eye retroreflecting lens setup [92]. The diaphragm ensures that the zeroth order is not reflected back to the AOM. Since the beam passes the quarter-wave plate once before and once after reflection, the polarisation is changed to vertical. The virtue of this setup is that it allows detuning of the laser light without having to adjust the beam path. The fixed frequency 80 MHz AOM[j] in the beam path to the spectroscopy setup cancels the 2×80 MHz shift so that the detuning of the laser beam travelling towards the vacuum chamber is twice the frequency difference from 80 MHz in the main AOM. In this way the laser can be locked on the atomic resonance frequency and the detuning can be set by adjusting the AOM frequency using the control software (cf. § 4.9). The AOM frequency was verified to vary linearly with the voltage applied to the driver. The frequency output of the tunable AOM driver is connected to a frequency counter[k] for easy monitoring during the experiments. Figure 4.5 shows the AOM diffraction efficiency as a function of RF frequency for three different cases. The efficiency for a single-pass setup is indicated by the diamonds and the triangles indicate the efficiency for a double-passed AOM. Inserting the cat's eye lens leads to a significant increase in the bandwidth as shown by the squares. Note that for the double-pass measurements the frequency added to the light is twice the value indicated in the figure. The results of this double-pass setup are comparable to Ref. [92]. We observe an asymmetry of the curves as well, although our efficiencies are generally slightly higher.

After returning from the tunable AOM the (now vertically polarised) trapping beam is deflected at the PBS and sent to a telescope where its 1/e-radius is increased to 0.79 cm, before being sent to the vacuum chamber. The power in front of the telescope is 14 mW.

After being expanded the trapping and repumper beams travel to the experimentation table containing the vacuum chamber. The beam path is shown in Figures 4.6 and 4.7. The trapping beam passes through a PBS which splits off about one third of the incident power for the vertical MOT beams. The rest passes on to the vacuum chamber and makes up the xy beam. After having passed through the vacuum chamber twice, the beam is retroreflected onto itself.

The repump beam travels to the PBS at a lower level and enters it from below. Using the $\lambda/2$ plate the amount of repump light in the z and xy beams can be regulated. Equally dividing the power over the three axes proved to catch the most atoms in the trap.

j Isomet 1205C-1
k HP 5328A Universal Counter

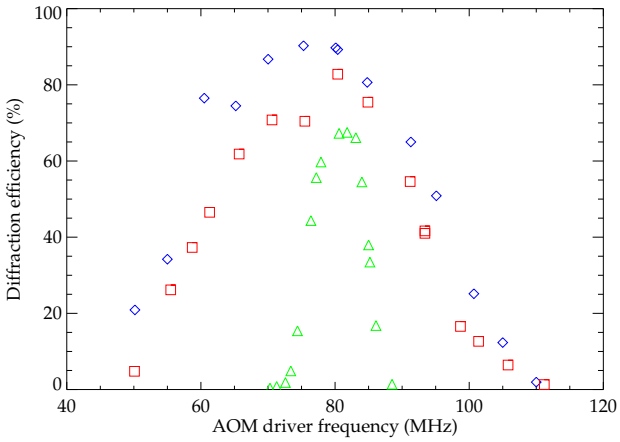

Figure 4.5: Diffraction efficiency of the double-passed AOM with cat's eye lens setup as a function of AOM driving frequency. The diamonds indicate the efficiency for a single-pass AOM, the triangles are for a double-pass setup and the squares indicate the efficiency of the double-pass setup with a cat's eye lens. Note that the effective tuning range in the latter two cases is twice the driver frequency, since the AOM is double-passed.

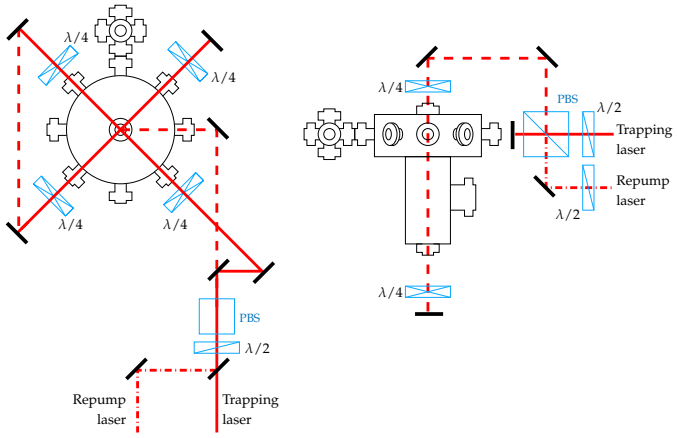

(a) Top view (b) Side view

Figure 4.6: Schematic overview of the diode laser beam paths around the vacuum setup. The dash-dotted beam is the repump beam which propagates at a lower level than the trapping beam until it is overlapped with the trapping beam at the PBS. At the same PBS the vertical MOT beam is split off. The power in the vertical and horizontal beams can be adjusted by the $\lambda/2$-plates. The dashed beams in a) are travelling in a horizontal plane above the vacuum chamber level.

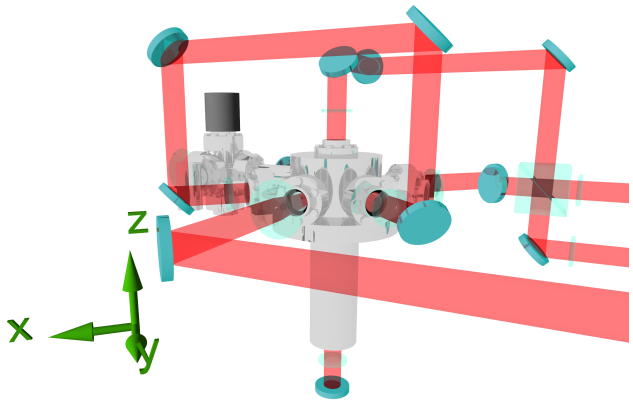

Figure 4.7: 3D rendering of the vacuum chamber including the optical beams. Figure C.3 on page 111 is a colour print of this figure.

4.4 DIODE LASER LOCKING

The diode lasers in the MOT setup are stabilised using polarisation spectroscopy [93–98]. This technique is closely related to the well-known saturated absorption spectroscopy techniques (cf. e. g. Demtröder [99]). Polarisation spectroscopy was chosen because the dispersion shape of the signal is well-suited for locking without requiring any form of dithering.

Polarisation spectroscopy with a single photodiode (PD) was first proposed by Wieman and Hänsch [93] in 1976, where it was used to study the Balmer-β lines of hydrogen and deuterium. Later the Hänsch group used it to study a Ne transition with a pulsed dye laser [100] and in 1980 Hänsch and Couillaud [94] used the technique in an improved setup with two PDs to frequency stabilise a CW dye laser. To our knowledge, Lancaster et al. [95] were the first to use polarisation spectroscopy in the single-PD setup to stabilise diode lasers in a MOT experiment with Rb. The linewidth of their spectra is rather large, but this was improved in the measurements of Pearman et al. [96] and Yoshikawa et al. [97] who used the two-PD setup.

4.4.1 *Theoretical description*

In polarisation spectroscopy one measures the light-induced change in the index of refraction and absorption coefficient of a gas sample. One of the simplest cases to consider is the case of a circularly polarised pump beam that induces an

optical anisotropy in the gas. Due to the change in birefringence and dichroism, a linearly polarised probe beam will experience a change in polarisation, which can be detected by analysing the polarisation of the probe beam with a PBS at an angle of 45° with respect to the polarisation direction and two PDs. Without the presence of the pump beam the two polarisation components are equal and subtracting them results in a zero signal. In the presence of the pump beam, however, the resultant polarisation rotation gives rise to a difference in the signals of the two PDs and therefore to a signal on a flat background.

To describe the change in the probe beam, consider a plane wave that is linearly polarised at an angle ϕ with the x direction in the xy-plane and travelling in the z direction

$$\boldsymbol{E}(z,t) = \begin{bmatrix} E_x(z,t) \\ E_y(z,t) \end{bmatrix} = \tilde{E}_0 \, \mathrm{e}^{i(kz-\omega t)} \begin{bmatrix} \cos\phi \\ \sin\phi \end{bmatrix}. \tag{4.2}$$

This linearly polarised light wave can be decoupled into a right-circular and a left-circular component

$$\boldsymbol{E}(z,t) = E_0(z,t) \left\{ \frac{\mathrm{e}^{i\phi}}{2} \begin{bmatrix} 1 \\ -i \end{bmatrix} + \frac{\mathrm{e}^{-i\phi}}{2} \begin{bmatrix} 1 \\ i \end{bmatrix} \right\}. \tag{4.3}$$

For a gas-cell of length L, the transmitted field can be written as

$$\boldsymbol{E}(z,t) = E_0(z,t) \left\{ \frac{\mathrm{e}^{i\phi}}{2} \mathrm{e}^{ik_+L} \mathrm{e}^{-a_+L/2} \begin{bmatrix} 1 \\ -i \end{bmatrix} + \frac{\mathrm{e}^{-i\phi}}{2} \mathrm{e}^{ik_-L} \mathrm{e}^{-a_-L/2} \begin{bmatrix} 1 \\ i \end{bmatrix} \right\}, \tag{4.4}$$

with $a_\pm$ and $k_\pm$ the absorption coefficient and wavevector of the right-circular $(+)$ and left-circular $(-)$ polarised components, respectively. Both k and a change due to the interaction with the circularly polarised pump beam. For convenience we introduce the average and the difference of the wavevector and the absorption coefficient

$$\begin{aligned} k &= \frac{1}{2}(k_+ + k_-), \quad \Delta k = k_+ - k_-, \text{ and} \\ a &= \frac{1}{2}(a_+ + a_-), \quad \Delta a = a_+ - a_-. \end{aligned} \tag{4.5}$$

Then the electric field of the probe beam can be written as

$$\boldsymbol{E}(z,t) = E(z,t) \, \mathrm{e}^{ikL} \mathrm{e}^{-aL/2} \left\{ \frac{\mathrm{e}^{i\phi}}{2} \begin{bmatrix} 1 \\ -i \end{bmatrix} \mathrm{e}^{iQ} + \frac{\mathrm{e}^{-i\phi}}{2} \begin{bmatrix} 1 \\ i \end{bmatrix} \mathrm{e}^{-iQ} \right\}, \tag{4.6}$$

with

$$Q = \frac{\Delta k L}{2} - \frac{i \Delta a L}{4}. \tag{4.7}$$

The difference signal of the two PD signals is used to lock the laser:

$$\begin{aligned}\Delta I &= I_y - I_x \\ &\propto |E_0|^2 \, \mathrm{e}^{-aL} \cos(2\phi + \Delta k L)\,.\end{aligned} \tag{4.8}$$

Now assume a Lorentzian lineshape for the absorption,

$$\Delta a = \Delta a_0 \frac{1}{1+\zeta^2}, \tag{4.9}$$

with $\zeta = 2\delta/\Gamma$ the ratio between the detuning $\delta = \omega - \omega_0$ and the (possibly broadened) linewidth Γ. From the Kramers-Kronig relations follows that [99]

$$\Delta n = -\Delta n_0 \frac{\zeta}{1+\zeta^2} \tag{4.10}$$

for the index of refraction. Using this relation and $\Delta k = \Delta n \frac{\omega}{c}$, Eq. (4.8) can be written as

$$\Delta I = I_0 \, \mathrm{e}^{-aL} \cos\left(2\phi + \frac{\omega}{c}\Delta n_0 L \frac{\zeta}{1+\zeta^2}\right). \tag{4.11}$$

Using the fact that $\Delta n_0 = \Delta a_0 \frac{c}{\omega}$ and the fact that the cosine is most sensitive at $\phi = \pi/4$ the PD signal can be approximated by

$$\Delta I = -I_0 \, \mathrm{e}^{-aL} \left(\Delta a_0 L \frac{\zeta}{1+\zeta^2}\right). \tag{4.12}$$

It is possible to take into account the birefringence of the windows by adding a term $\exp[-ik_w l]$ to Eq. (4.4) as Pearman et al. [96] have done, but this would only add a linearly increasing background to the final result. However, as will be shown in § 4.4.3, there is no need for such an addition to fit our data.

4.4.2 *Setup*

For each of the diode lasers a fraction of about 5 % of the power is split off from the main beam and sent to a polarisation spectroscopy setup (cf. Fig. 4.4). A schematic picture of such a setup is shown in Fig. 4.8. Again approximately 5 % of the incoming linearly polarised light is split off by a beam sampler as a probe beam. It passes through a 10 cm long glass cell containing a saturated rubidium vapour. Since polarisation spectroscopy is very sensitive to magnetic fields the cell is enclosed in a µ-metal shield. The probe beam enters the polarimeter, which consists of a polarising beamsplitter cube mounted on a rotator and two photodiodes (cf. Fig. 4.9). Most other experiments use a half-wave plate in front of a fixed PBS, but that is unnecessary here because we can rotate our polarimeter.

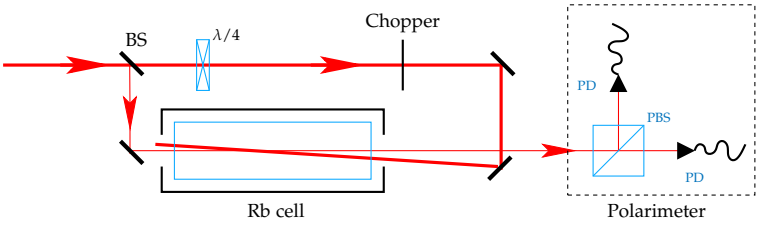

Figure 4.8: Schematic overview of the polarisation spectroscopy setup. The rubidium cell is enclosed in a μ-metal shield. See the text for a detailed description. Figure 4.9 shows the polarimeter in more detail. BS is a 5 % beamsplitter.

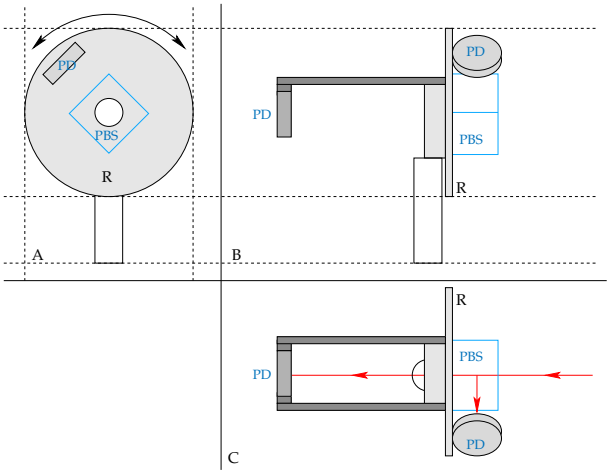

Figure 4.9: A schematic drawing of the rotatable polarimeter in the polarisation spectroscopy setup from the front (figure A), the side (B) and the top (C). R is the rotator.

The PBS and one of the PDs are mounted on a rotator to allow compensation if the incoming polarisation is not vertical or horizontal. It also allows for finetuning of the balance of the two PDs. The main beam acts as the pump beam. It is made circularly polarised by the quarter-wave plate and is modulated by the chopper. It counterpropagates the probe beam to make a Doppler-free setup.

The signals of the two PDs are amplified and then subtracted and the resulting signal is sent to a lock-in amplifier[1]. The error signal of the lock-in amplifier is integrated, after which a tunable DC offset is added. This signal is then fed back to the piezo controlling the grating angle of the diode laser. The DC offset voltage is used to set the grating angle so that the right hyperfine transition for locking can be selected. No feedback to the diode current is applied.

4.4.3 *Polarisation spectra*

In this section polarisation spectra relevant for our experiments will be shown. All data is collected by scanning the piezo in the DL100 with a triangle waveform at a frequency of 25 Hz. The beam diameter is 1.1 mm. For all spectra the power in the probe beam is 6 µW ($s_0 = 0.4$) and the power in the pump beam is 26 µW ($s_0 = 1.7$). The peaks in the spectra are fitted to Eq. (4.12). In each fit of a spectrum the distance between the lines is kept fixed as determined by the splittings shown in Fig. B.2. The height of the peaks, the scan rate (that converts piezo voltage to the detuning in MHz), the position of the peak with the highest F' number, the background level and the linewidth are free parameters. All peaks are assumed to have the same linewidth.

Figure 4.10a shows the ^{87}Rb $F = 2 \rightarrow F' = 1, 2, 3$ polarisation spectrum in the upper trace. The lower spectrum, which is shifted downwards for clarity, is the sum of the signals of the two PDs in the polarimeter divided by two resulting in the Doppler-free saturated absorption spectrum of the transition. For this trace a background signal containing the Doppler profile was subtracted in order to get a flat background signal. To this spectrum a set of six Lorentzian profiles is fitted with the same conditions as mentioned earlier for the polarisation spectra. However, the scan rate and the position of the peaks with the highest F' number are kept fixed at the values found for the polarisation spectrum. Comparing the spectra one observes that the zero crossing of the polarisation signal is indeed at the same position as the peaks of the saturated absorption signal. This is verified for the other spectra as well, although not explicitly shown in the figures. The observed linewidths in the two traces are almost identical as is to be expected, but the steep slope of the polarisation signal at the $F' = 3$ cycling transition shows why this technique is superior for use in our laser lock system. In figure 4.10b the polarisation spectrum of the ^{85}Rb $F = 3 \rightarrow F' = 2, 3, 4$ transitions is shown. Since these levels are more closely spaced the scan voltage on the piezo is reduced by a

1 Femto Messtechnik LIA-BV-150-H

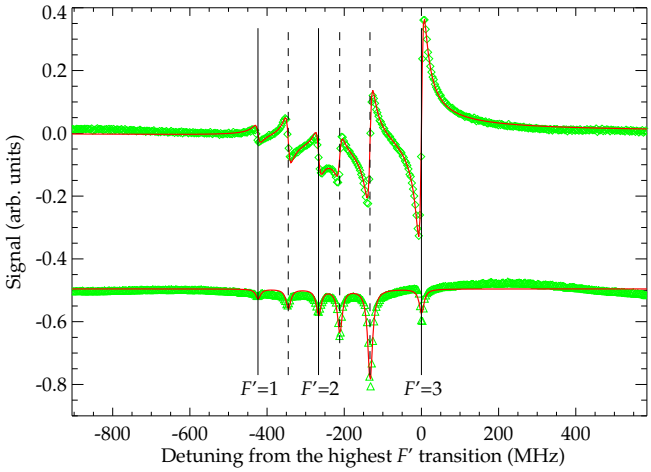

(a)

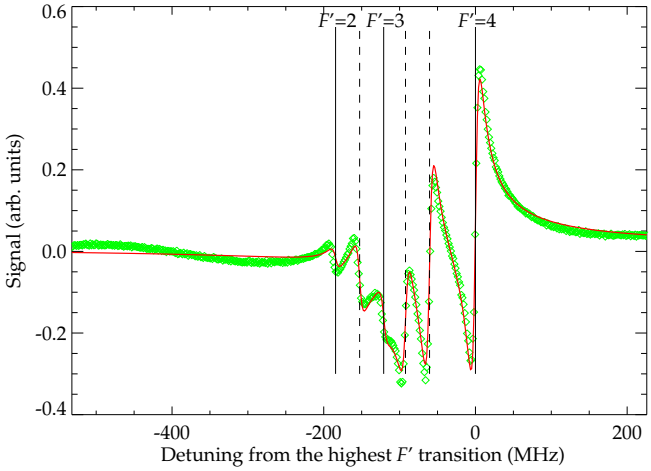

(b)

Figure 4.10: Polarisation spectra for the cycling transitions of Rb. The solid line through the data points is a fit to Eq. (4.12). The solid vertical lines indicate the positions of the F' peaks, the dashed lines indicate the positions of the cross-over peaks. (a): The top trace is the polarisation spectrum of the ^{87}Rb $F = 2 \rightarrow F'$ transitions. In the bottom trace, which is shifted down for clarity, the corresponding saturated absorption spectrum is plotted for comparison. The fitted linewidth for the polarisation spectrum is 14.6 MHz. A set of Lorentzians was fitted to the saturated absorption spectrum. It resulted in a linewidth of 14.0 MHz. (b): ^{85}Rb $F = 3 \rightarrow F'$ transitions. The fitted linewidth is 11.9 MHz.

SPECTRUM	FIGURE	s_0	Γ_f	Γ_{pb}	SCAN RATE
^{87}Rb $F = 2 \rightarrow F'$	(4.10a)	2.1	14.0	10.7	233
^{87}Rb $F = 2 \rightarrow F'$	(4.12)	0.53	9.0	7.5	224
^{85}Rb $F = 3 \rightarrow F'$	(4.10b)	2.1	12.8	10.6	238
^{85}Rb $F = 2 \rightarrow F'$	(4.11a)	2.1	11.9	10.6	233
^{87}Rb $F = 1 \rightarrow F'$	(4.11b)	2.1	18.5	10.7	260

Table 4.1: Summary of the polarisation spectroscopy fit results. For each figure in this chapter the fitted linewidth Γ_f and the calculated power broadened linewidth Γ_{pb} are shown in MHz. The last column shows the piezo scan rate in MHz/V deduced from each fit.

factor of two compared to the previous figure. Notice again the steep slope at the cycling transition. Figure 4.11a shows the spectrum for the ^{85}Rb repump laser. The scan rate is the same as in the case of the ^{85}Rb cycling transition. Note that both in this spectrum and in the ^{87}Rb repump spectrum (Fig. 4.11b) the transition with the highest F' number does not have the largest amplitude. Nevertheless it is still possible to use these transitions for locking.

To show the necessity of the μ-metal shield Fig. 4.12 shows the ^{87}Rb $F = 2 \rightarrow F'$ spectrum with (upper trace) and without (two lower traces) the shield. The data of the upper two traces is taken with a pump power of 4 μW and the upper trace has a linewidth of 9.0 MHz, only a few MHz larger than the natural linewidth of $\gamma/2\pi = 6.065$ MHz. The lower trace was taken with a pump power of 120 μW ($s_0 = 8.0$) and the signal is divided by two in this plot. Using this higher power the dispersive shape of the signal could somewhat be restored, if only for the highest F' level. This can be understood by considering the fact that the presence of an external magnetic field leads to Zeeman precession of the state with highest $m_{F'}$ to other $m_{F'}$ states. Increasing the pump power increases the optical pumping rate and hence reduces this redistribution. From the figure it is clear that the absence of the shield leads to a reduction of the signal amplitude and a shift of the zero crossing of the peaks.

Table 4.1 summarises the fit results. The linewidth found in the fits is indicated by Γ_f and the calculated power broadened linewidth $\Gamma_{pb} = \gamma\sqrt{1+s_0}$ with γ the natural linewidth. The differences between Γ_f and Γ_{pb} are most likely due to collisional effects and the small angle of 33 mrad between the pump and probe beams. The values for scan rate of the piezo in the DL100 are in good agreement with each other.

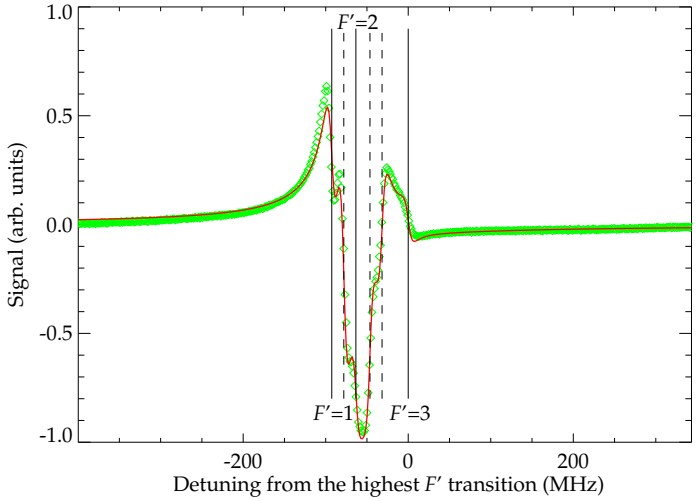

(a)

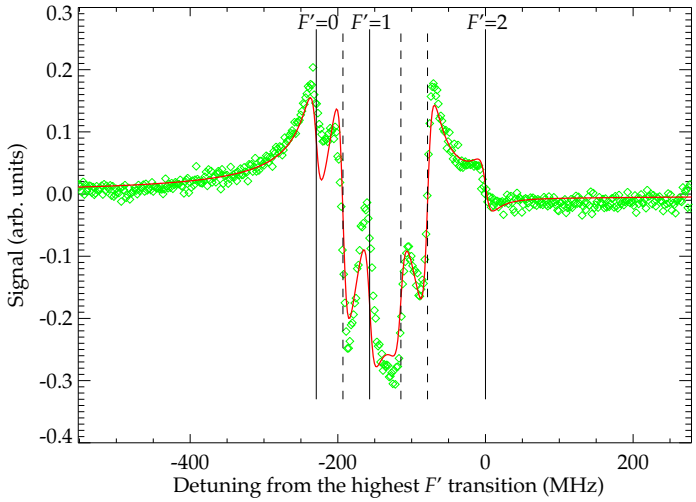

(b)

Figure 4.11: Polarisation spectra of the Rb repump transitions. See Fig. 4.10 for a description of the different lines. (a): The ^{85}Rb $F = 2 \rightarrow F'$ transitions. The fitted linewidth is 12.9 MHz. (b): The ^{87}Rb $F = 1 \rightarrow F'$ transitions. The fitted linewidth is 18.5 MHz.

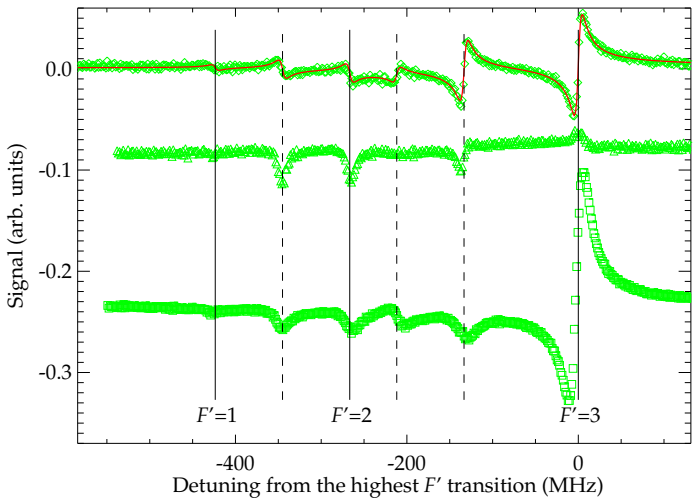

Figure 4.12: Polarisation spectra of the ^{87}Rb $F = 2 \rightarrow F'$ transitions with and without μ-metal shield. The upper trace shows a typical low power polarisation spectrum. The fitted linewidth is 9.0 MHz. The middle trace is taken under the same conditions, but with the μ-metal shield removed. The lower trace is taken at a higher pump power which somewhat restores the dispersive lineshape. The signal level in this trace is divided by two compared to the upper two traces.

4.4.4 *Discussion*

Harris et al. [98] have measured polarisation spectra for Cs and Rb. Their spectra look identical to ours. In their paper they have modelled the spectra by calculating rate equations from the optical Bloch equations. Since their model does not work well for the repump spectra, we have not used it to fit our own spectra. Our measurements improve on the linewidth of 17 MHz as measured by Yoshikawa et al. [97] and are otherwise comparable.

We have compared polarisation spectroscopy to several other methods like Doppler-free saturation spectroscopy and Dichroic Atomic Vapour Laser Lock (DAVLL) [101]. Our conclusion is that polarisation spectroscopy works best, since we do not need the large capture range of DAVLL and the steep slopes of the polarisation signals provide a very stable lock. Furthermore, it is very easy to implement and requires no frequency dithering like saturated absorption spectroscopy. Because the lock signal is the difference of two PD signals this method has intrinsic compensation for laser power fluctuations. Using the setup described in this section the lasers remained frequency locked for hours.

Recently Weatherill [102] has made a similar comparison and he shares our conclusions. Wasik et al. [103] and Petelski et al. [104] claim that their Doppler-free DAVLL setup works better than polarisation spectroscopy. We have reconstructed Petelski's setup to compare both methods and conclude that in our case polarisation spectroscopy has the smallest linewidth and as the figures in this section show we can use almost all transitions for locking. That Petelski et al. conclude the opposite may be due to the lack of magnetic shielding in their polarisation spectroscopy setup.

4.5 TI:SAPPHIRE LASER

The FORTs (cf. § 3.2) in our experiments are made using a Coherent Mira 900 Ti:sapphire ($Ti:Al_2O_3$) laser. With the SW optics set the tuning range of the Mira is approximately $720 - 830$ nm. The Mira is designed to be run in ML-mode, which means that the optical phases of the longitudinal modes inside the cavity are locked together. Through the use of a Kerr-lens [105] this results in the output of a train of short coherent pulses [21] of a few picoseconds with a repetition rate determined by the cavity roundtrip time: $f_{\text{rep}} = \frac{c}{2L} = 76$ MHz, corresponding to one pulse every 13 ns. Note that the lifetime of a Rb atom in the excited state is of the same order, $\tau_{\text{Rb}} = 26$ ns (cf. tables B.1 and B.2). The time-averaged output power P_{Mira} ranges from $0.10 - 1.5$ W. This corresponds to an energy per pulse of $P_{\text{Mira}} / f_{\text{rep}} = 1.3 - 20$ nJ.

Depending on the layout of the internal components the Mira can output pulses of several picoseconds or several hundreds of femtoseconds, referred to as the Mira 900-P and 900-F, respectively. After several unsuccessful trials with the

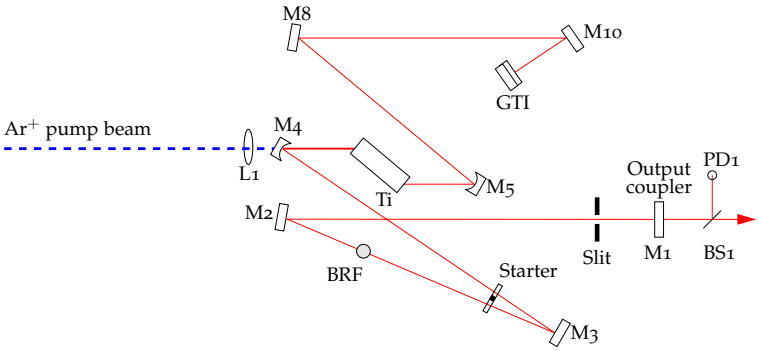

Figure 4.13: Schematic overview of the optics of the Mira laser (adapted from Ref. [108]). BRF: birefringent filter, L1: Focusing lens, M1–M10: mirrors, GTI: Gires-Tournois interferometer, PD1: photodiode, used to monitor output intensity.

900-F we decided to convert to the 900-P setup, since the high bandwidth of the femtosecond pulses could hit a multitude of photoassociation lines present in the wavelength range under investigation, leading to increased atom losses [10, 25–27, 106, 107]. A schematic representation of the internal Mira 900-P optics is shown in figure 4.13. The autocorrelation time τ_{ac} of the pulse is measured to be 1.9 ps. For a pulse shape of the form $I(t) \propto \mathrm{sech}^2\left(\frac{1.76t}{\tau_p}\right)$ this corresponds to a FWHM pulse time τ_p of $0.648\tau_{ac} = 1.2$ ps for a transform limited pulse.

4.5.1 *Beam path*

Figure 4.14 shows a schematic overview of the path of the Mira beam in the experiment. After exiting the laser the beam passes through an OI[m] to minimise reflection of laser light back into the cavity. This is necessary to maintain ML operation, as the ability to mode lock appears to be highly sensitive to reflections of the lenses in the telescope and the front facet of the wavemeter fibre coupler. A telescope reduces the beam diameter to let the beam pass through the AOM which is used as a fast shutter. The zero order half-wave plate in front of it is used to rotate the polarisation back from 45° to horizontal after passing through the OI. The zeroth order of the AOM is sent to a wavemeter[n] in order to monitor its wavelength. The first order passes through a homemade shutter (cf. § 4.7.2) and passes on to the vacuum chamber in the adjacent room. The long beam path allowed the beam to expand in free space, thus avoiding the need of beam expansion optics that could distort the beam profile. In the room with the vacuum chamber the Mira beam is brought to the level of the optical table by a periscope

m Leysop FOI 5/57
n Burleigh Wavemeter Jr

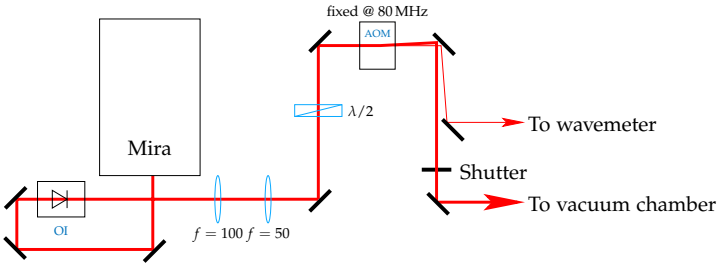

Figure 4.14: Schematic top view of the path of the Mira beam near the laser. The focal distances are given in mm.

and directed to the chamber by several mirrors as shown in figure 4.15. The PBS assures that the incoming polarisation is always horizontal. Before entering the setup an achromatic doublet lens with a focal length of 200 mm was used to focus the beam down to a waist of typically 20 µm (cf. § 4.5.4). The total beam path from the output mirror of the laser to the final focusing lens in front of the chamber is 5.10 m. After exiting the vacuum chamber the beam is blocked by a beam dump.

4.5.2 *Laser stability*

The Mira is pumped by a multiline argon ion laser[o] with a maximum output power of 22 W, typically run at $3 - 10$ W. It has been shown that intensity noise in the dipole trap laser leads to exponential heating of atoms in the trap. Similarly, beam pointing noise leads to heating at a constant rate [109, 110].

Figure 4.16 shows the intensity noise spectrum of the Mira laser when pumped at 3.3 W in the upper trace. The middle spectrum is for Mira in ML mode with a pump power of 6.6 W. In the bottom trace the intensity noise of one of the diode lasers is shown for comparison. In all measurements the average power on the photo diode was the same. It is unclear why the noise level of the mode-locked Mira lies significantly below the CW spectrum. All measurements are performed with a 16 bits spectrum analyser[p]. The PD and its amplifier were homemade. For these measurements the Ar^+ laser is in PowerTrack mode, which is also used during the FORT experiments.

The pointing noise of the dipole trap beam focus is shown in Fig. 4.17. It is measured near the vacuum chamber by splitting the beam and direct both paths to a PD and subtract these signals. One of the PDs is partially blocked by a pinhole. The large peak at 700 Hz is due to vibrations of the turbo pump. Trap frequencies in the radial direction in a FORT are generally in the order of several

o Coherent Innova 400
p Advantest Digital Spectrum Analyzer R9211A

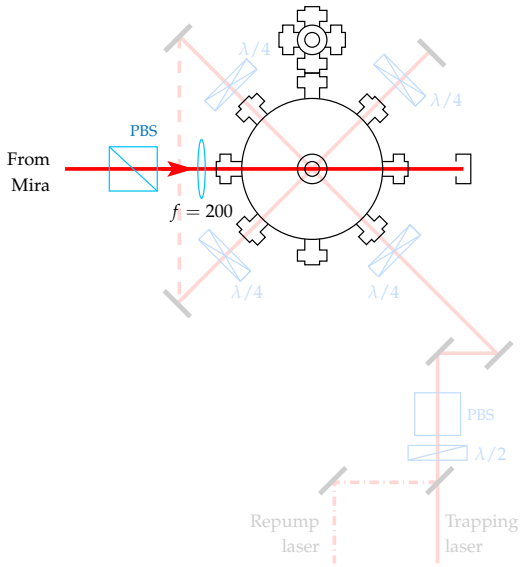

Figure 4.15: Schematic top view of the path of the Mira beam near the vacuum chamber. The focal distance is in mm.

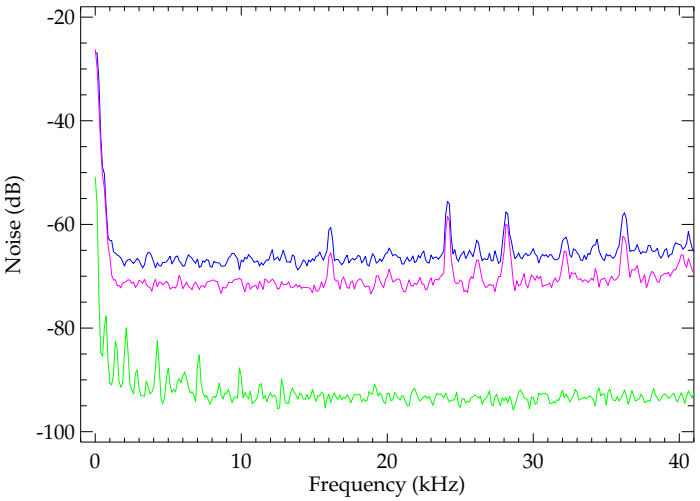

Figure 4.16: Mira intensity noise spectra. The top line is the spectrum of Mira in CW mode at a pump power of 3.3 W, in the middle spectrum Mira is in ML mode at a pump power of 6.6 W. The lower trace is a trace of the diode laser driving the cycling transition. All measurements were taken with the same average voltage of the photodiode.

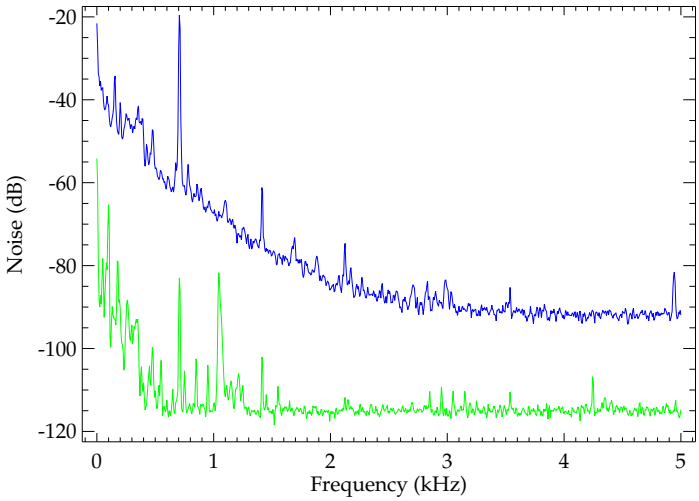

Figure 4.17: Pointing noise spectrum of the Mira ($P_{\text{pump}} = 3.3\,\text{W}$). The lower trace is the spectrum taken with a flashlight in front of one PD (attaining the same voltage on the detector as in the upper trace), with the second PD blocked. This shows the electronic contribution to the noise.

kHz (cf. Table 3.1) . The measurements show that in this range the beam noise will not pose a problem.

In order to investigate the frequency stability of the Mira laser in CW and ML mode the pump beam in our polarisation spectroscopy setup (cf. Fig. 4.8) was replaced with the Mira beam with a power of 0.50 W focused to a long waist using an $f = 50\,\text{cm}$ lens. As shown by Ban et al. [111, 112] one would expect absorption spectra in which the laser repetition rate would show up as a comb when the pump beam was tuned to the D_1 or the D_2 line.

However, it was not possible to show a steady signal of peaks separated by the laser repetition rate, the frequency fluctuations were too large. Therefore we conclude that the Mira central frequency is not stable within approximately 100 MHz, neither in CW nor in ML mode. A possible reason may be the fact that the we do not have a phase locked frequency comb, unlike Ban et al. This was a confirmation of earlier measurements by Vledder et al. [113] who found low-frequency fluctuations on a 20 ms time scale with an amplitude of approximately 30 MHz.

4.5.3 *FORT alignment*

The following procedure was followed to align the FORT beam with the MOT. First the oven was heated to approximately 150 °C in order to increase the amount of vapour in the setup. This allows us to see the scattered light of the laser beams on the CCTV screen (cf. Fig. 4.19). The Ti:Sapph laser is subsequently set to CW mode with a relatively high power of 0.5 W and is tuned to the Rb D_1 or D_2 wavelength, depending on which of the two lines is closest to the wavelength at which the experiments are to be done. With the FORT beam on resonance and the chamber filled with rubidium vapour the position of the beam and even the location of the focus can easily be distinguished.

By making small adjustments to the mirrors in front of the PBS (cf. Fig. 4.15) the FORT beam can be steered through the centre of the MOT by looking at the reduction of MOT fluorescence on the CCTV screen. To make sure that the beam is also centred on the MOT in the (horizontal) dimension that is not visible on the screen, one also has to look for the position with lowest MOT fluorescence. This procedure works quite effectively and is only hampered by the mode hops of the Ti:Sapphire laser that make the beam's scattering flicker.

After this relatively coarse alignment the laser is tuned to the desired wavelength. To compensate for the resulting displacement of the beam the final steps of the alignment are carried out by looking at the position and the intensity of the FORT fluorescence with respect to that of the MOT on the CCD image. Using a micrometre screw to adjust the position of the FORT lens, the axial position of the FORT can be adjusted so that it coincides with the centre of the MOT.

4.5.4 *Measuring the size of the beam waist*

In our experiments three methods were used to determine the focus size of the FORT laser beam. Since the focus lies inside the vacuum system, it can not be determined directly.

The first method used, involves the creation of an image of the focal plane using an achromatic doublet lens with a 20 cm focal length and an image distance of approximately 10 m. The image is recorded on the CCTV camera (which obviously is not in the position indicated in Fig. 4.19 in this measurement). By translating the imaging lens and recording several images, the minimal focus size can be found by fitting the beam diameters found from the images to

$$w(z) = w_0 \sqrt{1 + \left(\frac{(z - z_0)\lambda M^2}{\pi w_0^2} \right)^2}. \tag{4.13}$$

A typical measurement is shown in Fig. 4.18. From the fit we find $w_0 = 21.5 \pm 1.2\,\mu\text{m}$ and $M = 1.12 \pm 0.05$.

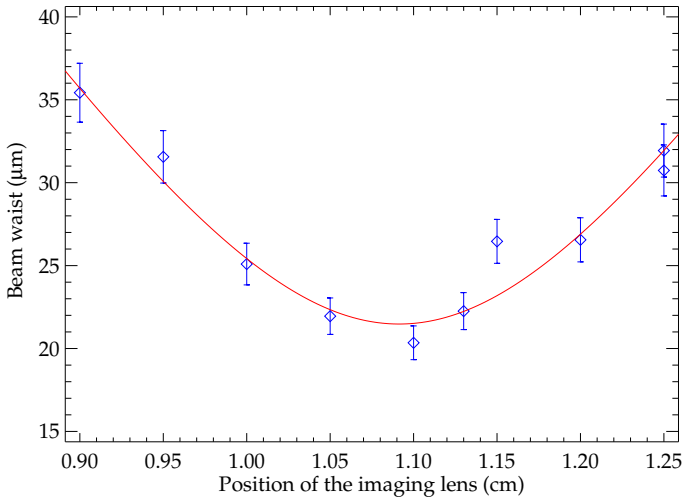

Figure 4.18: Measurement of the Mira waist at $\lambda_{\text{Mira}} = 795\,\text{nm}$ by imaging the focus onto the CCTV camera for different positions of the imaging lens. The line is a fit to Eq. (4.13) with $w_0 = 21.5\,\mu\text{m}$ and $M = 1.12$.

There are, however, several drawbacks to using this method. First, the Mira beam has to be attenuated a lot, which involves placing several ND filters into the beam path, which may distort the beam. Furthermore, the AOM in the Mira path has to be turned off. Also the CCTV camera and the beam imaging lens need to be repositioned for every measurement. Finally the number of images that needs to be taken is higher compared to our second method, described now.

In this method, the measurement of the $1/e^2$ beam waist involves the translation of a knife edge through the beam and recording the transmitted power as a function of x, the position in the beam. The waist at position z can be found by fitting the transmitted power to

$$P(x) = \frac{P_0}{2}\left(1 \pm \text{Erf}\left(\frac{x}{\sqrt{2}\,\sigma}\right)\right), \tag{4.14}$$

where σ is the half the $1/e^2$ radius of the beam and thus the measured waist is $w(z) = 2\sigma$. Of course it would have been possible to determine the waist by inserting a mirror in front of the chamber and do a knife edge measurement directly. However, due to lack of space near the vacuum chamber this was not practical. Furthermore, such a direct determination would require several measurements of the beam width to be sure that the smallest waist was found. Therefore we developed the following method which involves only two knife edge measurements of the beam waist $w(z)$ at positions z_1 and $z_2 = z_1 + d$ after

passing through the vacuum chamber. From these two widths and the distance between them the minimum waist of the beam, w_0, and its position relative to z_1 can be determined using Gaussian optics. Appendix A shows the details of the calculation. The measurement was first done by inserting a mirror in front of the vacuum chamber and measuring near the focus. By repeating the measurements after the beam passed through the chamber and finding the same focus size, the Gaussian propagation of the beam was verified. Uncertainties in this method are the accuracy with which the distance d between z_1 and z_2 can be determined, and the fact that the laser beam may not be perfectly Gaussian as indicated by the factor M in Eq. (4.13). Using this method the beam waist was determined to be $20.0 \pm 1.2\,\mu m$. In practice the second is the least involved of the two methods. All later measurements were taken in this way.

The third way to measure the beam waist involves the measurement of the radial trap frequency and is discussed in Chapter 6.

4.6 THE IMAGING OPTICS

Infrared-sensitive cameras are very important for the experiments, both in a qualitative and in a quantitative way. In our experiments, two cameras are used. The setup contains a simple CCTV camera for alignment purposes and a low-noise triggerable liquid-nitrogen cooled CCD camera for quantitative measurements. Both will be described below. Figure 4.19 shows the imaging setup. In order to suppress stray light from the Mira beam entering the CCD a bandpass filter[q] around 780 nm with a FWHM of 10 nm was inserted. The fast shutter S replaces the original shutter of the CCD (cf. § 4.6.2). Lenses L_1 and L_2 are mounted on flip mounts and are never used simultaneously. The former is generally used when imaging the FORT onto the LN CCD whereas the latter is used when imaging the MOT. The lenses are arranged in such a way that the object distance for one is the image distance for the other and *vice versa*. Both lenses have a focal distance of 100 mm. The fraction of light that is imaged onto a camera is determined by the solid angle subtended by the lens, which is, for example, for lens L_1

$$\eta_{L_1} = \frac{\pi r_{L_1}^2}{4\pi s_1^2}, \tag{4.15}$$

with r_{L_1} the radius of lens L_1 or the radius of the window, whichever is smallest and s_1 the object distance as shown in Fig. 4.19. This yields $\eta_{L_1} = 3.3 \cdot 10^{-3}$.

The PBS behind L_3 splits the fluorescent light of the MOT into two parts, one directed to the CCTV camera, the other to a PD. The MOT fluorescence is randomly polarised, therefore the PBS splits the light into equal parts. The photodiode signal is used to monitor the MOT loading process during the experiments.

q Thorlabs FB780-10

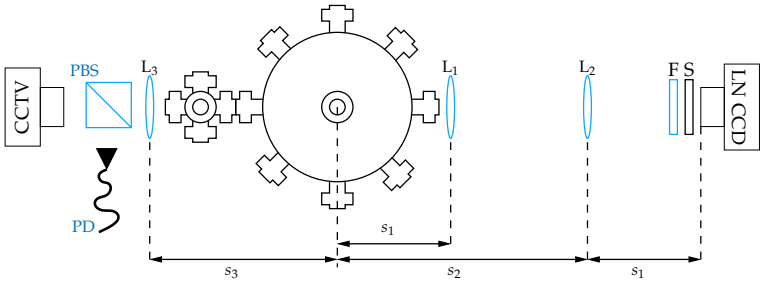

Figure 4.19: The imaging setup consists of a CCTV and a liquid-nitrogen-cooled CCD camera. F is the bandpass filter, S is the Uniblitz shutter mentioned in § 4.6.2. The object distances are $s_1 = 16\,\text{cm}$, $s_2 = 27\,\text{cm}$, $s_3 = 31\,\text{cm}$. Depending on the measurement being done either lens L_1 or L_2 is used. The focal distances are $f_1 = 100\,\text{mm}$, $f_2 = 100\,\text{mm}$ and $f_3 = 60\,\text{mm}$.

4.6.1 *CCTV camera*

The CCTV camera has a CCD array of $6.3 \times 4.9\,\text{mm}$ with 384×288 pixels (i. e. a pixel size of $16\,\mu\text{m} \times 17\,\mu\text{m}$) and is connected to a TV screen and a frame grabber card[r] (cf. Fig. 4.22). It is used to monitor and align the MOT, but also facilitates initial alignment of the FORT beam on the MOT and measurement of the waist of the FORT beam, as described earlier.

4.6.2 *LN CCD camera*

In the early stages of the experiment, attempts have been made to detect the atoms in the FORT using a PD. Unfortunately this did not result in measurable signals. Therefore, a liquid-nitrogen-cooled CCD camera[s] was used for high quality imaging of the atoms in the FORT. The CCD chip[t] has an area of 512×512 pixels with a pixel size of $27\,\mu\text{m} \times 27\,\mu\text{m}$. The CCD has a typical dark current of $1.0\,\text{nA/cm}^2$ at 20 °C, which is reduced by a factor of 10^9 at liquid nitrogen temperature (77 K). At room temperature and a wavelength of 780 nm the quantum efficiency is 55 %. However, the CCD is operated at a temperature of 153 K and the quantum efficiency is known to go down with lower temperatures. Based on the work of Jorden and Oates [114] we estimate the quantum efficiency to be 15 percent point lower at 153 K. The full well capacity of the sensor is $5 \cdot 10^5$ electrons and the readout noise is 8 electrons. The dynamic range relative to readout noise is 62 500 : 1. The ST-130 control box of the camera has a 16 bit AD converter and is connected to the relatively old imaging computer because the

r Pinnacle/Miro DC10
s Princeton Instruments LN/CCD-512TKBM/S
t Back-illuminated inside Tektronix TK512

ISA card that provided the connection to the computer was only supported by an older version of the imaging software[u] that only runs on MS Windows 95. The control box also contains the thermostat that keeps the CCD at a temperature of 153 K. A schematic representation of the imaging setup can be found in Fig. 4.19.

The original shutter in the LN CCD camera did not function according to specifications. Its opening and closing times turned out to be erratic and too long for some of the experiments. Therefore a fast shutter[v] was bought (S in Fig. 4.19). The opening and closing times of this shutter are 3.0 ms and 5.0 ms respectively. The minimal exposure time including opening and closing is 10.0 ms.

4.7 LASER BEAM SHUTTERS

As mentioned in § 4.3, AOMs are used as shutters to block the laser light during parts of the experimental runs. However, since the extinction ratio of an AOM is of the order of 10^{-3} a mechanical shutter is needed to fully extinguish a beam. In this section two types of shutters will be discussed. One design is based on the actuator arm of a computer hard drive and the other is based on a Fleishmann model train railway switch. Design criteria for the shutters were:

- open/close times of ≈ 1 ms
- repetition rates of a few hundreds of Hz, so an open-close cycle can be completed fast
- low jitter after an input trigger pulse
- robustness
- low-cost

Because of the inertia of the shutter 'flag', the first two requirements are the most difficult to satisfy simultaneously.

4.7.1 *Hard disk shutter*

After working for some time with shutters based on a loudspeaker [115] we were dissatisfied by their short lifetimes and their frailty. Therefore, we decided to develop our own shutters based on a computer hard drive. In a computer hard drive data is stored on a series of rotating circular platters by a recording head mounted on an arm. The arm is moved by actuating a voice coil inside a static magnetic field generated by two permanent magnets. The speed at which data

u Princeton Instruments Winview 1.6.2
v Uniblitz VS25-S2-T1 with VCM-D1 control unit

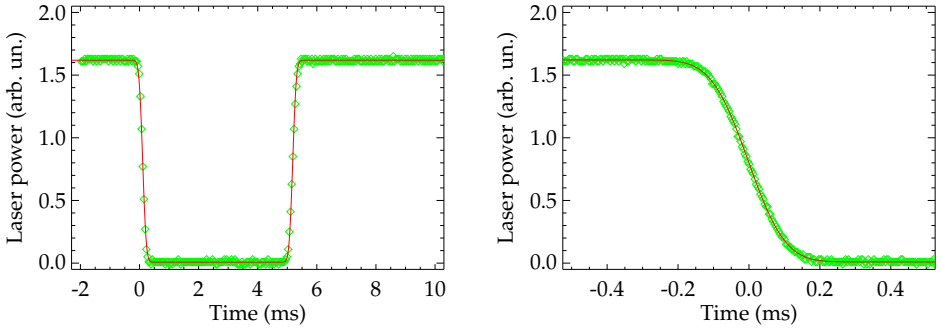

Figure 4.20: Timing measurements of the hard disk shutter. The left figure shows a closing-opening cycle of the shutter. The figure on the right zooms in on the closing slope. The lines are a fit to Eq. (4.14).

can be addressed on the disk depends, among others, on the speed at which the arm can be moved over the platters.

By removing the platters from the hard drive and stripping the casing down to a minimum size the voice coil can be connected to a circuit that can deliver high currents for a rapid rotation of the arm.

Basically this type of shutter satisfied all our criteria. However, it has two main drawbacks, the first being the large vibrations passed to the optical table on which the shutter is mounted. This is a result of the high speed at which the arm hits the plastic buffer at the end of its trajectory. Covering this buffer with felt did not sufficiently reduce the vibrations. By mounting the shutter on an arm that was not connected to the optical table, however, this problem was solved.

The second most important drawback is the rather bulky size of the shutter. It does not allow for easy mounting, especially since mechanical coupling to the optical table is not desirable. We also found that the high currents going to and through the voice coil generated electromagnetic stray fields that could sometimes interfere with other sensitive electronics in the setup.

Timing measurements for the shutter are shown in Fig. 4.20. Figure 4.20a shows the closing and opening of the shutter, Fig. 4.20b zooms in on the downward slope of the first figure. The slopes are fitted to an equation similar to Eq. (4.14) where the position variable x has been replaced with time. This yields an closing-opening time of 5.078 ± 0.001 ms and a closing time of 0.0820 ± 0.0003 ms. The beam waist at the location of the shutter is 0.38 mm. At around the same time, Maguire et al. worked on an equivalent design [116–118].

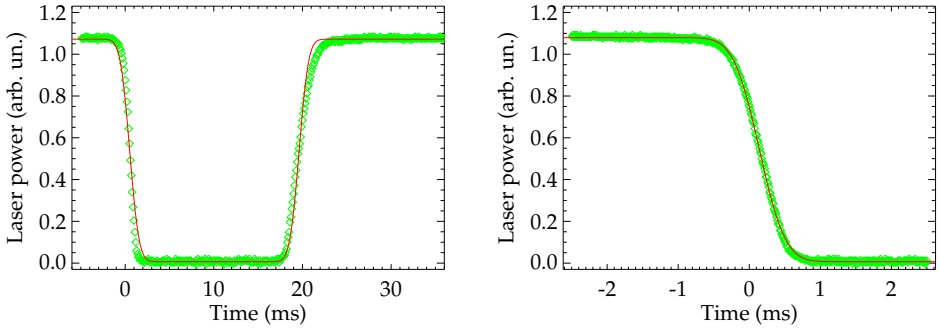

(a) (b)

Figure 4.21: Timing measurements of the Fleishmann shutter. The left figure shows a closing-opening cycle of the shutter. The figure on the right zooms in on the closing slope. The lines are a fit to Eq. (4.14).

4.7.2 *Fleishmann shutter*

Because of the drawbacks of the hard disk shutter, a different approach was taken based on model train railway switches[w]. Such a switch consists of two coils that can be powered independently and an arm that moves inside the coils. On the arm of the switch a fan of blackened aluminium is mounted. The switch itself is mounted on a standard post and placed in a postholder with a rubber damped base in order to reduce the transmission of vibrations to the optical table.

At the heart of the electronics that drive the switch resides a dual one-shot[x], which has an output that, after triggering, remains stable for a time determined by a connected resistor and capacitor. During this time the flag moves. After that no current is running through the coils, resulting in a longer lifetime of this shutter compared to the hard disk shutter where the voice coil needs to be powered constantly. By implementing a dual one-shot for each of the solenoids in the Fleishmann shutter the flag can be moved in both directions.

Measurements of the closing and opening times are shown in Fig. 4.21. Similarly to the measurements of the hard disk shutter the slopes are fitted to Eq. (4.14), yielding a closing-opening time of 19.120 ± 0.007 ms and a closing time of 0.287 ± 0.001 ms for the same beam waist as mentioned earlier.

This type of shutter satisfies all of the criteria mentioned at the beginning of this section except for the repetition rate requirement. Because of the rather large mass of the flag one has to wait 19 ms before the motion of the shutter can be

w Fleishmann N Piccolo 9195
x Type 74LS123

reversed. In experiments where a shorter timing is required, the shutters are left open and only the AOMs are used. The fact that the closing time of the Fleishmann shutter is also larger than that of the hard disk shutter presents no problem, since the AOMs take care of the fast switching.

4.8 MEASUREMENT AND CONTROL HARDWARE

Two computers are used in the experiments. One, the Imaging Computer, is used solely for the image acquisition of the CCD cameras (cf. § 4.6). The other PC takes care of the timing of the experimental sequences and is called the Control Computer. Many aspects of the experiments require precise timing in the order of milliseconds. This timing was realised partly in hardware and partly in software. The Control Computer has an AMD Athlon XP 3000+ processor and 512 MB of RAM and was equipped with a PCI data acquisition (DAQ) board[y] with 8 digital input/output (DIO) lines, 16 analog inputs, 2 analog outputs (AOs) and 2 counter/timers. Figure 4.22 shows a schematic representation of the measurement and control hardware. The AO connection to the repumper AOM allows for the generation of intensity ramps (cf. Fig. 4.24). The AO connection to the trap laser is connected to the frequency input of the AOM which controls the detuning of the MOT (and probe) light (cf. Fig. 4.5 in § 4.3 for details). The DIO line to the external synchronisation input of the LN CCD camera triggers the camera to record an image if the Imaging Computer had previously armed the camera. The image is then stored on the Imaging Computer. The DIO line to the MOT coils is connected to the switch discussed in § 4.2.

y National Instruments PCI-6024E

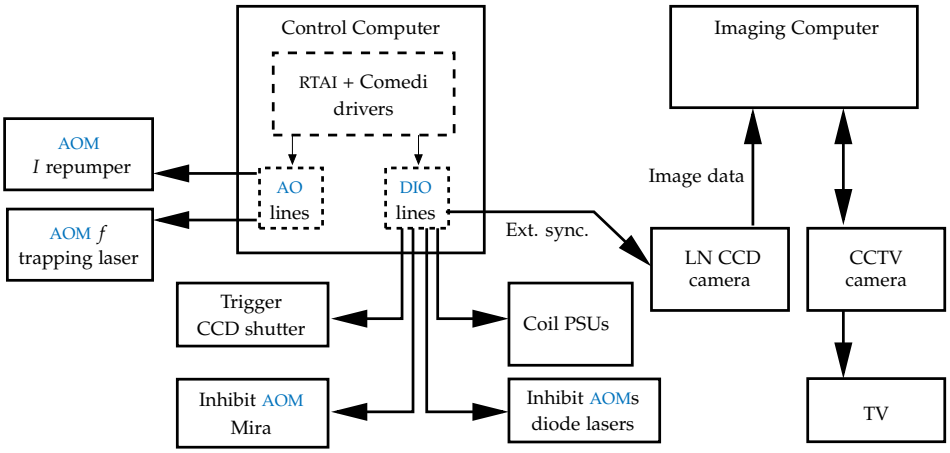

Figure 4.22: Schematic overview of the measurement and control computers and the way they are connected to the different AOMs and other experimental apparatuses. Refer to Figs. 4.4 and 4.14 for the location of the AOMs in the beam paths.

4.9 TIME-SEQUENCING SOFTWARE

Because the DAQ card in the Control Computer has no onboard memory in which to store a sequence of DAQ commands, the timing of the digital and analog lines must be done by software. Ordinarily such a scheme depends on how fast the computer can handle interrupts. In the most generally used operating systems there is no guarantee that such an interrupt will be serviced within a specified time. Since this is not desirable, a solution was developed based on Real-Time Application Interface for Linux (RTAI) [119]. The drivers for the hardware were provided by the Comedi project [120]. In this section our software timing solution is explained in more detail.

4.9.1 *Real-time operating systems*

Most computers used nowadays are run so-called general-purpose operating systems. These OSs allocate all tasks (also called processes or threads) an equal share of the total processing time in order to achieve good average performance. Therefore, there is no guaranteed response time for any of the processes and there is no way to be certain that a task starts (or finishes) at the designated time. This results in unpredictable latencies. Since the timing in our experiments should generally be done with a resolution of the order of about 100 µs, some sort of control over these latencies must be found. This is done by a real-time operating system. These OSes can be found in health care computers, robotics devices, etc.

Many definitions of a real-time operating system exist. A general one that applies to our present situation is [121]:

> A real-time operating system is able to execute all of its tasks without violating *specified* timing constraints.

The timing constraints in our experiments are two-fold. First, the DAQ instructions must be handled fast, i. e. we want low latencies, the instructions must be processed with the highest priority. Furthermore, the maximum latency of handling interrupts for example, must be known. Second, the system must behave deterministically, i. e. the response of the system must be predictable. The duration of instructions must be guaranteed to be within certain limits. In order to provide such control real-time operating systems like VXworks or QNX were developed. Drawbacks of these products are their cost and the fact that they usually only support a restricted set of hardware platforms.

4.9.2 *RTAI and LXRT*

In order to address the concerns mentioned above the Real-Time Application Interface for Linux (RTAI) was developed by the Dipartimento di Ingegneria Aerospaziale - Polytecnico di Milano [119, and documents linked there]. The real-time RTAI Linux kernel is quite easy to install [122] and basically treats the standard Linux kernel as a low-priority real-time task. Furthermore, it provides a real-time hardware abstraction layer that is used to intercept and process system interrupts. This combination allows for real-time scheduling while still allowing non real-time tasks (all other programs, but also drivers) to function as if nothing has changed. The Comedi drivers that do the actual communication with the DAQ hardware are patched during the RTAI installation to allow them to address the card in real-time.

RTAI provides an extra advantage compared to the other real-time product for Linux RTLinux [123], namely that the use of the Linux real-time (LXRT) extension module allows real-time programs to run in user space instead of kernel space [119, 124, 125]. Only those parts of a program that really need real-time performance work in kernel space. This greatly reduces the risks that an ill-programmed application can crash the whole system and also simplifies programming and debugging significantly. The cost is a slightly increased overhead. However, this proved not to be a problem in our situation.

Two real-time timing modes exist in RTAI, the periodic mode and the oneshot mode. The periodic mode is specially suited for real-time sequences that have to be repeated with high precision timing, e. g. a stroboscope light. The oneshot mode is best used when the timing of the real-time task is not a multiple of some base time. This is the mode used in our program. The smallest guaranteed time step using our program was measured to be 20 µs.

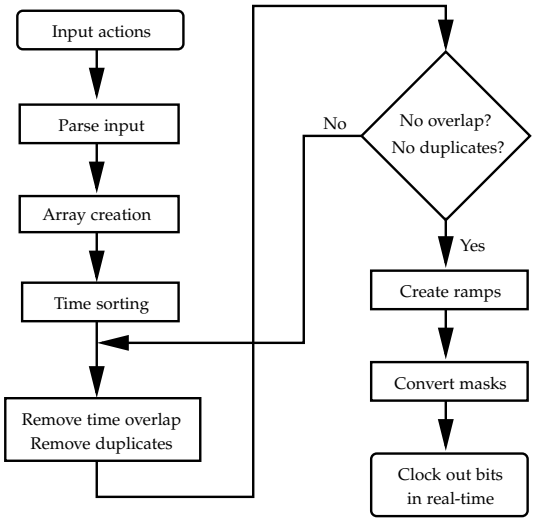

Figure 4.23: Schematic of the structure of the time-sequencing software.

The time-sequencing program we developed using LXRT and the patched Comedi drivers will be described in the following section. For this program we used RTAI v.3.5, Comedi CVS of 13-06-2007 and Linux kernel v.2.6.17.3, all installed on Slackware Linux v.11.0.

4.9.3 *General layout of the time-sequencing program*

The central concept of the sequencing program is the "action". Such an action can be something like "Turn the FORT on for 200 ms", or "Turn off the MOT after 40 ms, ending with a detuning ramp of 10 ms from $\delta = -12$ MHz to -30 MHz for the MOT trapping laser". Internally the program disseminates such an action into a set of start times, durations and associated AO and DIO bit levels. The *Probe On* action for example, consists of entries that turns on the MOT beams at a given time and for a given duration by flipping the appropriate DIO bits for the AOMs. It also sets the detuning of the primary MOT laser to zero by sending the correct voltage to the appropriate AOM (cf. § 4.3) a few ms in advance. Furthermore, it makes sure that the ExtSync line of the LN CCD is triggered 14 ms before probing to enable the old slow shutter in the camera to open. Finally it also triggers the fast shutter in front of the LN CCD 4 ms before the probe light is turned on to allow it to open.

The general layout of the measurement sequencing program is as follows (cf. Fig. 4.23). The user supplies a file containing some constant parameters like the IDs of the devices to be used. This is followed by a list of actions together with

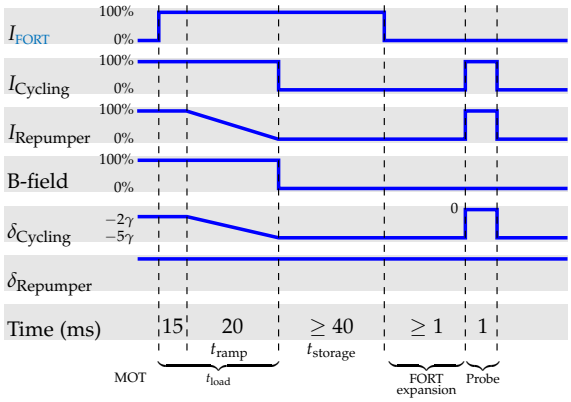

Figure 4.24: Typical timing of an experiment. Durations are in ms.

the associated timings and, if necessary, the appropriate detuning. The program parses this file and generates a list of start times, durations, and AO bit values and DIO bit masks. The list is time sorted, time overlap between entries is detected and duplicate entries are removed. Then the list is checked for jumps in AO values between two time steps, since these indicate that an AO ramp should occur. In that case the list is subdivided into smaller time steps with the appropriate increase or decrease of AO bit values to generate the ramp. Finally the DIO bit masks are converted to the actual bits that need to be clocked out.

After this preprocessing every AO and DIO bit setting is stored in an array together with the start time and the duration of each state. This array is sent to the core of the program, a hard real time function that is scheduled in RTAI's oneshot mode. The real-time function walks through this array and for every element it records the present time in nanoseconds as returned by the OS. Subsequently it sends out the AO and DIO bits, after which it goes to sleep for the remainder of the duration as stored in the array. In the next step the recorded present time can then be compared against the previously stored time incremented by the duration to check for any timing anomalies. After the last entry in the array the function leaves hard real-time and the program exits.

4.9.4 *Timing of the experiments*

The sequencing software described in the previous section is used to control the timing of the experimental runs. A typical timing scheme is shown in Fig. 4.24. First the MOT is loaded for approximately 20 s. Then the Mira beam is turned on and the FORT starts to load. The FORT loading can be enhanced by a reduction of the repump light intensity and by detuning the MOT trapping laser further from resonance (cf. § 5.1). The ramp duration t_{ramp} is typically 20 ms.

After the FORT is loaded the diode laser beams are turned off by sending an inhibit signal to the AOMs and the MOT magnetic field is turned off as well. Since only the FORT light is switched on, this period is referred to as the storage time. During this stage of the experiment, the untrapped MOT atoms drop due to gravity. This stage takes at least $t_{\text{storage}} = 40\,\text{ms}$, which is the time it takes for an atom to fall outside the region of the MOT beams, so that it will not be detected by the probe light.

Following the storage period, the atoms in the FORT are released from the trap and detected after a brief expansion time by turning on the two MOT lasers. The intensity of both lasers is set to the highest possible value and the detuning of the trapping laser is adjusted to zero in order to generate as much fluorescence as possible. The typical probe time is 1 ms to make sure that the atom cloud is not disrupted, e. g. by the creation of optical molasses.

After probing the atoms in the FORT the experiment is "reset" by turning all lasers off and let all atoms leave the detection region. This phase usually lasts 100 ms and is followed by the loading of the MOT for the next measurement.

4.10 MOT PROPERTIES

The MOT is the workhorse in the field of atom optics and it is not much different in our lab. It is the starting point of FORT experiments because it is a source of atoms that are cold enough to be caught in the dipole traps. In this section the basic properties of the MOT atoms will be presented.

4.10.1 *Number of atoms*

The number of atoms in the MOT can be determined in several ways. One is using the specs of the LN CCD camera (cf. § 4.6.2) that captures the fluorescence of the atoms during the probe phase. With a full well depth of $5 \cdot 10^5$ and a 16 bit detector we have 7 electrons per ADU (analog-digital converter unit, sometimes also called grey level). With a quantum efficiency of 45 % the number of photons per ADU is

$$\eta_{\text{CCD}} = 15.6. \tag{4.16}$$

The fluorescence f (in Watt) registered by the CCD depends on the number of ADUs, N_{CCD}, in the following way

$$f = N_{\text{CCD}}\,\eta_{\text{CCD}}\,\frac{\hbar\omega}{\Delta t_{\text{probe}}}, \tag{4.17}$$

with $\hbar\omega$ the energy per photon and Δt_{probe} the duration of the probe pulse. The total number of atoms is given by

$$N = \frac{f}{\hbar\omega\,\eta_{L_1}\,\rho_{ee}\,\gamma}, \tag{4.18}$$

where γ is the natural linewidth, η_{L_1} is the geometrical detection efficiency of the imaging lens as defined in Eq. (4.15) and ρ_{ee} is the fraction of atoms in the excited state (Eq. (3.26)). Therefore the number of atoms is[z]

$$N = \frac{N_{\text{CCD}}\,\eta_{CCD}}{\Delta t_{\text{probe}}\,\eta_{L_1}\,\rho_{ee}\,\gamma}. \tag{4.19}$$

When calculating ρ_{ee} note that the values for the saturation intensity I_{sat} in Appendix B are for the cycling transitions only. For the more complex environment of a MOT Dinneen et al. [126] found a value of $10.5\,\text{mW/cm}^2$ and $9.1\,\text{mW/cm}^2$ for ^{85}Rb and ^{87}Rb, respectively, based on measurements of the photo-ionisation cross-sections. Recently Shah et al. [127] found $I_{\text{sat}} = 9.2 \pm 1.7\,\text{mW/cm}^2$ for ^{87}Rb. Also note that in this discussion scattering of light from the repump beam has been neglected.

A second method that is used to find the number of atoms in the MOT involves the collection of the fluorescence on a calibrated photodiode or power meter, in which case N can be calculated from Eq. (4.18) directly. For a ^{85}Rb (^{87}Rb) MOT we found $N = 6 \cdot 10^8$ atoms ($N = 1 \cdot 10^9$ atoms). This method could not be used to determine the number of atoms in the FORT because the number of atoms in the FORT is typically a factor of 10^3 to 10^4 lower than in the MOT. At the position of the LN CCD the power of the FORT fluorescence would be in the order of a few nW. It is possible to detect this using a photomultiplier tube. However, we did not have one in our experiment.

4.10.2 *Density and shape*

A typical fluorescence image of the MOT is shown in Fig. 4.25. The MOT cloud was allowed to expand for 18 ms before detection. A 2D Gaussian is fitted to the data from which the cloud radii in the vertical and horizontal directions are found. These can be used to find the density of atoms in the MOT according to

$$n(\boldsymbol{r}) = \frac{N}{(2\pi)^{3/2}\,\sigma_x\sigma_y\sigma_z}\,\mathrm{e}^{-\left((\frac{x}{\sigma_x})^2+(\frac{y}{\sigma_y})^2+(\frac{z}{\sigma_z})^2\right)}, \tag{4.20}$$

with σ_i the $1/\mathrm{e}^2$ radius of the cloud in direction i. Because the magnetic field gradients in the x and y direction are equal it is justified to set $\sigma_x = \sigma_y$. For the cloud in Fig. 4.25 we find $\sigma_x = 2.0\,\text{mm}$ and $\sigma_z = 2.0\,\text{mm}$. This yields a peak density of $n_0 = 2 \cdot 10^{10}\,\text{cm}^{-3}$.

z Note that when using this equation with LN CCD data the 55 % transmission of the band pass filter must be taken into account (cf. § 4.6).

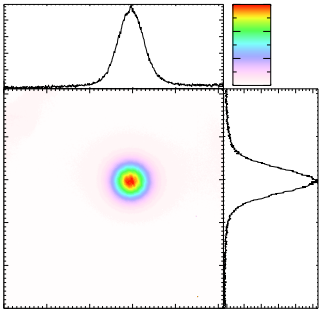

Figure 4.25: Fluorescence image of the MOT taken after an expansion time of 18 ms. The trapping laser detuning is 24 MHz. Figure C.4 on page 111 is a colour print of this figure.

4.10.3 *Temperature*

The temperature of the MOT atoms can be found by allowing the cloud to expand ballistically by turning off both diode lasers and the magnetic field. Assuming a Maxwell-Boltzmann distribution of the velocity of the trapped atoms, the temperature of the sample can be deduced by determining the radius of the cloud as a function of the expansion time t:

$$\sigma(t) = \sqrt{\sigma_0^2 + \frac{k_B T}{m} t^2}, \tag{4.21}$$

where m is the atomic mass and σ_0 the initial radius of the cloud. The same technique will be used to measure the temperature of the FORT in Chapter 5. Figure 4.26 shows a typical measurement for both isotopes. From the fit to Eq. (4.21) we find a temperature of $134 \pm 2\,\mu K$ and $160 \pm 3\,\mu K$ for ^{85}Rb and ^{87}Rb respectively. These values are very reasonable considering the fact that the Doppler temperature of rubidium is 140 µK. The initial radius of the cloud is 0.55 ± 0.02 mm and 0.68 ± 0.02 mm for the respective isotopes. For this measurement the MOT was loaded at a detuning of -2γ, followed by a detuning ramp of $t_{ramp} = 20$ ms to -5γ (cf. § 4.9.4).

The temperature of the atoms in a MOT depends on the detuning of the trapping laser light as shown in Fig. 4.27, where two temperature measurements are shown, one of a MOT loaded at a detuning of $-\gamma$ and the second loaded at -5γ. In a more general way the dependence of the temperature of a multilevel atom trapped in a MOT as a function of laser light intensity and detuning can be written as [128–130]

$$\frac{k_B T}{\hbar \gamma} = C_{\sigma^+\sigma^-} \frac{\Omega^2}{|\delta|\gamma} + C_0, \tag{4.22}$$

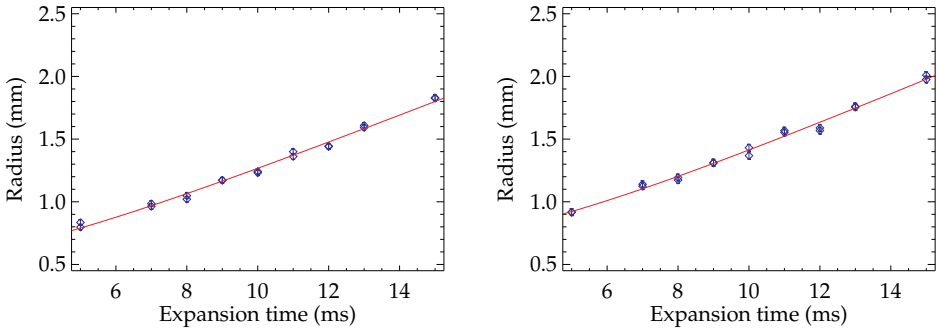

(a) ^{85}Rb (b) ^{87}Rb

Figure 4.26: Temperature measurements of the MOT for both isotopes using ballistic expansion. The lines are fits to Eq. (4.21), from which a temperature of 134 µK and 160 µK is found for the respective isotopes.

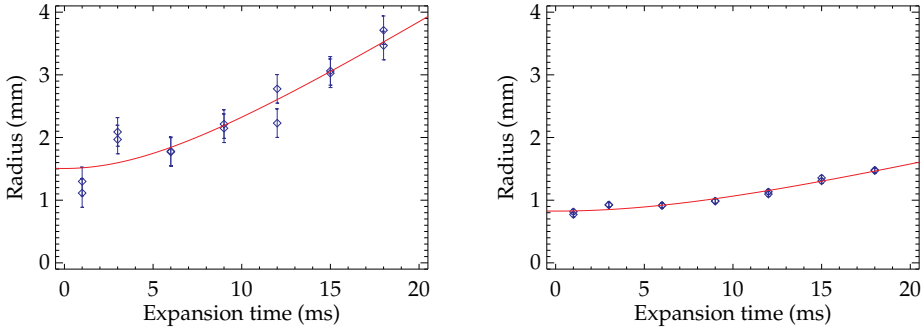

(a) $\delta = -6\,\mathrm{MHz}$, $T = 320 \pm 30\,\mu\mathrm{K}$ (b) $\delta = -30\,\mathrm{MHz}$, $T = 46 \pm 2\,\mu\mathrm{K}$

Figure 4.27: Two ^{85}Rb MOT temperature measurements at different detunings of the trapping laser, plotted on the same scale.

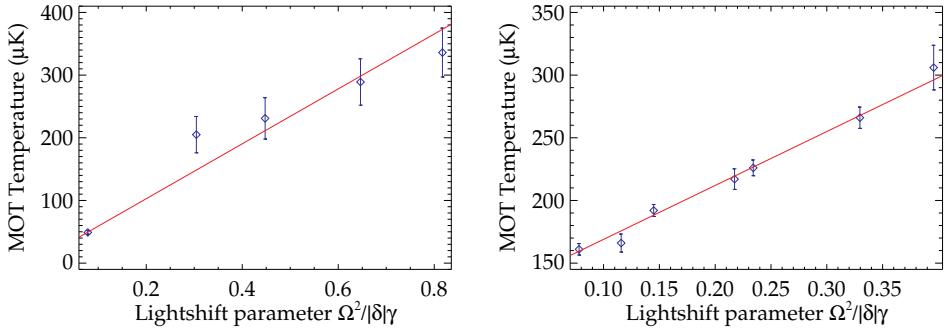

(a) ^{85}Rb (b) ^{87}Rb

Figure 4.28: MOT temperature versus the dimensionless light shift parameter. The line is a fit to Eq. (4.22).

where we have introduced the dimensionless light shift parameter

$$\frac{\Omega^2}{|\delta|\gamma} = \frac{\gamma}{2|\delta|}\frac{I}{I_{\text{sat}}}, \tag{4.23}$$

with Ω the single beam Rabi frequency, δ the detuning and γ the natural linewidth. We measured this dependence by varying the detuning of the trapping laser up to -5γ. Figure 4.28 shows the results for both isotopes. From the fits we find $C_{\sigma^+\sigma^-} = 1.53 \pm 0.13$ and 1.48 ± 0.60 for ^{85}Rb and ^{87}Rb, respectively. Compared to other measurements [128, 130] this is a factor of 3 higher. However, in those works the detuning was generally kept constant and the intensity of the trapping laser was varied. Furthermore the detuning was generally much larger than our maximum detuning of -5γ.

4.10.4 *Loading*

The number of atoms $N(t)$ loaded into a vapour-cell MOT can be described by the following rate equation [131–133]:

$$\frac{\mathrm{d}N(t)}{\mathrm{d}t} = R_{\text{MOT}} - \Gamma_{\text{MOT}}\, N(t) - \beta_{\text{MOT}}\, N(t)^2. \tag{4.24}$$

The loading rate R_{MOT} is determined by the trapping volume of the MOT laser beams V, the density n and temperature T of the Rb vapour [134]:

$$R_{\text{MOT}} = \frac{1}{2}\frac{nV^{2/3}v_c^4}{(2k_{\text{B}}T/m)^{3/2}}. \tag{4.25}$$

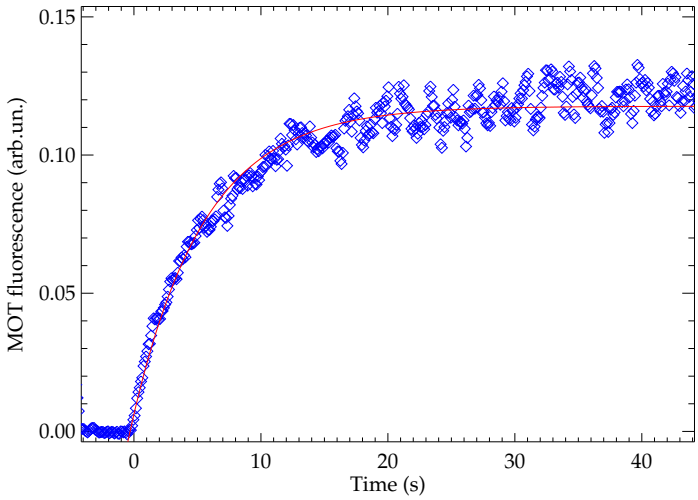

Figure 4.29: Measurement of the loading of an ^{85}Rb MOT. The data is fitted to Eq. (4.27).

Here v_c is the maximum capture speed; only rubidium atoms with a lower speed can be slowed enough to be trapped. It is determined by parameters like the radius of the trapping beams, the light intensity and detuning, etc. The second term on the RHS in Eq. (4.24) describes losses due to hot Rb atoms in the vapour and other background gas collisions. The third term describes losses due to collisions between trapped atoms, e. g. radiative escape or ground-state hyperfine-changing collisions [131, 135–137]. Unlike in the creation of BECs, higher-order loss processes involving three-body collisions are not significant at the comparatively low densities in a MOT. In our regime the density is relatively low, which means two-body losses may therefore also be neglected. Therefore Eq. (4.24) is reduced to

$$\frac{\mathrm{d}N(t)}{\mathrm{d}t} = R_{\mathrm{MOT}} - \Gamma_{\mathrm{MOT}}\, N(t), \tag{4.26}$$

with the solution

$$N(t) = N_{\mathrm{ss}}\big(1 - \exp(-\Gamma_{\mathrm{MOT}}\, t)\big), \tag{4.27}$$

where $N_{\mathrm{ss}} = R_{\mathrm{MOT}}/\Gamma_{\mathrm{MOT}}$ is the steady state number of atoms.

Figure 4.29 shows a typical measurement of the loading of ^{85}Rb MOT. The line is a fit to Eq. (4.27) with a MOT loading time constant of $1/\Gamma_{\mathrm{MOT}} = 5.64 \pm 0.07\,\mathrm{s}$. In our experiments the MOT is loaded for at least 20 s before the FORT beam is turned on.

5

CHARACTERISTICS OF CONTINUOUS AND PULSED FORTS

In this chapter measurements of several aspects of atoms trapped in a FORT are discussed. These include the way atoms are loaded into the optical dipole trap, a study of the loss processes that eject atoms from the trap and a determination of the temperature of the atoms in the trap. A comparison is made between CW and ML FORTs. One might expect differences between these two schemes due to the pulsed nature of the ML light. Many-body losses may, for example, be higher for a ML FORT, because of the larger bandwidth of the light. Apart from this, one would expect the initial number of atoms loaded in the trap to be equal, since the time-averaged potential is the same in both schemes. In 2000 Clarke et al. were the first to make an optical dipole trap (ODT) with ML lasers, using a Ti:Sapphire and a Nd:YVO_4 laser [88]. Recently Shiddiq et al. used a Nd:YAG laser for a more detailed study of the properties of ML FORTs [138]. Both experiments were performed in a rubidium cell.

Unless mentioned otherwise, the experimental parameters chosen in this chapter are as follows. The wavelength of the FORT beam is $\lambda = 810\,\mathrm{nm}$, the time averaged power $P_{\mathrm{Mira}} = 0.14\,\mathrm{W}$ and the beam waist $w_0 = 20\,\mu\mathrm{m}$. This results in a trap depth of $U_0 = 276\,\mu\mathrm{K}$ for ^{85}Rb and $U_0 = 280\,\mu\mathrm{K}$ for ^{87}Rb. The FORT loading time $t_{\mathrm{load}} = 35\,\mathrm{ms}$ and the FORT storage time $t_{\mathrm{storage}} = 40\,\mathrm{ms}$. The probe light is switched on for 1 ms after an expansion time of 1 ms. The detuning of the cycling laser $\delta_{\mathrm{MOT}} = -2\gamma$ during loading of the MOT and it is ramped to -5γ in $t_{\mathrm{ramp}} = 20\,\mathrm{ms}$ while loading the FORT. During the ramp the intensity of the repump laser is also reduced.

5.1 LOADING BEHAVIOUR

Studying the number of atoms in the FORT as a function of experimental parameters is important in order to find out the optimal way to trap as many atoms as possible into the dipole trap. Kuppens et al. have investigated this extensively for a CW FORT and their observations were taken as a starting point for our own experimental settings, summarised above [139, 140].

Figure 5.1 shows a typical timing scheme for a FORT loading measurement.

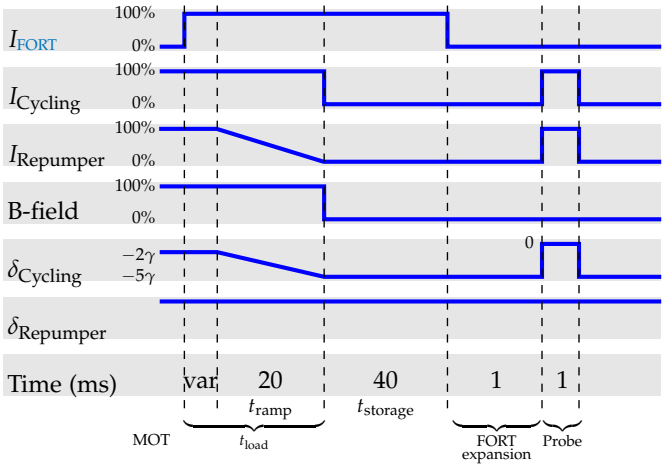

Figure 5.1: Typical timing of a FORT loading measurement. Times are given in ms.

All FORT measurements start with the loading of the MOT (cf. § 4.10). As soon as the number of atoms in the MOT has stabilised, typically after 20 s, the Mira light is turned on. After a variable delay the intensity of the repump laser is ramped down, and at the same time the detuning of the MOT light is ramped as described above. In most other experiments involving FORTs described in literature, the magnetic field is also turned off during this detuning ramp to create a sub-Doppler cooling phase, leading to an increase in the number of atoms trapped in the FORT. However, in our experiments this is not possible because of the imbalance in the self inductions of the coils as mentioned in § 4.2. Despite the presence of the magnetic field the atoms are still cooled because of the optical molasses. Following the ramp, the MOT lasers are switched off and the atoms remain captured in the FORT for $t_{\mathrm{storage}} = 40\,\mathrm{ms}$, after which the Mira beam is switched off and the atoms are allowed to expand for 1 ms before being detected by a 1 ms probe pulse.

5.1.1 *Power dependence*

Figure 5.2 shows the number of atoms trapped in the FORT for different powers of the Mira laser. The diamonds and triangles are for a CW and a ML trap, respectively. One can readily see that there is no statistically significant difference between the number of atoms in a continuous or a pulsed trap. This is not surprising since the atoms cannot follow the light pulses and only sense a time averaged potential depth equal to that of the CW case. Our result is in agreement with the measurements of Clarke et al. [88], but Shiddiq et al. trapped 70 % less atoms in their pulsed FORT, possibly because they did not use a MOT

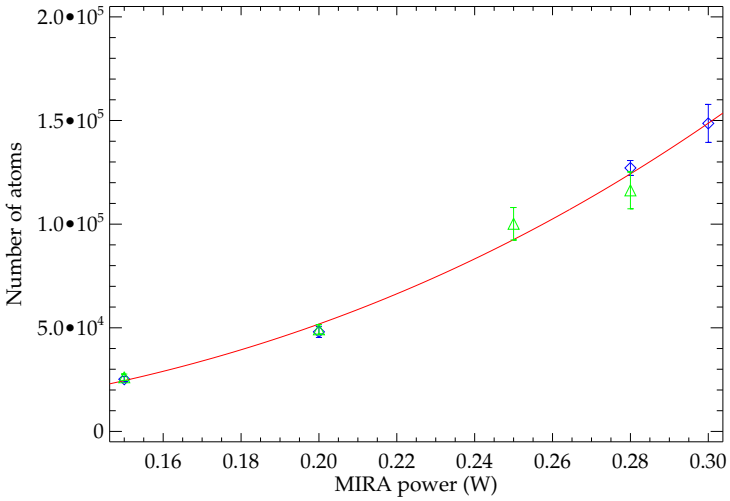

Figure 5.2: The number of ^{85}Rb atoms trapped in a CW (diamonds) and a ML (triangles) FORT versus the power of the trap laser. The line is a fit to $N = aP_{\text{Mira}}^{b}$.

detuning/repump intensity ramp [138]. The line is a fit to $N = aP_{\text{Mira}}^{b}$, with P_{Mira} the Mira power. The resulting values for the fit parameters are $a = (3.4 \pm 0.4) \cdot 10^6$ and $b = 2.6 \pm 0.1$.

To interpret these measurements the following static model has been proposed [141]. Assume that the atom density of the MOT is uniform over the volume of the FORT and equal to the peak density n_0 (cf. § 4.10.2). Also assume that the velocities of the atoms in the MOT are distributed according to a Maxwell-Boltzmann distribution. Then the number of atoms trapped in the FORT can be calculated by assuming that all atoms within the trapping volume that have a kinetic energy smaller than the local potential depth $U_{\text{dip}}(\rho, z)$ cannot escape and become trapped. This defines an effective volume V_{eff} in phase space. Note that this oversimplifies the experiment considerably, since the dynamics induced by the ramps of the MOT detuning and the repump intensity are not taken into account, while we observe clear effects in reality.

To find the number of atoms in the trap we use

$$N = n_0 V_{\text{eff}}, \tag{5.1}$$

where the effective volume is given by

$$V_{\text{eff}} = 2\pi \int_0^\infty \rho \, \mathrm{d}\rho \int_{-\infty}^{\infty} \mathrm{d}z \int_0^{v_{\max}(\rho,z)} f(v) \, \mathrm{d}v, \tag{5.2}$$

with $f(v)\,\mathrm{d}v$ the Maxwell-Boltzmann distribution

$$f(v)\,\mathrm{d}v = 4\pi \frac{v^2}{\pi^{3/2}\,\tilde{v}^3} \exp\!\left(\frac{-mv^2}{2k_\mathrm{B}T}\right)\,\mathrm{d}v, \tag{5.3}$$

in which $\tilde{v} = \sqrt{\frac{2k_\mathrm{B}T}{m}}$ is the most probable speed. The maximum speed an atom can have without escaping the trap is found from $\frac{1}{2}mv_{\max}^2 = U_{\mathrm{dip}}(\rho, z)$:

$$v_{\max}(\rho, z) = \sqrt{\frac{2U_0}{m}}\,\frac{w_0}{w(z)} \exp\!\left(\frac{-\rho^2}{w(z)^2}\right), \tag{5.4}$$

where we have used

$$U_{\mathrm{dip}}(\rho, z) = \frac{-U_0}{w(z)^2} \exp\!\left(\frac{-2\rho^2}{w(z)^2}\right) \tag{5.5}$$

from Eqs. (3.18a) and (3.21). The number of trapped atoms is then given by

$$\begin{aligned} N &= n_0 V_{\mathrm{eff}} \\ &= 2\pi n \int_0^\infty \rho\,\mathrm{d}\rho \int_{-\infty}^{\infty} \mathrm{d}z \int_0^{v_{\max}(\rho,z)} 4\pi \frac{v^2}{\pi^{3/2}\,\tilde{v}^3} \exp\!\left(\frac{-mv^2}{2k_\mathrm{B}T}\right)\,\mathrm{d}v, \end{aligned} \tag{5.6}$$

The integral over $\mathrm{d}v$ can be solved analytically,

$$\int_0^{v_{\max}} f(v)\,\mathrm{d}v = \mathrm{Erf}\left(\frac{v_{\max}}{\tilde{v}}\right) - \frac{2\,v_{\max}}{\sqrt{\pi}\,\tilde{v}} \exp\left(-\frac{v_{\max}^2}{\tilde{v}^2}\right), \tag{5.7}$$

but the remaining part has to be computed numerically. Unfortunately it diverges because $U_{\mathrm{dip}}(\rho, z)$ falls off with $1/z^2$. Therefore, we chose to truncate the volume of integration at $z = z_\mathrm{R}$, the Raleigh range. This is justified since z_R is of the order of the MOT size and no significant number of atoms from the background gas will be captured. The results of this calculation are shown in Fig. 5.3 where the effective volume V_{eff} is plotted as a function of the Mira laser power. The model thus shows that N scales as $P_{\mathrm{Mira}}^{3/2}$ for low powers as indicated by the dashed line and gradually levels off towards $P_{\mathrm{Mira}}^{1/8}$ at high powers (dash-dotted line). Comparing this to our measurements where we have found a $P_{\mathrm{Mira}}^{2.6}$ dependence, we must conclude that this static model does not describe our measurements. Consider, for example, $P_{\mathrm{Mira}} = 0.20\,\mathrm{W}$. The central MOT density is $n_0 = 2 \cdot 10^{16}\,\mathrm{m}^{-3}$ (cf. § 4.10.2 on page 60) and from Fig. 5.3 we find $V_{\mathrm{eff}} = 2.2 \cdot 10^{-12}\,\mathrm{m}^3$ at 0.20 W. Thus the number of trapped atoms is $N = 4.5 \cdot 10^4$, which is close to our measurement. Conversely, at $P_{\mathrm{Mira}} = 0.30\,\mathrm{W}$ we find $V_{\mathrm{eff}} = 4 \cdot 10^{-12}\,\mathrm{m}^3$ giving $N = 8 \cdot 10^4$, almost a factor of two lower than in our measurement.

The discrepancy between the results of this simple model and our measurements may have several reasons. First of all it only considers the geometrical

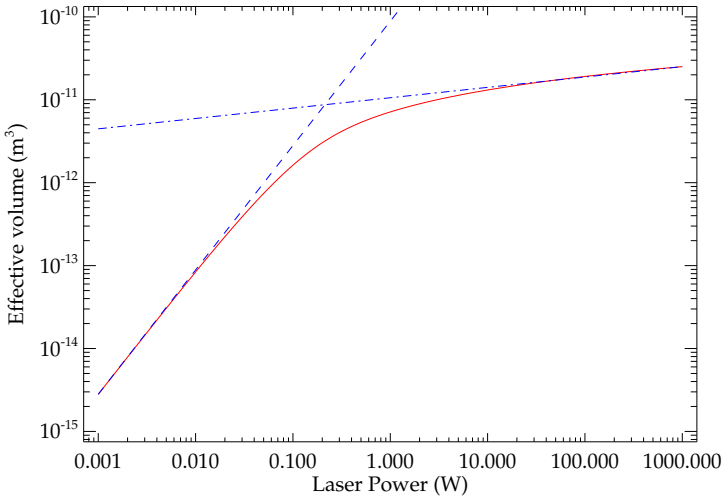

Figure 5.3: Numerical calculation of the effective volume V_{eff} of the FORT, which is proportional to the number of atoms trapped in the FORT, as a function of Mira laser power P_{Mira}. The dashed line indicates $P_{\text{Mira}}^{3/2}$ and the dash-dotted line $P_{\text{Mira}}^{1/8}$.

overlap of the FORT with the MOT; only atoms that are in the trapping volume of the FORT beam are taken into account in the calculation. The complicated dynamics of MOT atoms entering and exiting the FORT region and collisions between the already captured atoms in the FORT are ignored. The same goes for the loading scheme including the ramps of the repump laser intensity and the MOT cycling-laser detuning. Nevertheless, the model does fit the measurements of Wu et al., even though their loading scheme is similar to ours [141].

5.1.2 *Time dependence*

The number of atoms loaded into a dipole trap as a function of time is generally described by an equation similar to the MOT loading equation, Eq. (4.24):

$$\frac{\mathrm{d}N(t)}{\mathrm{d}t} = R_{\text{FORT}}\, \mathrm{e}^{-\gamma_{\text{MOT}} t} - \Gamma_{\text{L}}\, N(t) - \beta'_{\text{L}}\, N(t)^2, \tag{5.8}$$

In accordance with the definition of Kuppens et al. [139] the prime on β'_{L} is used to indicate number dependent losses as compared to density dependent losses and γ_{MOT} is the rate at which the MOT loses atoms due to the repump and detuning ramp.

Figure 5.4 shows typical loading curves for both a CW and a ML FORT. For these measurements $t_{\text{load}} = t_{\text{ramp}}$, i. e. the ramps start at the same time the FORT light is

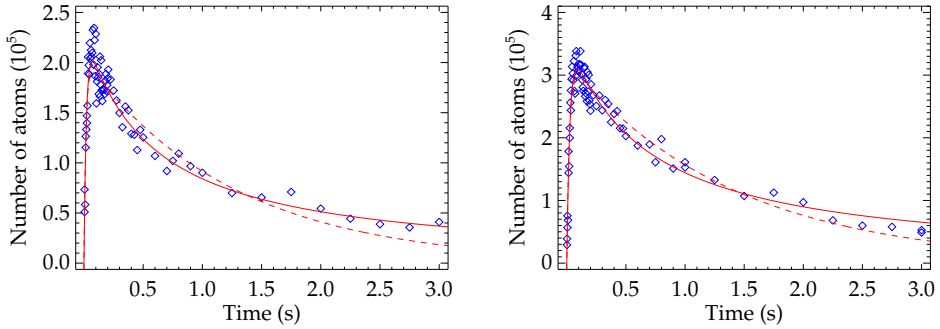

(a) CW (b) ML

Figure 5.4: Loading curves for both CW and ML FORTs with detuning ramp times equal to the FORT loading time. The solid lines are fits to the solution of Eq. (5.9) with the parameters mentioned in the text. The dashed lines are fits to Eq. (5.8) without the two-body loss term. The statistical errors are of the order of the symbol size. The measurements were done with ^{85}Rb at a power of $P_{\text{Mira}} = 0.20\,\text{W}$.

turned on, contrary to the situation in Fig. 5.2 where the FORT light was switched on for 15 ms before the ramps started. In the present scheme the number of atoms loaded into the ML FORT is significantly higher than for the continuous FORT. As mentioned earlier, this is in contrast with the findings of Shiddiq et al., who did not apply ramps but change the MOT detuning instantaneously [138]. Possibly the higher yield observed in the ML FORT loading is caused by cooling of atoms in the FORT by the MOT lasers. This cooling is absent in the CW case because of the light shift. It turns out that the measurements cannot be fit satisfactorily with Eq. (5.8). Therefore, the solid lines in Fig. 5.4 are fits to the solution of Eq. (5.8) without the single-particle loss term. The fit coefficients are listed in Table 5.1. The dashed lines are fits to Eq. (5.8) without the two-body loss term. From the $\bar{\chi}^2$ of the fits we conclude that in these measurements two-particle losses are dominant. Equation (5.8) thus reduces to

$$\frac{\mathrm{d}N(t)}{\mathrm{d}t} = R_{\text{FORT}}\,\mathrm{e}^{-\gamma_{\text{MOT}}t} - \beta'_{\text{L}}\,N(t)^2, \tag{5.9}$$

which has an analytic solution in terms of the modified Bessel functions of the first (I_α) and second kind (K_α) [142, 143]. Accounting for the different FORT volumes, the loading rate R_{FORT} agrees with the values found in literature [138, 139, 144]. Our values for β'_{L} agree with Kuppens et al., but are slightly smaller than those found by Shiddiq et al., Petrov et al..

For ^{87}Rb Dürr et al. have shown that the two-body losses can be reduced by a factor of 15 using an extra laser frequency [145]. However, we did not investigate

	CW FORT	
R_{FORT}	$1.10 \cdot 10^7 \pm 2.7 \cdot 10^4\,\mathrm{s}^{-1}$	$1.21 \cdot 10^7 \pm 3.3 \cdot 10^4\,\mathrm{s}^{-1}$
γ_{MOT}	$49.8 \pm 0.14\,\mathrm{s}^{-1}$	$60.0 \pm 0.18\,\mathrm{s}^{-1}$
Γ_{L}		$0.80 \pm 0.0017\,\mathrm{s}^{-1}$
β'_{L}	$(7.6 \pm 0.020) \cdot 10^{-6}\,\mathrm{s}^{-1}$	
$\tilde{\chi}^2$	547.4	835.6
	ML FORT	
R_{FORT}	$1.35 \cdot 10^7 \pm 2.0 \cdot 10^4\,\mathrm{s}^{-1}$	$1.45 \cdot 10^7 \pm 2.4 \cdot 10^4\,\mathrm{s}^{-1}$
γ_{MOT}	$39.2 \pm 0.072\,\mathrm{s}^{-1}$	$45.7 \pm 0.084\,\mathrm{s}^{-1}$
Γ_{L}		$0.72 \pm 0.0011\,\mathrm{s}^{-1}$
β'_{L}	$(4.2 \pm 0.0075) \cdot 10^{-6}\,\mathrm{s}^{-1}$	
$\tilde{\chi}^2$	932.5	1109

Table 5.1: Fit parameters for the FORT loading fits of Fig. 5.4. The left (right) column lists the parameters for the solid (dashed) lines.

this, since the suppression is expected to be much lower for ^{85}Rb, which is the isotope we mainly use.

5.2 FORT LIFETIME

The 1/e decay time of the number of atoms in the dipole trap during the storage time (i. e. when no MOT light is present) is a second important characteristic of a FORT. Measuring such a lifetime curve entails the following steps, as shown schematically in Fig. 5.5. After loading the MOT for several seconds the FORT beam is turned on. FORT loading typically lasts $t_{\mathrm{load}} = 35\,\mathrm{ms}$ after which the MOT lasers are switched off, allowing the MOT atoms that are not trapped in the FORT to fall away due to gravity. The FORT laser remains switched on for a variable amount of time t_{storage}, after which the remaining FORT atoms are allowed to expand into free space for 1 ms. This stage is followed by a 1 ms probe pulse and the atomic fluorescence is recorded on the CCD. The minimal storage time is 40 ms since for shorter times the falling MOT cloud is still visible.

A general model for trap loss in an optical trap is described by

$$\frac{\mathrm{d}N(t)}{\mathrm{d}t} = -\Gamma_{\mathrm{S}}\,N(t) - \beta'_{\mathrm{S}}\,N^2(t), \tag{5.10}$$

with N the number of atoms trapped in the FORT. The term with Γ_{S} includes the losses due to collisions with untrapped (background gas) atoms and losses due

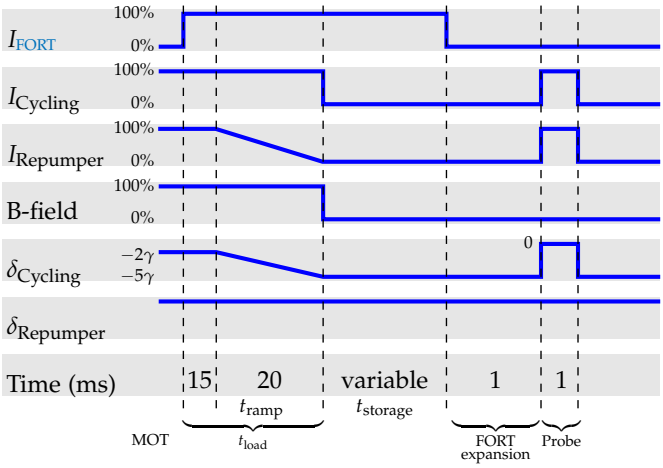

Figure 5.5: Typical timing of a FORT lifetime measurement. Times are given in ms.

to scattering of Mira laser photons. The N^2 term describes the two-body losses caused by e. g. cold collisions between two trapped atoms or photoassociation. The subscript S indicates that the coefficients refer to the storage of atoms in the FORT, which is to distinguish them from the loss terms in the loading equations (Eq. (5.8) and Eq. (5.9)), since they are not necessarily the same because of the absence of MOT light. The solution to Eq. (5.10) is

$$N(t) = \frac{N_0\, \mathrm{e}^{-\Gamma_S t}}{1 + \frac{\beta'_S N_0}{\Gamma_S}(1 - \mathrm{e}^{-\Gamma_S t})}, \tag{5.11}$$

where N_0 is the number of atoms at $t = 0$.

Figure 5.6 shows typical lifetime curves, both for a CW (diamonds) and a ML (triangles) FORT with ^{85}Rb atoms. The solid line is a fit of the CW data to Eq. (5.11). From the fit we find $\Gamma_S = 0.82 \pm 0.03\,\mathrm{s}^{-1}$ and $\beta'_S = (7.7 \pm 0.17) \cdot 10^{-5}\,\mathrm{s}^{-1}$. For the ML data (dashed line) we find $\Gamma_S = 1.3 \pm 0.03\,\mathrm{s}^{-1}$ and $\beta'_S = (6.6 \pm 0.20) \cdot 10^{-5}\,\mathrm{s}^{-1}$. From these numbers it is clear that the differences for the two-body losses between the CW and the ML FORT are small. However, we do find a significant difference in Γ_S. For the CW case the lifetime of $1/\Gamma_S = 1.2\,\mathrm{s}$ is determined by collisions with the background gas. Taking a closer look at the variation of Γ_S versus FORT laser power as shown in Fig. 5.7 we observe no change for a CW FORT. For a ML FORT, however, the single particle scattering rate starts at the same level as in the CW case but it increases for larger powers. This may be due to the increased photon scattering rate and concomitant heating. The scattering becomes larger than the losses due to background gas which dominate at low powers.

The two-body collision rates are equal for both pulsed and continuous FORTs as shown in Fig. 5.8. They are in agreement with the measurements in Refs. [138, 146]

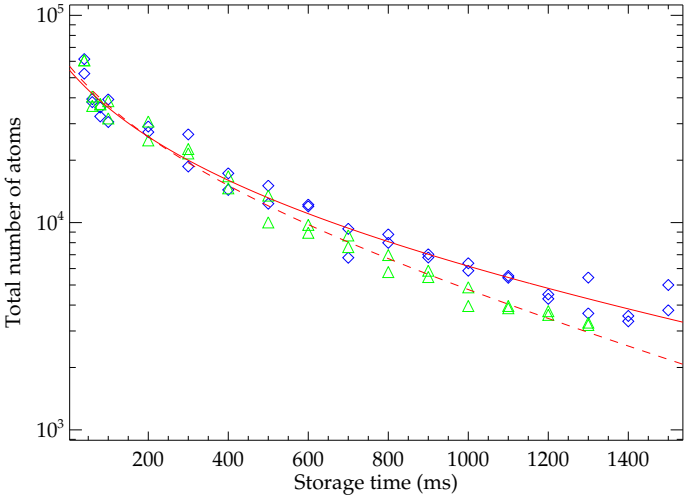

Figure 5.6: Typical lifetime curves for a CW (diamonds, solid line) and a ML (triangles, dashed line) FORT with ^{85}Rb atoms, the statistical error bars are of the order of the symbol size. The lines are fits to Eq. (5.11). For these measurements $P_{\text{Mira}} = 0.20\,\text{W}$.

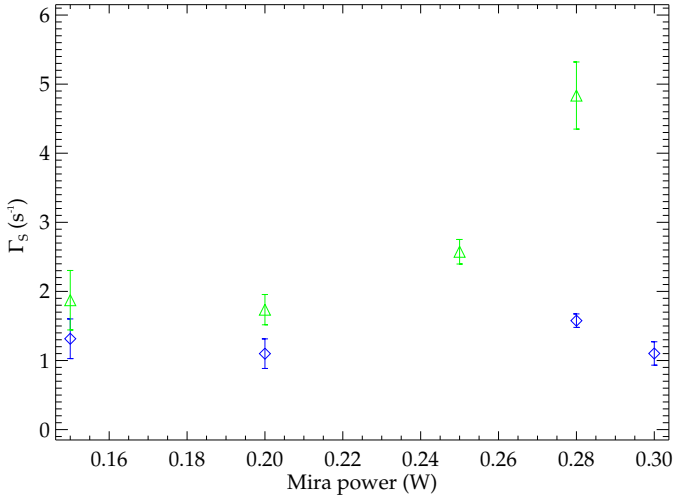

Figure 5.7: The single particle scattering rate Γ_S as a function of FORT laser power for both CW (diamonds) and ML FORTs (triangles).

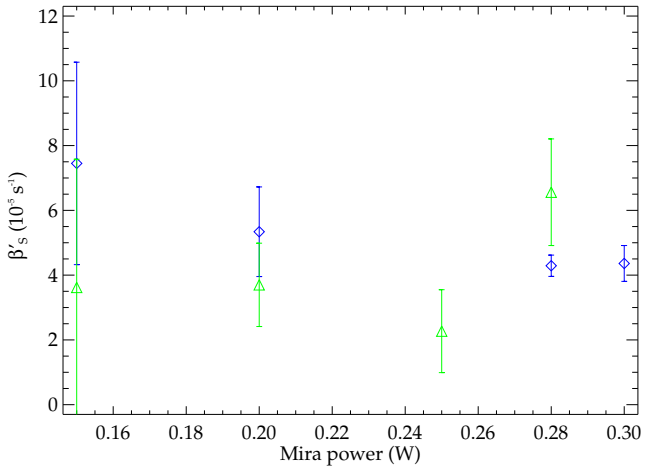

Figure 5.8: The two-body loss rate β'_S as a function of FORT laser power for both CW (diamonds) and ML FORTs (triangles).

and almost an order of magnitude lower than the value of Petrov et al. who found $2.3 \cdot 10^{-4}\,s^{-1}$ for Cs in a CW Yb:YAG trap. For ^{87}Rb we found for $\beta'_S = (8.2 \pm 0.3) \cdot 10^{-4}\,s^{-1}$ and $(7.6 \pm 0.6) \cdot 10^{-4}\,s^{-1}$ for CW and ML, respectively at $P_{Mira} = 0.25\,W$. Just as for ^{85}Rb the difference is no statistical difference between the CW and the ML trap. Some care must be taken when comparing the two-body loss rate across different experiments since FORT volumes may differ and photoassociation is one of the processes contributing to the two-body losses. The wavelength range we are using has a plethora of photoassociation lines, therefore β'_S will vary a lot with the FORT laser wavelength, sometimes almost up to an order of magnitude [146]. This may explain the difference between our value for β'_S and the value of $1.42 \cdot 10^{-6}\,s^{-1}$ found at $\lambda = 784.5\,nm$ [139]. In experiments involving QUESTs photoassociation does not play a role anymore.

5.3 FORT TEMPERATURE

The temperature of atoms trapped in the FORT is measured using ballistic expansion in a similar way as the temperature of atoms in the MOT (cf. § 4.10.3). After loading the FORT the atoms are stored for typically $t_{storage} = 40\,ms$ in order to allow them to equilibrate in the potential of the ODT and remove untrapped atoms from the MOT by gravity. To monitor the ballistic expansion of the cloud, the probe light is switched on for 1 ms after specified times of flight and an image of the fluorescence is recorded by the LN CCD. Figure 5.9 shows a series of images

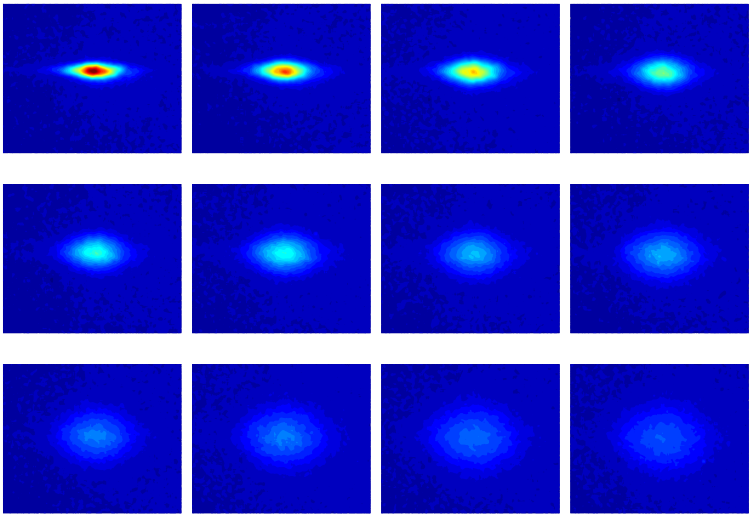

Figure 5.9: Series of images of an expanding ^{85}Rb CW FORT making up a temperature measurement. The images where taken after an expansion time of 1 to 6.5 ms at intervals of 0.5 ms. The images have identical false-colour scales. Figure C.5 on page 112 is a colour print of this figure.

taken in this way. The initial size of the FORT cloud is 0.47×0.10 mm.

The temperature of the atoms is determined by fitting a Gaussian to the images and extracting the radius σ as a function of expansion time in the radial and the axial direction. These widths, plotted versus expansion time, are fitted to Eq. (4.21). Because of the limited size of the probe beams in the horizontal plane the falling cloud can only be monitored for several tens of ms. Since the initial size of the cloud is smallest in the radial direction, the temperature can be determined most accurately by analysing the radial width of the Gaussian. It is in this direction that the expansion is largest compared to the initial size in Eq. (4.21). Figure 5.10 shows temperature measurements in the radial (5.10a) and axial (5.10b) directions. The fitted temperatures are $T_\rho = 81.6 \pm 1.3\,\mu$K and $T_z = 106 \pm 4\,\mu$K for the radial and axial directions respectively. As noted earlier, the influence of the initial size is clearly seen in the axial measurement. The temperature does not depend on t_{ramp}. The fact that the temperatures in both directions differ points to slow thermalisation in the 40 ms storage time. Indeed, the densities in the FORT are relatively low and the axial trap frequency is only a few Hz.

Experiments on the temperature of the FORT atoms vs. the trap depth show a linear dependence with $\eta_\rho = k_{\mathrm{B}} T_\rho / U_0 = 0.28 \pm 0.03$ and $\eta_z = k_{\mathrm{B}} T_z / U_0 = 0.42 \pm 0.05$. A similar dependence with a factor 0.4 is found in literature as

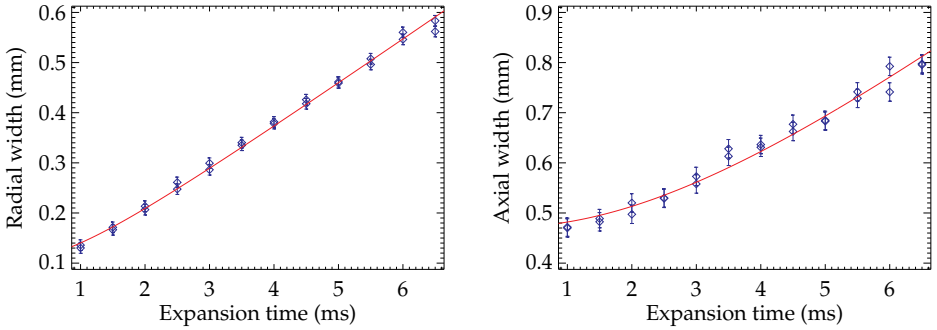

(a) Radial FORT temperature.

(b) Axial FORT temperature.

Figure 5.10: A typical measurement of cloud radius versus expansion time. The lines are a fit to Eq. (4.21) from which a temperature of $81.6 \pm 1.3\,\mu K$ is found for the radial direction and $106 \pm 4\,\mu K$ for the axial direction.

well [139]. For potassium the fraction was found to be 0.2 [147]. The fraction increases for larger MOT detunings. Comparing the temperatures of the MOT and the FORT shows that the atoms in the FORT have a temperature that is a factor of 1.6 higher at $U_0 = 0.90\,mK$. This is due to the fact that the atoms equilibrate in the new potential, in correspondence with the constant η we found.

5.4 CONCLUSIONS

Loading atoms into a pulsed FORT works just as efficiently as in the continuous case. Under the condition that the ramps last the complete FORT loading time, the number of atoms in a ML trap is higher. The number of atoms scales with $P_{\text{Mira}}^{2.6}$, which is higher than expected from a static model. In our setup the loading is mostly limited by two-body collisions, with a loss rate β'_L that is in agreement with other experiments. Losses linear in N do not play a role, except for ML traps at powers above 0.25 W, where photon scattering comes into play.

The lifetime of the trap is 1.2 s for a continuous trap and 0.77 s for pulsed traps, which is in agreement with other experiments. For trap laser powers higher than approximately 0.23 W Γ_S starts to increase for ML FORT due to the increased photon scattering. The two-body loss rate β'_S in the lifetime measurements remains constant as a function of trap laser power.

The temperature of atoms in the FORT is a fixed fraction of the potential depth, $\eta_\rho = T_\rho/U_0 = 0.28 \pm 0.03$ and $\eta_z = T_z/U_0 = 0.42 \pm 0.05$, which is close to the value found in literature. The temperature of the atoms in the FORT is a factor of 1.6 higher than the MOT temperature.

6

PARAMETRIC EXCITATION IN AN OPTICAL DIPOLE TRAP

In § 4.5.2 the phenomenon of parametric heating of the atoms in an optical dipole trap (ODT) due to noise in the Ar^+ pump laser intensity is briefly discussed. In this chapter the effects of parametric excitation due to laser intensity modulation are studied in more detail. Our initial goal was to use parametric heating to find the trap frequency and use that to calculate the beam waist. We were surprised by the rich physics of both heating and cooling that we encountered.

After an introduction, we will first discuss experiments in which the FORT potential depth is modulated. Subsequently a measurement is presented in which the modulation depth is increased to 100 %. Both measurements are complemented by simulations to elucidate the physics involved.

6.1 INTRODUCTION

At the end of the nineties of the previous century Savard et al. and Gehm et al. studied the influence of small fluctuations in trapping laser power on atoms in an ODT [109, 110]. In the theoretical description they approximated the potential of the dipole trap by a harmonic potential and demonstrated how small intensity fluctuations produce sizable parametric heating of the atoms in the trap. This heating may lead to ejection of atoms from the trap and therefore limits the lifetime of the trap to several seconds. More recently a quantum-mechanical calculation of parametric excitation in atom traps has been presented, but in our case quantisation is not necessary, since the number of bound states in our trap is large [148]. Resonances in trap loss due to parametric heating have been observed both in ODTs and in optical lattices [141, 146, 147, 149–152]. Parametric resonance has also been studied in a MOT and in an optical tweezers trap [153, 154].

In a harmonic trap parametric resonances occur at modulation frequencies which are close to twice the vibrational frequency f_v of atoms in the trap, $f = 2f_v$, and, with smaller amplification factors, at subharmonics at

$$f_n = 2f_v/n \tag{6.1}$$

with n integer valued, because at these frequencies the atomic motion and the

parametric excitation become phase locked [155, 156]. At these frequencies the atoms gain energy with an exponential increase in time resulting in rapid ejection from the trap. This is in contrast with normal resonance where the amplitude increases linearly in time. In the harmonic approximation the dipole potential Eq. (3.18a) reduces to

$$U_{\mathrm{dip}}(\rho, z) = -U_0 \left(\frac{2\rho^2}{w_0^2} + \frac{z^2}{z_{\mathrm{R}}^2} \right) \tag{6.2}$$

for small ρ and z. This is the potential of a harmonic trap with radial and axial trap frequencies $f_{\rho,z}$:

$$f_\rho = \frac{1}{2\pi} \sqrt{\frac{4U_0}{m\, w_0^2}}, \tag{6.3a}$$

$$f_z = \frac{1}{2\pi} \sqrt{\frac{2U_0}{m\, z_{\mathrm{R}}^2}}. \tag{6.3b}$$

In our experiments the radial frequency is typically in the order of several kHz and the axial frequency is in the order of several tens of Hz (cf. table 3.1). In the following we will focus on resonances in the radial direction, which is the direction in which we want to measure the beam waist.

Since in our experiments the trap depth is generally of the same order as the temperature of the atoms, the harmonic approximation fails. Consequently, atoms will not oscillate with one single frequency, leading to a broadening of the resonance. The calculated frequency f_{anh} with which a particle with energy U in a Gaussian potential with depth U_0 oscillates is displayed in Fig. 6.1 and clearly tracks

$$f_{\mathrm{anh}} = f_{\mathrm{h}} \left(1 - \frac{U}{U_0} \right)^{1/e}, \tag{6.4}$$

with f_{h} the frequency of the harmonic trap with the same waist (Eqs. 6.3). The calculation is done for a beam waist $w_0 = 20\,\mu\mathrm{m}$ and a trap depth $U_0 = 300\,\mu\mathrm{K}$, which are typical values for our experiments. In the harmonic approximation $f_\rho = 2.73\,\mathrm{kHz}$. The figure shows that atoms at the bottom of the trap indeed oscillate at this frequency. However, atoms with higher energies sample higher parts of the potential and oscillate with a reduced frequency.

The experiments discussed in this chapter are carried out with ^{85}Rb at $\lambda = 810\,\mathrm{nm}$. The FORT was loaded as described in the previous chapters with $t_{\mathrm{ramp}} = 125\,\mathrm{ms}$ and $t_{\mathrm{storage}} = 75\,\mathrm{ms}$. The FORT load time t_{load} is identical to t_{ramp}. After the storage time the Mira is turned off and the atoms are allowed to expand for 1 ms followed by a detection pulse of 1 ms. During the time the FORT light is on ($t_{\mathrm{load}} + t_{\mathrm{storage}}$) a modulation is applied to the amplitude input of the AOM that

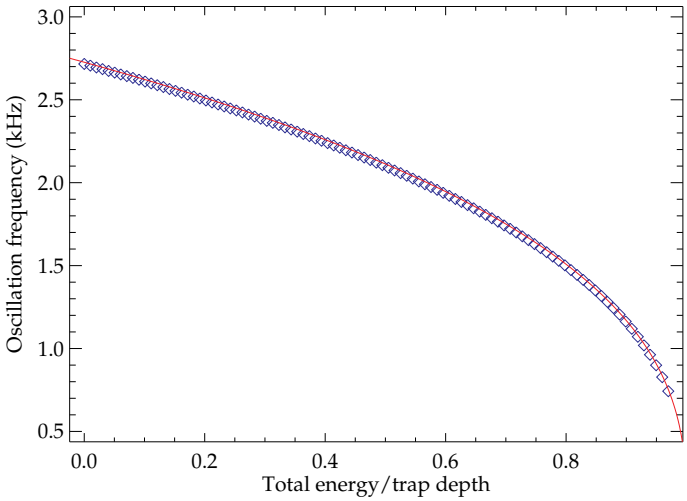

Figure 6.1: Numerically calculated oscillation frequency of an atom in an anharmonic Gaussian-shaped trap with $U_0 = 300\,\mu K$ and $w_0 = 20\,\mu m$ as a function of relative energy. For a harmonic trap with these parameters $f_h = 2.73\,kHz$. The solid line is Eq. (6.4).

controls the Mira light (cf. Fig. 4.14). The switch time of the AOM is of the order of several hundred ns, which is fast enough for our experiments.

6.2 SMALL MODULATION DEPTHS

6.2.1 *Experiments*

A 25 % sinusoidal modulation is applied to the AOM in the FORT beam leading to an intensity modulation of the light and thus a modulation of the trap depth. Figure 6.2 shows a typical measurement of the number of atoms as a function of the modulation frequency for a CW trap and a ML trap, respectively. The lines are fits to a Lorentzian. From the fits the measured resonance frequency f_0 is found to be $f_0 = 6.0 \pm 0.2\,\mathrm{kHz}$ and $f_0 = 6.3 \pm 0.3\,\mathrm{kHz}$ for CW and ML, respectively. The respective linewidths of $6.2 \pm 1.3\,\mathrm{kHz}$ and $11 \pm 3\,\mathrm{kHz}$ are quite broad signifying the large anharmonicity of the Gaussian potential trap.

Rewriting Eq. (6.3a) using Eq. (3.18a), Eq. (3.21) and Eq. (3.22) results in the following expression for the beam waist of a harmonic trap, in terms of the axial harmonic resonance frequency f_ρ:

$$w_0 = \left(\frac{P_{\mathrm{Mira}}}{m\,\pi^2 f_\rho^2} \, \frac{c^2 \gamma}{\omega_0^3} \, \left(\frac{2}{\delta_2} + \frac{1}{\delta_1} \right) \right)^{1/4}. \tag{6.5}$$

For a Gaussian anharmonic trap, however, the parametric resonance occurs at

$$f_0 = 2\langle f_{\mathrm{anh}} \rangle \approx 1.46 f_\rho \tag{6.6}$$

Using this equation we find that the harmonic frequency corresponding to our measured $f_0 = 6.0\,\mathrm{kHz}$ is $f_\rho = 4.1\,\mathrm{kHz}$ for the CW measurement. Inserting this value into Eq. (6.5) results in $w_0 = 16.8 \pm 0.2\,\mu\mathrm{m}$ for CW and $w_0 = 16.4 \pm 0.3\,\mu\mathrm{m}$ for ML. These values are slightly lower than the values found using the other methods mentioned in § 4.5.4.

Quite strikingly the analysis of the measurements reveals that the size of the cloud varies as a function of the modulation frequency. Figure 6.3 shows a parametric excitation measurement similar to the previous one, but with a modulation depth of 33 %. The upper figure shows the number of trapped atoms, the lower two the radial and axial width of the FORT vs. frequency. Since the width of the cloud is directly related to its temperature (cf. sections 5.3 and 4.10.3), the dispersive shape shows that regions of cooling and regions of heating exist near the parametric resonance. This can naturally be explained by the anharmonicity of the trap. As shown in Fig. 6.1 the most energetic atoms in the trap oscillate at low frequencies. Consequently, tuning well below $2f_\rho$ results in the selective heating of hot atoms, their subsequent ejection from the trap, and a decrease of the mean energy of the trapped atoms. Conversely, the mean energy of the atoms in the trap increases when tuning closer to $2f_\rho$ because it leads to heating of cold atoms at the bottom of the trap. The line in the upper figure is a Lorentzian fit with a resonance frequency $f_0 = 8.5 \pm 0.2\,\mathrm{kHz}$. The lines in the lower two figures

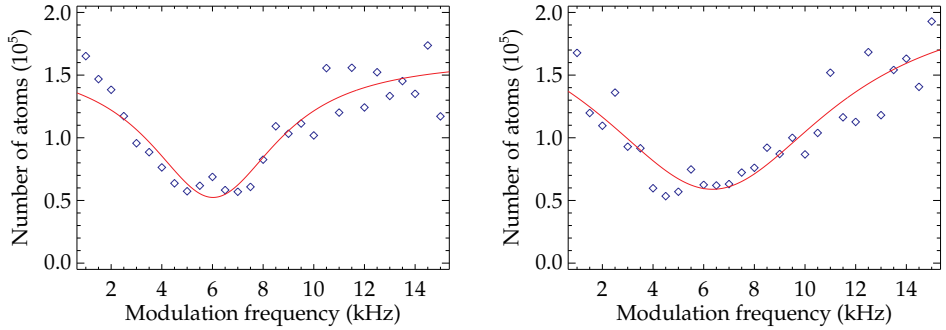

Figure 6.2: Measurement of the trap loss due to parametric excitation for a CW (a) and a ML (b) FORT with ^{85}Rb atoms. The lines are fits to a Lorentzian. Experimental parameters are: $P_{\text{Mira}} = 0.17\,\text{W}$, 25 % intensity modulation.

are fits to the derivative of a Lorentzian, with respective resonance frequencies at $9.4 \pm 0.1\,\text{kHz}$ and $9.7 \pm 0.2\,\text{kHz}$. We see that the resonance in the width profiles is located at a slightly higher frequency than the parametric resonance. We also have observed that the amplitude of the cooling-heating curve is larger for increasing modulation depths. Furthermore, the shape becomes asymmetric, the cooling dip becomes smaller compared to the heating peak. Figure 6.4a illustrates this for the situation of the CW trap in Fig. 6.2a where the modulation depth was 25 %. The symmetric dispersion curve clearly does not fit the data. The dispersive shape of the temperature curve has also been observed in experiments where atoms in a magnetic trap are parametrically excited by shaking the trap [157].

6.2.2 *Simulations*

In order to gain more insight into the underlying mechanisms of parametric excitation in an anharmonic trap, a 1D simulation has been carved out. In this simulation the position and velocity of 10 000 atoms in a Gaussian-shaped trap are monitored as the trap depth is modulated. The initial velocities are distributed randomly according to a Maxwell-Boltzmann distribution corresponding to the measured FORT temperature; the initial positions are distributed randomly in the trap according to the Boltzmann factor. The modulation of the trap is applied for typically 5 ms during which the equations of motion of the atoms in the trap are integrated numerically using a fourth-order Runge-Kutta method. Collisions are not included in the simulation. We have checked that following the atoms for more than 5 ms does not lead to different results. This is expected because as

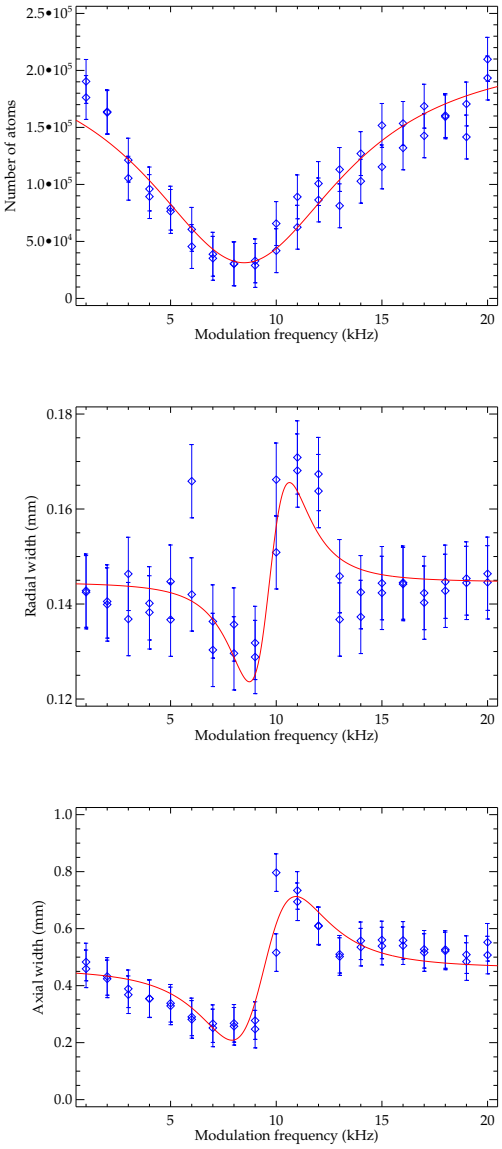

Figure 6.3: Measurement of the parametric excitation of a ^{85}Rb CW FORT. The top figure shows the number of atoms captured in the trap, the line is a fit to a Lorentzian. The two lower figures show the radial and axial widths of the cloud after 1 ms of expansion time. The widths are directly proportional to the temperature of the cloud. The lines are fits to the derivative of a Lorentzian. The experimental parameters are: $P_{\text{Mira}} = 0.24\,\text{W}$, 33 % intensity modulation.

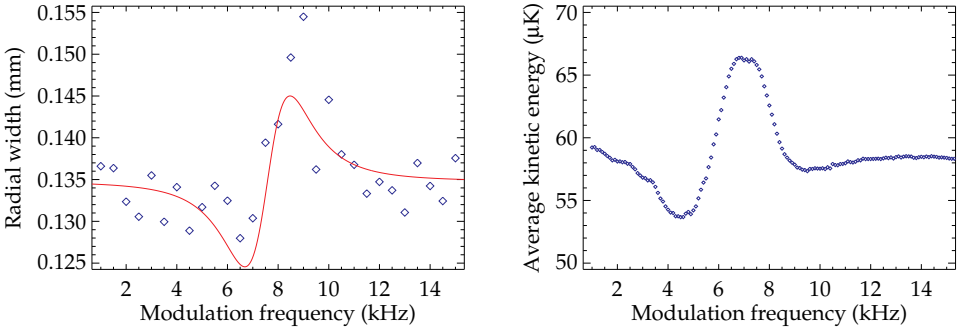

Figure 6.4: (a) Measured width of the CW FORT cloud as a function of modulation frequency corresponding to the trap-loss measurement of Fig. 6.2a. (b) Corresponding result of the simulation discussed in § 6.2.2, showing the average kinetic energy per trapped atom vs. the modulation frequency.

soon as a certain energy class has been depleted it will never be replenished. The initial and final positions and energies, as well as the number of trapped atoms are counted for each run.

Figure 6.5 shows the results of the simulation for the situation corresponding to Fig. 6.3. Figure 6.5a shows the number of trapped atoms vs. modulation frequency. In order to get the simulated resonance at the same position as the measured f_0 at 8.5 kHz, the beam waist needs to be adjusted to 16 µm, somewhat smaller than the value found earlier. For $P_{\text{Mira}} = 0.24\,\text{W}$ this waist corresponds to $U_0 = 738\,\mu\text{K}$. For the temperature of the atoms in the FORT $T = 221\,\mu\text{K}$ is chosen, because $\eta = 0.3$ as discussed in § 5.3. Figure 6.5b shows the average kinetic energy in µK of an atom trapped in the FORT after the modulation. This is equivalent to the temperature since we derive the temperature of the atoms in the trap from their kinetic energy by measuring the expansion of the width of the cloud. From the figure one clearly sees that the simulation reproduces many of the characteristics observed in the measurements. Firstly, the kinetic energy in Fig. 6.5b reproduces the measured dispersive shape. Secondly, the centre of the dispersion curve is at a slightly higher frequency than f_0, but still below $2f_\rho$. Furthermore, the simulation shown in Fig. 6.4b show that the amplitude of the dispersive curve goes down for lower modulation depths in conformity with the experiments. From the simulations it appears that the asymmetry is not due to the lower modulation depth, but due to a lower η. As stated earlier, parametric excitation leads to an exponential energy gain for a class of atoms having a certain energy in the trap. This implies that parametric cooling due to the anharmonicity of the trap also goes exponentially, but at a slower rate for

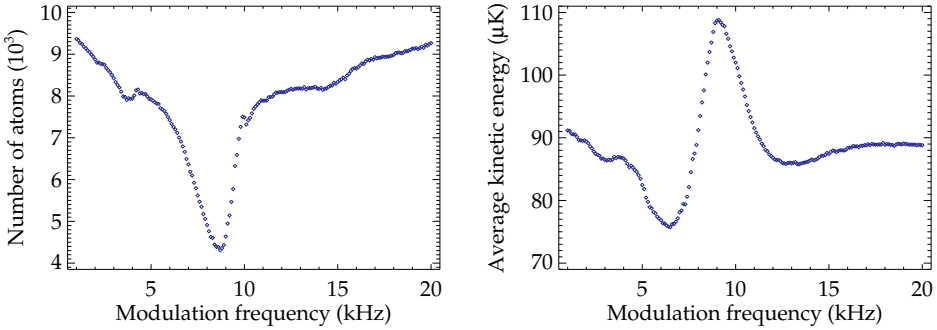

(a) (b)

Figure 6.5: Results of the simulation of atoms in a parametrically excited FORT with a modulation depth of 33 %. The parameters are chosen such that the results correspond to the measured data of Fig. 6.3 (see text). Figure (a) shows the number of atoms as a function of the modulation frequency f and Fig. (b) shows the average kinetic energy of an atom after the modulation.

colder atoms. The main feature the simulations do not reproduce is the width of the trap-loss resonance, which is smaller than the measured one. There is some speculation in the literature that this is due to a slight ellipticity of the beam cross-section [152]. An other reason for the broadening could be anharmonic mixing of the radial and axial frequencies which is not taken into account in the simulation. Finally, the assumption of thermal equilibrium may not be true in a real trap.

With the results of the simulation a series of phase space plots at different frequencies can been made, as shown in Fig. 6.6. The plots show how the heating rate increases as the modulation frequency goes towards resonance at $f_0 = 8.5\,\mathrm{kHz}$. Furthermore, we observe that both cooling and heating take place for atoms depending on the phase of their motion with respect to the driving field. Even near f_0 where virtually all atoms are heated, atoms near the bottom of the trap are still cooled.

In literature another explanation for the dispersive shape of the temperature curve has been proposed [158]. This explanation assumes that a velocity class is selectively removed from the Maxwell-Boltzmann distribution. If the resulting hole in the distribution is tuned below the original mean velocity the sample becomes hotter and *vice versa*. However, our simulations clearly show that parametric driving of the trap truly involves direct cooling and heating without involving collisions and formation of a thermalised gas.

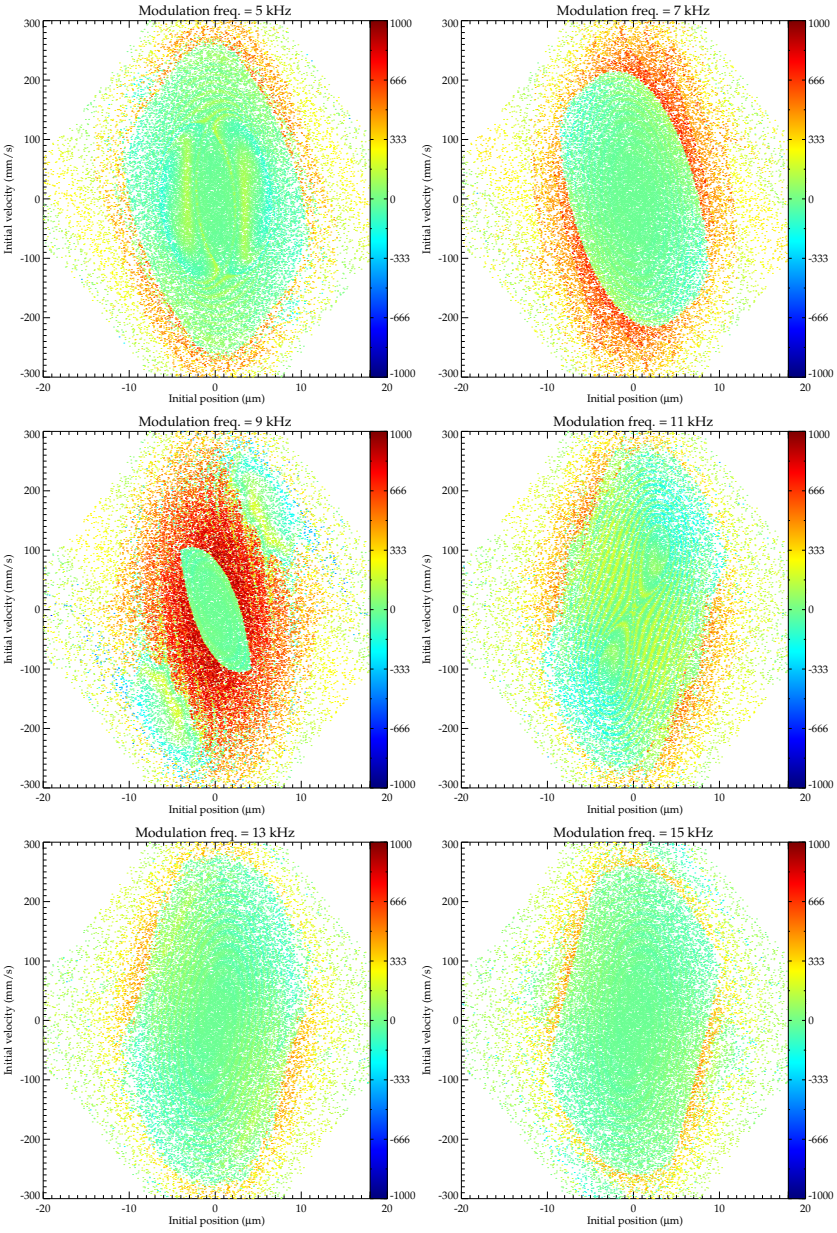

Figure 6.6: Phase space plots of the atoms in a FORT whose depth is modulated at different frequencies as indicated above the individual plots. All images have the same colour scale that indicates the heating rate in μK/s. Figure C.6 on page 113 is a colour print of this figure.

6.3 FULL MODULATION DEPTH

6.3.1 *Experiment*

At this point we investigate the low-frequency regime of a truly pulsed trap. To this end the FORT beam intensity is modulated by applying a 100 % square-wave modulation to the FORT beam, switching the trap on and off at a specific frequency. In such an experiment we expect the modulated trap to be velocity selective and thus temperature selective. Fast atoms escape the trap region before the trap has been turned on. However, atoms with a speed that corresponds to the diameter of the trap divided by half the modulation period (the time the trap is off) are expected to remain trapped, since their arrival time at the edge of the trap region coincides with the turning on of the trap. Consider the following crude model. For atoms with a temperature T the most probable speed is

$$\tilde{v} = \sqrt{\frac{2k_B T}{m}}. \tag{6.7}$$

With that speed an atom remains captured if

$$\frac{1}{2}\Delta t = \frac{2w_0}{\tilde{v}}, \tag{6.8}$$

with $\Delta t = 1/f$ the period of modulation. For a MOT with $T = 130\,\mu\text{K}$ (cf. § 4.10.3) and a FORT beam waist of $w_0 = 16\,\mu\text{m}$ this corresponds to a modulation frequency of 5.0 kHz. At lower frequencies one would expect hardly any atoms to be trapped and at higher frequencies the number of atoms is expected to increase until the maximum number of atoms is reached at a frequency that the atoms can no longer follow, as in the parametric excitation experiments. Moreover, atoms with speeds compatible with subharmonics of the modulation frequency will be captured as well since

$$2w_0 = \tilde{v}\frac{\Delta t}{2} = \text{constant}, \tag{6.9}$$

and therefore

$$2w_0 = \frac{\tilde{v}}{n}\frac{n\Delta t}{2} \tag{6.10}$$

$$= \frac{\tilde{v}}{n}\frac{1}{f_n}, \tag{6.11}$$

with f_n the frequency of the n^{th} subharmonic (cf. Eq. (6.1)).

Figure 6.7 shows the measured number of atoms trapped in the FORT as a function of modulation frequency. One clearly sees that the increase in the number of trapped atoms occurs at a frequency that is four times higher than

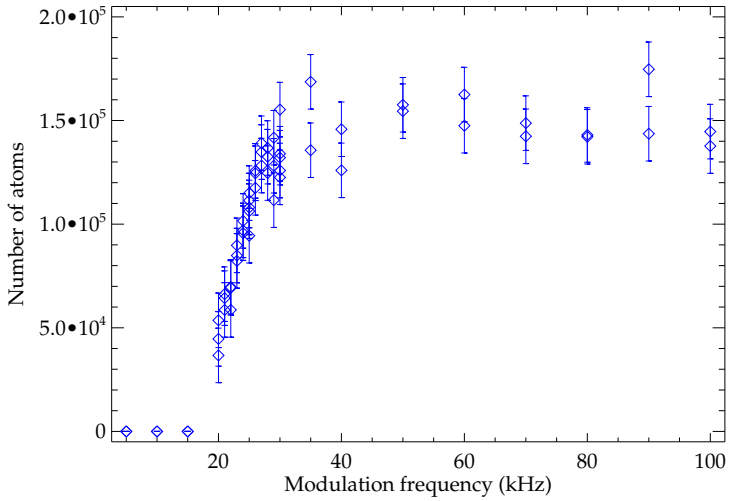

Figure 6.7: Measurement of the number of atoms vs. modulation frequency for full modulation. Below 20 kHz no trapped atoms are detected. The experimental parameters are as mentioned in the previous section, except $P_{\text{Mira}} = 0.28\,\text{W}$.

expected from the simple model. For modulation frequencies below 20 kHz no trapped atoms are detected. For this trap $f_\rho = 5.8\,\text{kHz}$. Apparently the 100 % modulation in an anharmonic trap gives rise to a completely new type of dynamics, which will be discussed in the following section. To check our hypothesis of the velocity selection we measured the temperature of the atoms in the trap. For high modulation frequencies we find $T = 80 \pm 1\,\mu\text{K}$, which is equal to the temperature without modulation of the potential. At 30 kHz the temperature starts to decrease, reaching $66 \pm 1\,\mu\text{K}$ at a modulation frequency of 25 kHz. For lower frequencies the number of atoms was too low for reliable temperature measurements. Although we measured lower temperatures for lower frequencies we feel this is inconclusive evidence for our hypothesis.

6.3.2 *Simulations*

Using the simulation we have also simulated atoms in a fully modulated trap. In Fig. 6.8 the number of trapped particles is shown as a function of the modulation frequency. The input parameters are chosen in conformity with the experimental parameters: $T_{\text{MOT}} = 130\,\mu\text{K}$, $w_0 = 16\,\mu\text{m}$ and $U_0 = 861\,\mu\text{K}$. Comparing the simulation with the experiment one notices that the frequency at which the number of atoms starts to increase is clearly lower than the one observed in the

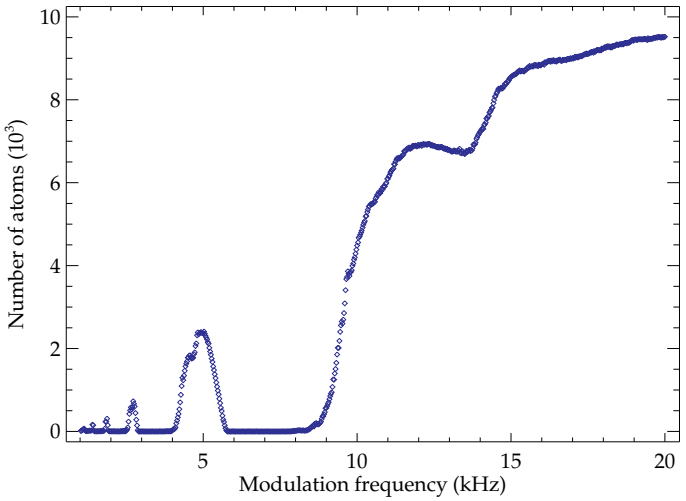

Figure 6.8: Simulation of the number of particles trapped in a FORT as a function of modulation frequency for a 100 % trap depth modulation. $T = 130\,\mu K$, $w_0 = 16\,\mu m$, and $U_0 = 861\,\mu K$.

experiment. However, the simulation shows a peak at 5.0 kHz, exactly as expected by our simple calculation. Furthermore, the simulation shows the subharmonics we expected as well. The narrow width of these peaks stems from the fact that the speed of the atom needs to be very close to the matching frequency, if the speed is slightly higher than the one compatible with the width, the atom will not be trapped. If the speed is slightly lower, the atom will still be trapped, because the potential is still on when it arrives at the edge of the potential. Decreasing the temperature of the atoms in the simulation leads to a increase in the peak heights since the spread in velocities also decreases.

In order to move the capture frequency towards the observed 20 kHz, the potential depth must be lowered to 1.5 mK and the waist must be set to 10 µm in the simulations. These differences are so large that they cannot be attributed to experimental error. This discrepancy may be due to heating effects in the AOM. At low modulation frequencies the AOM has time to heat up and cool down. This may lead to a change in the intensity of the Mira beam which, in turn, can lead to parametric excitation as described earlier. The effect is most pronounced at low modulation frequencies. At higher frequencies the temperature fluctuations in the AOM become less and less severe because there is less time available to cool down and the average temperature will converge to the steady state temperature.

The phase space plots at different frequencies are shown in Fig. 6.9. Comparing the plots with Fig. 6.8 we see that at low frequencies many of the atoms are

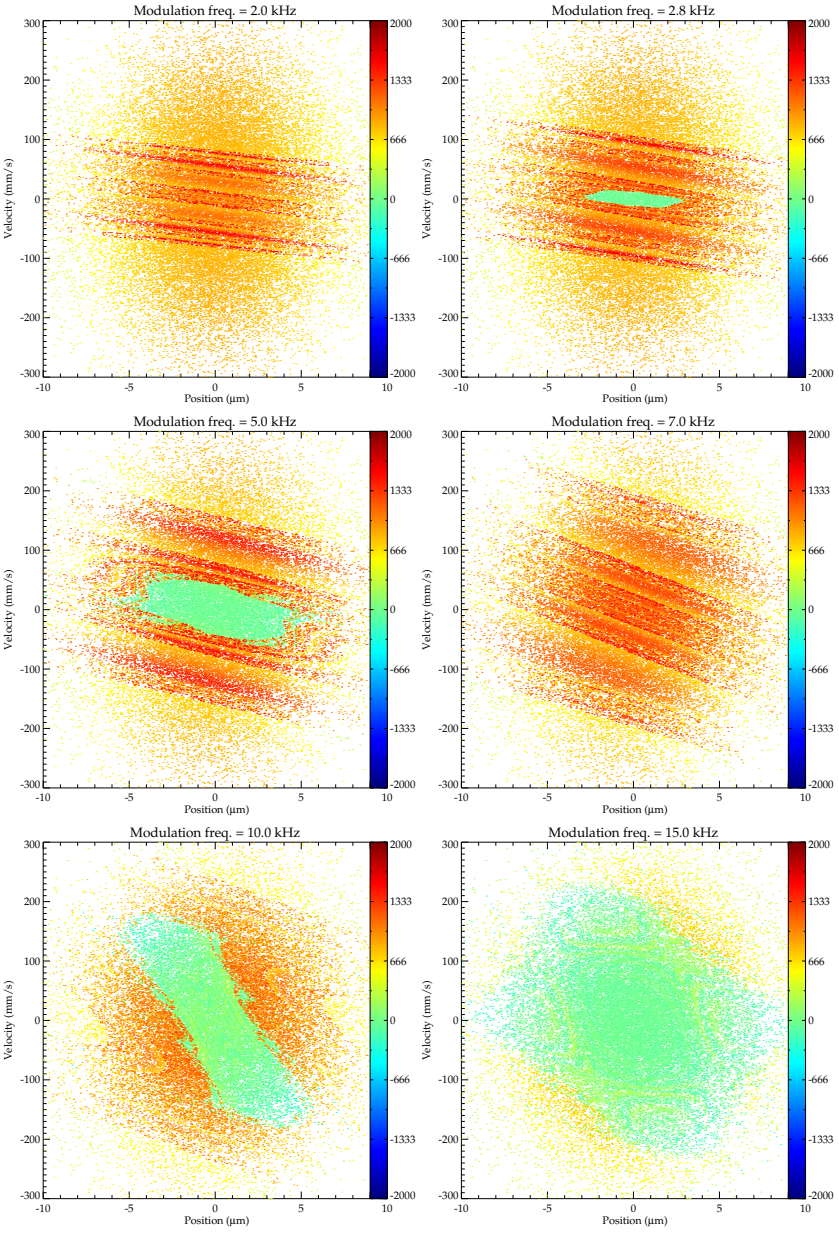

Figure 6.9: Phase space plots of the atoms in a FORT whose depth is modulated at different frequencies as indicated above the individual plots. All images have the same colour scale that indicates the heating rate in μK/s. Figure C.7 on page 114 is a colour print of this figure.

actually heated. For higher modulation frequencies the number of atoms that get heated goes down as well as the heating rate itself. At approximately 15 kHz the majority of the atoms are slightly cooled. This is the region where most of the atoms are captured in the trap. Note that at 2.8 kHz low-velocity atoms near the centre of the trap are cooled and trapped while the other atoms all are heated. This gives rise to the small subharmonic peak at that frequency.

6.4 CONCLUSIONS

Parametric excitation of particles in a harmonic potential occurs at frequencies that are twice the radial and axial trap frequency f_ρ and f_z, respectively. This can be induced by applying a small modulation to the potential depth, for example. In reality, the FORT is highly anharmonic. Both measurements and simulations of trap loss in a FORT have been done. From the observed parametric resonance in an anharmonic trap the beam waist is derived, which is slightly lower than in our earlier measurements (cf. § 4.5.4).

Measuring the temperature of the atoms as a function of the parametric modulation frequency shows a dispersive curve with its centre between f_0 and $2f_\rho$. This is reproduced by the simulations as well, as is the dependency of the amplitude of the curve on the modulation depth. The simulation also shows that the asymmetry between the dip and the peak of the dispersion curve is the result of a low η. This asymmetry is caused by the fact that parametric driving leads to direct cooling and heating depending on the frequency. At lower η the exponential cooling effect is smaller. The simulation does not reproduce the observed width of the resonance. The increase in width may be caused by anharmonic mixing of the radial and axial degrees of freedom, which is not taken into account in the simulation, or a non-thermal velocity distribution in the trap.

From the phase space plots we find that cooling and heating occur at every modulation frequency. Only the number of atoms that has a specific heating or cooling rate varies, as does the magnitude of the rate. Furthermore the plots illustrate nicely that atoms with high kinetic energy are heated at red-detuned frequencies.

To investigate low-frequency pulsed traps the number of atoms in a FORT with 100 % trap depth modulation as a function of modulation frequency is measured. We find that atoms remain trapped starting at a frequency of 20 kHz, although our simple model predicts this to happen at frequencies of approximately 5.0 kHz. Our simulations confirm that frequency and otherwise describe our results well. The discrepancy between the observed and measured frequency is attributed to heating effects in the AOM that is used to modulate the Mira beam.

7

TRAPPING ATOMS WITH ELLIPTICALLY POLARISED LIGHT

All measurements discussed in the previous chapters are performed with linearly polarised FORT light. However, it is possible to trap atoms in a FORT made with circularly polarised light as well, and create a so-called circular FORT (CFORT) [86, 140, 159]. CFORTs can be used to store spin polarised neutral atoms, for example. Generally magnetic traps are used for this task, but those require large magnetic fields which are inherently difficult to control rapidly, are expensive because of the large power supplies involved, and need extensive cooling to prevent the setup from heating up. More importantly, magnetic traps offer relatively weak spring constants. On the other hand, ODTs provide strong confinement and can be controlled easily using AOMs, as shown in this thesis. Finally, the different Zeeman levels have different trap depths in a CFORT, which allows for Sisyphus cooling [159].

In this chapter CW and ML CFORTs created at different wavelengths will be compared.

7.1 THEORETICAL BACKGROUND

The FORT potential U_{dip} and the scattering rate Γ_{sc} depend on the polarisation of the trapping light and on the Zeeman state of the atom, as shown in Eqs. (3.18). For linearly polarised light ($\mathcal{P} = 0$) all m_F-states are degenerate and therefore experience the same potential depth. This degeneracy is lifted for light with $\mathcal{P} \neq 0$. Figure 7.1 shows the FORT potential depths for the $m_F = -3, \ldots, 3$ levels of the ^{85}Rb $F = 3$ ground state for a σ^+-polarised FORT beam ($\mathcal{P} = 1$). Note that the $m_F = 3$ potential is the deepest in between the D_1 and D_2 lines. Furthermore, optical pumping with σ^+ light rapidly transfers atoms to this state. At the red side of the D_1 line the state has the shallowest potential, since there is no $m_F = 4$ level in the $^2P_{1/2}$ state. Since $\Delta m_F = 1$ for σ^+ light (cf. Fig. B.2), this is a dark state.

Equations 3.18 are valid for FORT laser detunings where hyperfine structure splitting of excited states is not resolved: $|\delta| \gg \Delta\omega_{\mathrm{HFS}'}$, with the prime indicating

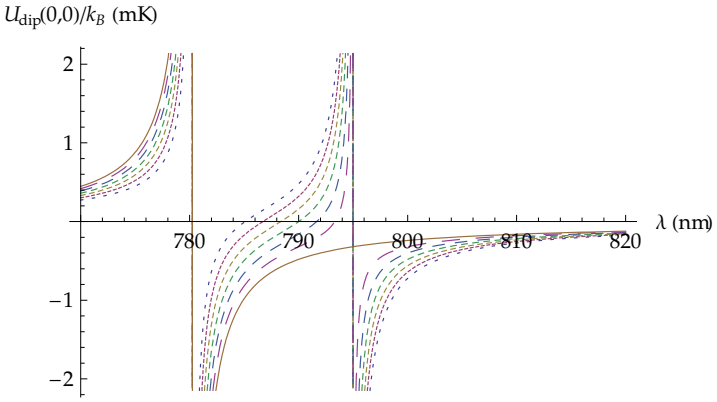

Figure 7.1: CFORT potential depth for the ^{85}Rb $F = 3$ ground states $m_F = 3$ (solid line) to $m_F = -3$ (dotted) for σ^+-polarised light as a function of FORT wavelength as given by Eq. (3.18a). $P_{\text{Mira}} = 0.11\,\text{W}, w_0 = 20\,\mu\text{m}$.

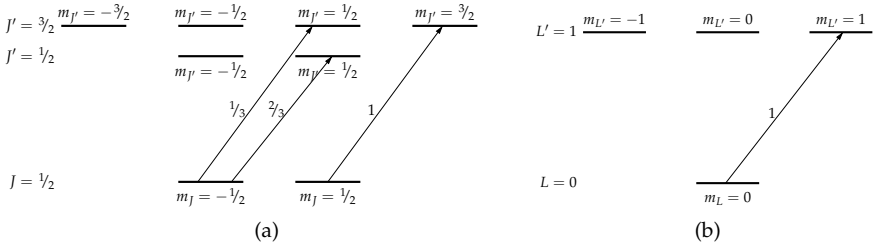

Figure 7.2: Level schemes representing an atom in a CFORT with σ^+ polarisation for $\Delta\omega_{\text{FS}'} \gtrsim |\delta| \gg \Delta\omega_{\text{HFS}}, \Delta\omega_{\text{HFS}'}$ (a) and $|\delta| \gg \Delta\omega_{\text{FS}'}$ (b). The numbers next to the transitions indicate their relative strengths.

the excited state. If the detuning is increased such that the ground-state hyperfine splitting is no longer resolved ($\Delta\omega_{\text{FS}'} \gtrsim |\delta| \gg \Delta\omega_{\text{HFS}}, \Delta\omega_{\text{HFS}'}$), the system can be described as a $J = 1/2 \to J' = 1/2, 3/2$ transition (cf. Fig. 7.2a). For such a transition the dipole trap potential and the scattering rate are given by Eqs. 3.18, with m_F replaced by m_J and g_F by g_J, which is 2 for the ground state of alkali atoms.

If the detuning is increased even further so that the detuning is larger than the fine structure splitting of 15 nm ($|\delta| \gg \Delta\omega_{\text{FS}'}$), the system becomes an $L = 0 \to L' = 1$ transition as depicted in Fig. 7.2b. In that case all transitions have the same transition strength for all polarisations. For that situation we expect no dependence on the polarisation of the FORT light. In this approximation the potential depth and scattering rate are reduced to the expressions Eqs. (3.15) for a two-level system.

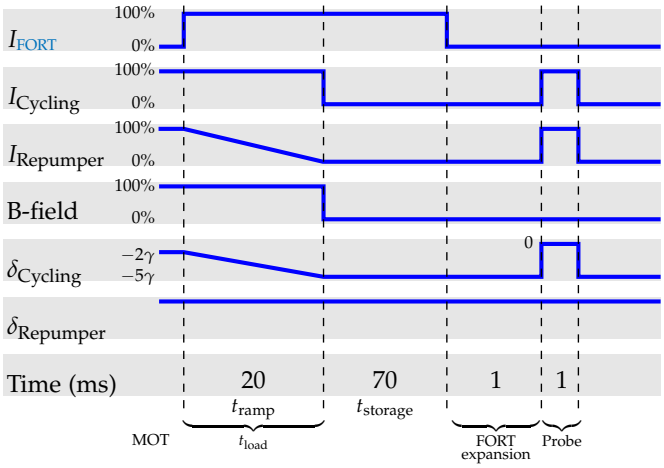

Figure 7.3: Timing of the polarisation dependence measurements. Times are given in ms.

7.2 MEASUREMENTS

For the measurements described in this chapter a quarter-wave plate is inserted between the PBS and the FORT focusing lens displayed in Fig. 4.15.

The typical timing scheme for the polarisation-dependence measurements is shown in Fig. 7.3. After the initial loading of the MOT for 20 s the FORT beam is turned on and the MOT detuning/repump intensity ramp is started. Again $t_{\text{load}} = t_{\text{ramp}} = 20\,\text{ms}$. The atoms are stored in the FORT for $t_{\text{storage}} = 70\,\text{ms}$ to allow them to equilibrate in the new potential and to remove untrapped MOT atoms. Subsequently the FORT beam is turned off and after an expansion time of 1 ms the probe beams are switched on for 1 ms to record a fluorescence image on the CCD. All measurements are performed with ^{85}Rb.

Figure 7.4 shows measurements of the number of atoms in a CW and a ML FORT as a function of the rotation angle θ of the quarter-wave plate for three wavelengths. We verified that the Mira light is linearly polarised in the horizontal plane at $\theta = 56°$, which is where the maxima occur. At $\theta = 11°$ the light is circularly polarised. By replacing the quarter-wave plate with a half-wave plate we verified the number of atoms to be $N_0 = (4.8 \pm 0.5) \cdot 10^5$ at $\lambda = 783\,\text{nm}$, independent of θ. The figures show that atoms can be trapped irrespective of the polarisation, except for the case of a ML laser tuned between the D-lines, where the number of atoms goes to zero when deviating from linear polarisation. However, most atoms are trapped with linearly polarised light. We can parametrise the measurements by using the Airy function to track the data:

$$N(\theta) = \frac{N_0}{1 + K \sin^2(2\theta + \phi)}, \tag{7.1}$$

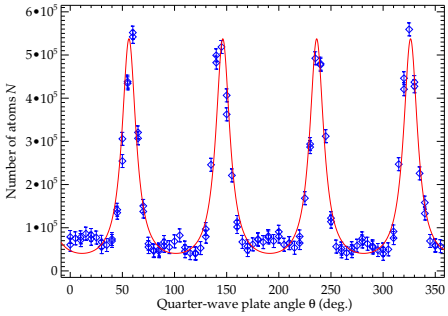

(a) CW, $\lambda = 783\,\mathrm{nm}$.

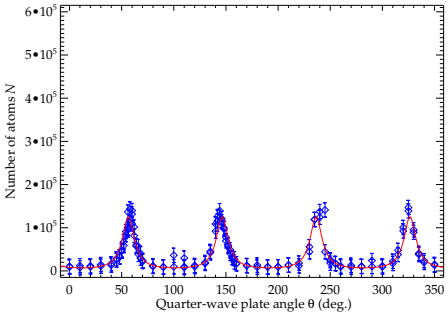

(b) ML, $\lambda = 783\,\mathrm{nm}$.

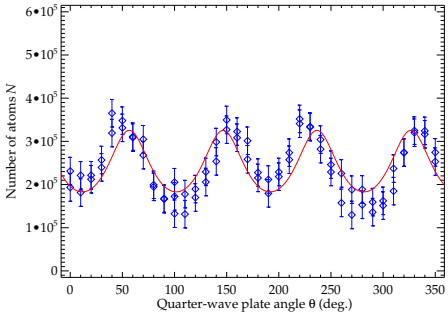

(c) CW, $\lambda = 810\,\mathrm{nm}$.

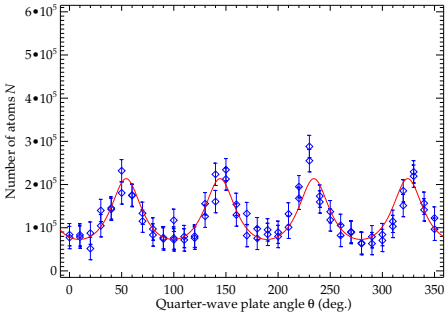

(d) ML, $\lambda = 810\,\mathrm{nm}$.

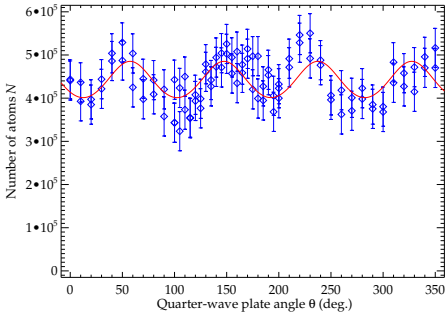

(e) CW, $\lambda = 819\,\mathrm{nm}$.

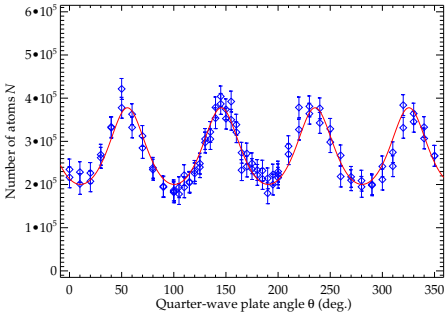

(f) ML, $\lambda = 819\,\mathrm{nm}$.

Figure 7.4: Measurements of the number of atoms in a CW or ML FORT as a function of the rotation angle θ of a quarter-wave plate for several wavelengths. The lines are fits to Eq. (7.1). At $\theta = 56°$ (modulo 90°) the Mira light is linearly polarised and at $\theta = 11°$ (modulo 90°) the light is circularly polarised. Table 7.1 lists experimental parameters and the fit parameters.

CW FORT						
λ	U_0/k_B	Γ_{sc}	N_0 (10^5 atoms)	K	ϕ (°)	$\tilde{\chi}^2$
783	1.0	670	5.37 ± 0.05	12.2 ± 0.3	67.4 ± 0.2	8.47
810	0.55	46.2	3.25 ± 0.08	0.778 ± 0.077	66.7 ± 2.1	1.70
819	0.58	32.4	4.85 ± 0.09	0.209 ± 0.036	65.1 ± 4.6	0.869
ML FORT						
λ	U_0/k_B	Γ_{sc}	N_0 (10^5 atoms)	K	ϕ (°)	$\tilde{\chi}^2$
783	1.1	731	1.25 ± 0.04	16.6 ± 1.8	67.1 ± 0.5	1.07
810	0.58	51.8	2.14 ± 0.07	1.93 ± 0.20	71.3 ± 1.6	0.915
819	0.58	32.4	3.78 ± 0.05	0.885 ± 0.048	69.0 ± 1.1	0.906

Table 7.1: List of experimental parameters and fit parameters for the polarisation-dependence measurements shown in Fig. 7.4 using Eq. (7.1). The FORT wavelength λ is given in nm, U_0/k_B is the calculated potential depth at the centre of the trap for the $m_F = 0/m_J = 0$ level in mK and Γ_{sc} is the calculated scattering rate of that level in Hz.

with N_0 the number of atoms in a linearly polarised FORT. The parameter K is a measure for the contrast, or, equivalently, the width of the peaks. The phase ϕ indicates the relative position of the peaks. The solid lines in Fig. 7.4 are fits to this function, with the fit parameters listed in table 7.1. From the fits in Fig. 7.4 we find that ϕ is the same for all plots. This shows that the maximum in the number of atoms is at the same polarisation (linear) for all experiments.

In the CW measurements (Figs. 7.4a, c and e) we find that K decreases as the detuning increases to the red of the D-lines. This is as we expect from our discussion in § 7.1, where we state that at large detunings the system can be described by a two-level model where the transition strength does not depend on the polarisation of the FORT light. For the ML FORTs (Figs. 7.4b, d and f) this is also observed. Note that the polarisation dependence is more sharply peaked and less sinusoidal than for a CW FORT and thus K is higher than for the CW measurements. The larger K for the ML FORT may be attributed to the bandwidth of 0.65 nm of the pulses, but more likely to the increased scattering due to the high peak intensities during the pulses.

In Fig. 7.4a we note a small increase in N at circular polarisation. In literature the dip in N between $\mathcal{P} = 0$ and $\mathcal{P} = \pm 1$ is attributed to a sharp increase of the losses due to scattering (Γ_S, cf. Eq. (5.10)) if the polarisation deviates from purely linear or purely circular [86]. However, our measurements show that the number of atoms does not fall off as sharply. Furthermore, for wavelengths to the red of

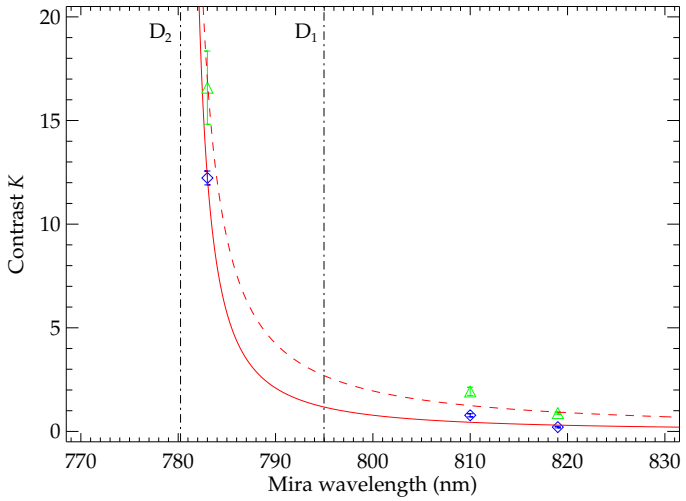

Figure 7.5: Plot of the fitted contrast K as a function of the Mira wavelength. The diamonds (triangles) indicate the CW (ML) measurements. The solid and dashed lines are fits to Eq. (7.2) for CW and ML, respectively. The dash-dotted lines indicate the D-lines.

the D_1 line no increase in N is detected for purely circularly polarised light.

We therefore propose the following. In Fig. 7.5 K is plotted as a function of the FORT wavelength. The lines are fits to

$$K(\delta) \propto 1/\delta_2^b \tag{7.2}$$

where δ_2 refers to the detuning from the D_2 line. In case the difference in the number of atoms trapped in a CFORT would exclusively be limited by the scattering of FORT photons, K scales with $1/\delta_2^2$. Due to optical pumping by σ^+ (σ^-) light the atoms are in the highest (lowest) m_F or m_J state, which do not couple to the D_1 transition (cf. Fig. 7.1). Therefore, the detuning relative to this transition plays no role. In case the different trap depths govern the contrast, K scales with $1/\delta_2$. We find $b = 1.40 \pm 0.04$ and $b = 1.10 \pm 0.04$ for CW and ML, respectively. This suggests that at small detunings δ_2 scattering is determining the contrast K, while at large detuning the trap depth limits the contrast.

7.3 CONCLUSIONS

In this chapter we have shown that it is possible to trap atoms in a FORT created with elliptically polarised light, both using a CW and a ML laser. The number of

trapped atoms depends on the ellipticity of the polarisation of the light. Most atoms are captured when the FORT light is linearly polarised, independent of the detuning. For a CW FORT tuned in between the D-lines we observed a small increase in the number of atoms at circular polarisation. For detunings to the red of the D_1 line the number of atoms always has a minimum at circular polarisation.

The difference in the number of trapped atoms characterised by the contrast parameter K becomes smaller for increasing detunings δ. For small detunings from the D_2 line K is limited by polarisation effects of the scattering, for large detunings by the effective trap depth. This is expected, since at large detunings the internal structure of the atoms and optical pumping effects become increasingly less important and for detunings much larger than the fine structure splitting the atom can be treated as effectively consisting of only two levels. In this case the coupling to the light field is independent of the polarisation.

In literature a decrease in the number of atoms is found when the polarisation deviates from either perfectly linear or perfectly circular. This is attributed to a dramatic increase of the decay rate Γ_S. However, our measurements do not show such a sharp decrease in the number of atoms. We find that difference in the number of atoms is determined by the photon scattering rate at small detunings and by the potential depth at large detunings.

8

SUMMARY AND OUTLOOK

8.1 SUMMARY

The aim of this research is to pave the way for making a trap for cold neutral atoms based on the force generated by pulses of a mode-locked (ML) laser, as explained in Chapter 2. As an onset towards such a trap we decided to use a far-off-resonance trap (FORT) loaded with cold rubidium atoms from a magneto-optical trap (MOT).

In Chapter 4 the experimental setup we built is discussed in detail. The emphasis is on the use of polarisation spectroscopy for the frequency stabilisation of the diode lasers of the MOT, as well as on the time-sequencing software we developed that allows us to time the various phases of a measurement cycle with a guaranteed resolution on the order of 100 µs. Furthermore, the Ti:sapphire laser that is used to make the FORTs is discussed. Our FORTs are typically made in the wavelength range of 780 nm to 830 nm, with a power of several hundred mW to 1 W. In this chapter the main characteristics of our MOT are also presented.

Several characteristics of FORTs made with continuous-wave (CW) and ML lasers are presented in Chapter 5, where we have investigated the loading behaviour of the traps, as well as their lifetimes. Furthermore we presented measurements of the temperature of the trapped atoms.

We looked at the effects of parametric excitation of the atoms in the FORT in Chapter 6. The anharmonicity of the trap results in interesting physics, including a change in the average temperature of the atoms, depending on the modulation frequency. We also investigated the trapping behaviour of the FORT at low pulse repetition rates by switching the laser intensity on and off on a kHz scale.

In Chapter 7 we looked at the dependence of the number of atoms on the polarisation of the FORT laser light, both for CW and ML traps. Atoms can be trapped at elliptical polarisations as well, although the number of trapped atoms is less. As the laser is detuned further to the red of the D_1 line, this effect becomes less and less pronounced, as predicted by our model.

8.2 OUTLOOK

The results obtained in this research are promising. We have a working setup, in which atoms can be trapped with a single ML laser beam. Therefore, the basic necessities are fulfilled to extend the setup with a second, counterpropagating ML laser beam. The major difficulties in setting up such a trap are the proper alignment of the foci of the two beams in space as well making sure that the pulses overlap in the centre of the atom cloud.

We have performed simulations of the dual-beam trap based on the work of Temkin and Krüger, which are promising [160, 161]. However, due to the Gaussian propagation of the beam it is impossible to make π-pulse at every position in the atom cloud, which may lead to heating of the atoms. Therefore, we propose to use the MOT laser beams in order to provide extra cooling. Using modern frequency doubling or tripling techniques this kind of setup can be used to trap elements that were hitherto beyond the reach of experimentalists. Moreover, since this trap does not require a closed two-level system, it could be used to trap molecules as well and therefore holds large promise for future experiments.

A

CALCULATING THE BEAM WAIST FROM TWO KNIFE EDGE MEASUREMENTS

In § 4.5.4 a method is described to determine the waist of a laser beam by doing a knife edge measurement of the beam radius at two positions in the beam. This appendix provides further details on the calculation involved. A Gaussian beam is determined by one parameter only, its waist w_0, and since the only other unknown quantity is the exact location of the waist (at position $z = 0$), we only need two measurements of the beam radius and the distance between them to uniquely determine these two quantities.

First, the beam size is measured at position z:

$$w(z)^2 = w_0^2 \left(1 + \frac{z^2}{z_R^2}\right) = w_0^2 + \frac{\lambda^2 z^2}{\pi^2 w_0^2}, \tag{A.1}$$

since $z_R = \frac{\pi w_0^2}{\lambda}$ is the Rayleigh length. Subsequently, the size is determined at position $z + d$:

$$w(z+d)^2 = w_0^2 \left(1 + \frac{(z+d)^2}{z_R^2}\right) = w_0^2 + \frac{\lambda^2 (z+d)^2}{\pi^2 w_0^2}. \tag{A.2}$$

Subtracting the beam size at position z yields:

$$w(z+d)^2 - w(z)^2 = \frac{\lambda^2}{\pi^2 w_0^2} \left\{ d^2 + 2dz \right\}, \tag{A.3}$$

which can be rewritten as

$$z = \frac{\pi^2 w_0^2}{2d\lambda^2} \left\{ w(z+d)^2 - w(z)^2 \right\} - \frac{d}{2}. \tag{A.4}$$

Using Eq. (A.4), Eq. (A.1) reads:

$$w(z)^2 = w_0^2 + \frac{\pi^2 w_0^2}{4d^2\lambda^2} \left\{ w(z+d)^2 - w(z)^2 \right\}^2 - \frac{1}{2} \left\{ w(z+d)^2 - w(z)^2 \right\} + \frac{d^2\lambda^2}{4\pi^2 w_0^2}. \tag{A.5}$$

Multiplying Eq. (A.5) by $2\,w_0^2$ yields:

$$\left(2+\frac{\pi^2}{2d^2\lambda^2}\left\{w(z+d)^2-w(z)^2\right\}^2\right)w_0^4 - \left\{w(z+d)^2+w(z)^2\right\}w_0^2+\frac{d^2\lambda^2}{2\pi^2}=0. \quad \text{(A.6)}$$

Non-trivial solutions of this equation are:

$$w_0^2=\frac{-b\pm\sqrt{b^2-4ac}}{2a}, \quad \text{(A.7)}$$

where

$$a=2+\frac{\pi^2}{2d^2\lambda^2}\left\{w(z+d)^2-w(z)^2\right\}^2,$$
$$b=-\left\{w(z+d)^2+w(z)^2\right\},$$
$$c=\frac{d^2\lambda^2}{2\pi^2}.$$

The result of this calculation is the waist size w_0 as a function of the two measured values $w(z)$ and $w(z+d)$. Using this waist, the distance z from the first measurement point to the position of the waist can be extracted from Eq. (A.3).

B

CHARACTERISTIC RUBIDIUM DATA

B.1 GENERAL PROPERTIES

This section contains tables with characteristic values of the most important parameters used for laser cooling and trapping of rubidium.

The electronic ground state of $_{37}$Rb is:

$$1s^2\ 2s^2\ 2p^6\ 3s^2\ 3p^6 4s^2\ 3d^{10}\ 4p^6\ 5s$$

Figure B.1 shows the Rb levels accessible by our Ti:Sapphire laser and the corresponding energies of the levels.

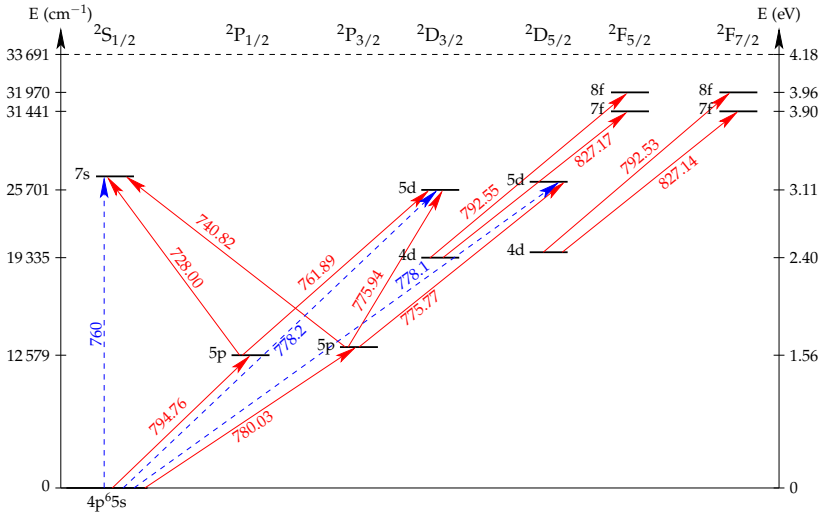

Figure B.1: Energy level diagram for Rb with transitions available in the Mira tuning range. All wavelengths are given in nm for air. The dashed arrows indicate two-photon transitions. Data taken from Refs. [162–166].

PROPERTY	SYMBOL	VALUE
Laser cooling transition		$5\,^2\mathrm{S}_{1/2}\,F=3 \rightarrow 5\,^2\mathrm{P}_{3/2}\,F'=4$
Natural abundance		72.17 %
Nuclear spin	I	$^5/_2$
Wavelength (*in vacuo*)	λ	780.243 855 568 nm [167]
Lifetime of upper state	τ_{Rb}	26.63 ns
Natural linewidth	$\gamma/2\pi$	5.98 MHz
Saturation intensity, for $\lvert F{=}3, m_F{=}3\rangle \rightarrow \lvert F'{=}4, m_{F'}{=}4\rangle$	I_{sat}	1.669 mW/cm^2 [72]
Mass	m	84.911 789 732 u [168]
Ionisation limit		33 690.7989 cm^{-1} [166]
		4.177 105 7 eV

Table B.1: General properties of ^{85}Rb.

PROPERTY	SYMBOL	VALUE
Laser cooling transition		$5\,^2\mathrm{S}_{1/2}\,F = 2 \rightarrow 5\,^2\mathrm{P}_{3/2}\,F' = 3$
Natural abundance		27.83 %
Nuclear spin	I	$^3/_2$
Wavelength (*in vacuo*)	λ	780.246 020 749 nm [164]
Lifetime of upper state	τ_{Rb}	26.24 ns
Natural linewidth	$\gamma/2\pi$	6.065 MHz
Saturation intensity, for $\lvert F{=}2,\, m_F{=}2\rangle \rightarrow \lvert F'{=}3,\, m_{F'}{=}3\rangle$	I_{sat}	1.669 mW/cm^2 [73]
Mass	m	86.909 180 520 u [168]
Ionisation limit		33 690.8048 cm^{-1} [166]
		4.177 127 0 eV

Table B.2: General properties of ^{87}Rb.

v_{D} (Doppler limit)	11.85 cm/s
T_{D}	143.41 µK
v_{r} (recoil limit)	0.602 cm/s
T_{r}	0.370 µK

Table B.3: Limiting values for velocity and temperature.

B.2 HYPERFINE SPLITTING

The hyperfine splitting of both rubidium isotopes is shown in figure B.2. For laser cooling the D_2 transition ($5\,^2S_{1/2} \rightarrow 5\,^2P_{3/2}$) is used, more specifically, the $F = 3 \rightarrow F' = 4$ hyperfine levels for ^{85}Rb and $F = 2 \rightarrow F' = 3$ for ^{87}Rb. The repump lasers excite the $F = 2 \rightarrow F' = 3$ and $F = 1 \rightarrow F' = 2$ transitions for ^{85}Rb and ^{87}Rb, respectively.

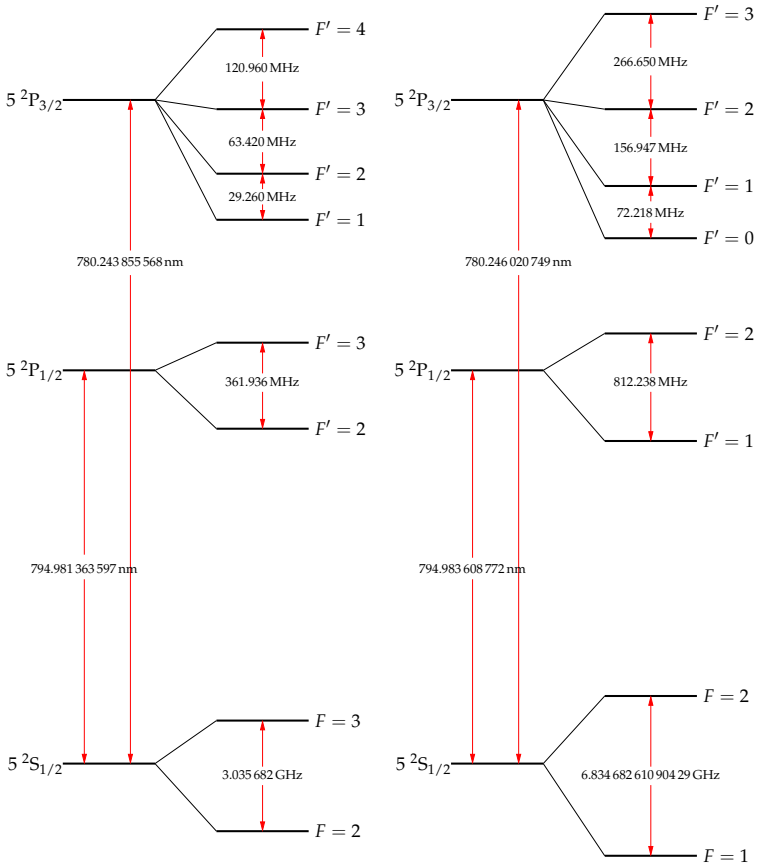

(a) ^{85}Rb (b) ^{87}Rb

Figure B.2: Energy level diagram of the Rb hyperfine levels of the D_1 and the D_2 line (not to scale). The values for the transition wavelengths are in vacuum. Data taken from Refs. [164, 167, 169–174].

B.3 TRANSITION STRENGTHS

Figures B.3 and B.4 show the transition strengths for the D_2-line for both rubidium isotopes [74]. Only the strengths for π-polarised light and σ^+-polarised light are shown, the strengths for σ^--polarised light can be found by using the σ^+ diagram and replacing the quantum numbers m_F by $-m_F$. All strengths are normalised to the weakest transition, which is ^{87}Rb $|F = 2, m_F = 0\rangle \rightarrow |F' = 1, m_{F'} = 1\rangle$ for σ^+-light. The diagrams of ^{85}Rb (^{87}Rb) can be used for any alkali with a nuclear spin $I = 5/2$ ($I = 3/2$).

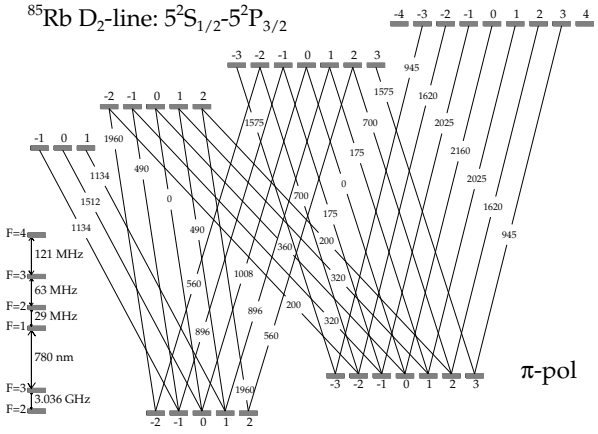

Figure B.3: Transition strengths for ^{85}Rb for π and σ^+-polarised light. (More accurate values for the hyperfine splittings can be found in Fig. B.2.)

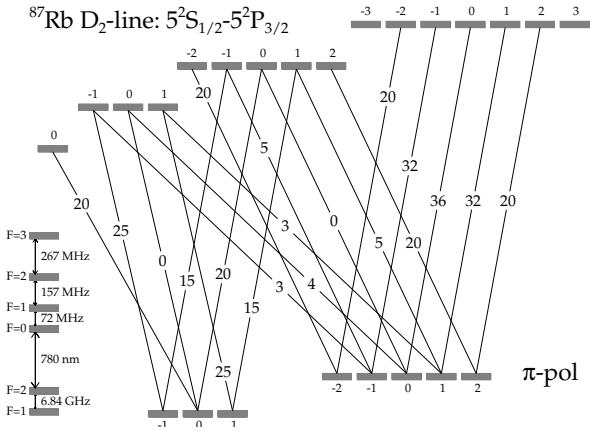

(a)

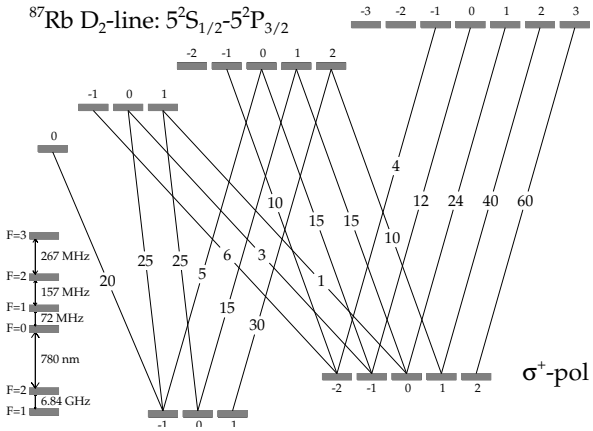

(b)

Figure B.4: Transition strengths for ^{87}Rb for π and σ^+-polarised light. (More accurate values for the hyperfine splittings can be found in Fig. B.2.)

C

COLOUR PRINTS OF SELECTED FIGURES

This appendix contains colour prints of selected figures from this thesis.

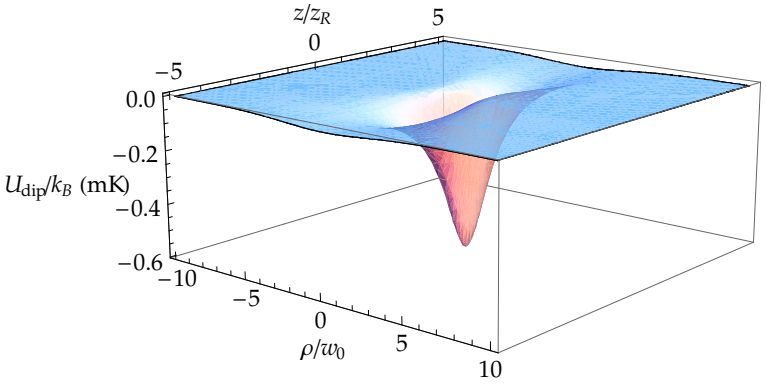

Figure C.1: The FORT potential of a red detuned Gaussian beam for the properties listed in table 3.1. Note that the aspect ratio of the ρ and z axis is not 1 : 1. This is a colour print of Fig. 3.1 on page 16.

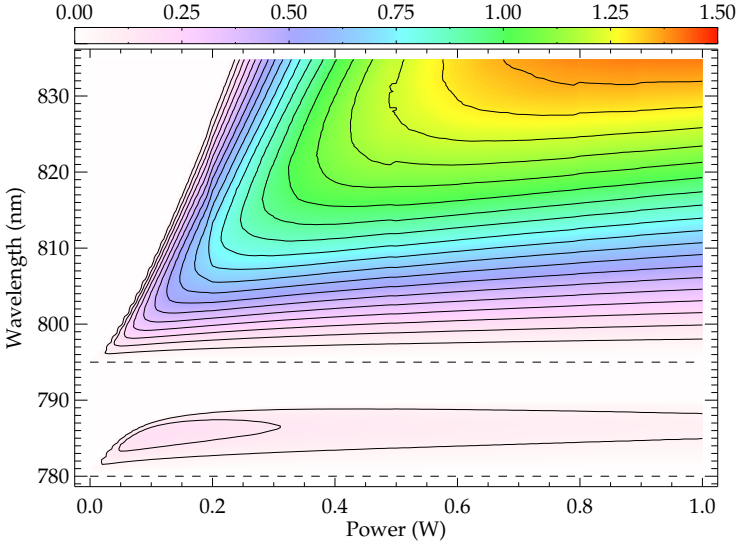

Figure C.2: Simulation of the lifetime of a FORT as a function of the wavelength and the power of the FORT laser. The colour bar indicates the 1/e lifetime in seconds. The positions of the D-lines are indicated by the dashed lines. This is a colour print of Fig. 3.3 on page 17.

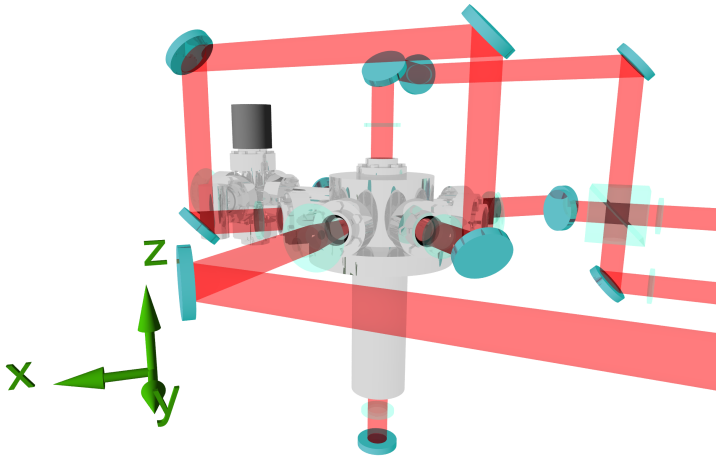

Figure C.3: 3D rendering of the vacuum chamber including the optical beams. This is a colour print of Fig. 4.7 on page 33.

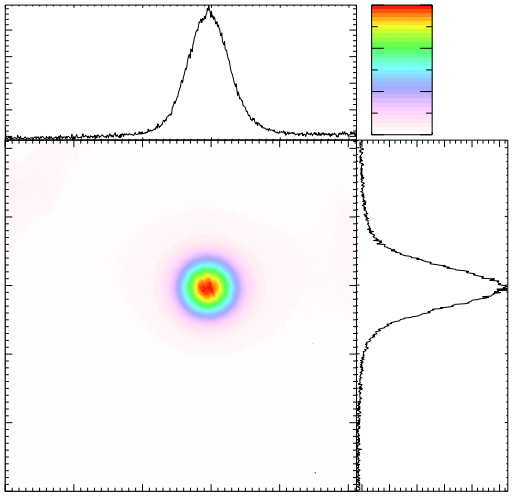

Figure C.4: Fluorescence image of the MOT taken after an expansion time of 18 ms. The trapping laser detuning is 24 MHz. This is a colour print of Fig. 4.25 on page 61.

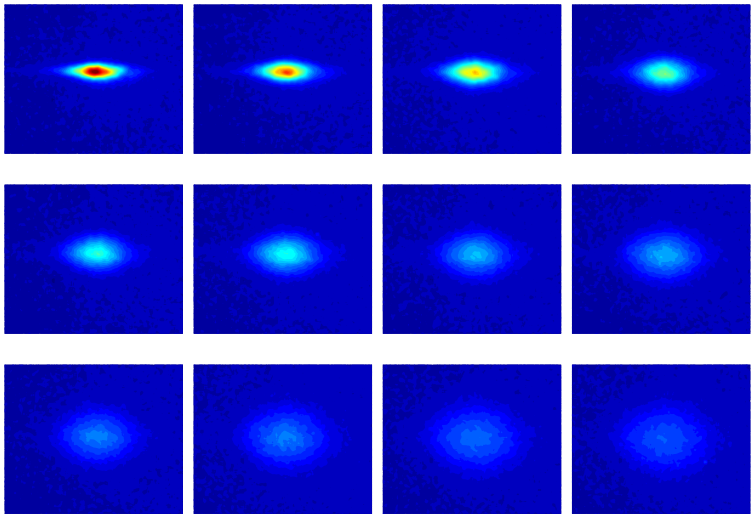

Figure C.5: Series of images of an expanding ^{85}Rb CW FORT making up a temperature measurement. The images where taken after an expansion time of 1 to 6.5 ms at intervals of 0.5 ms. The images have identical false-colour scales. This is a colour print of Fig. 5.9 on page 75.

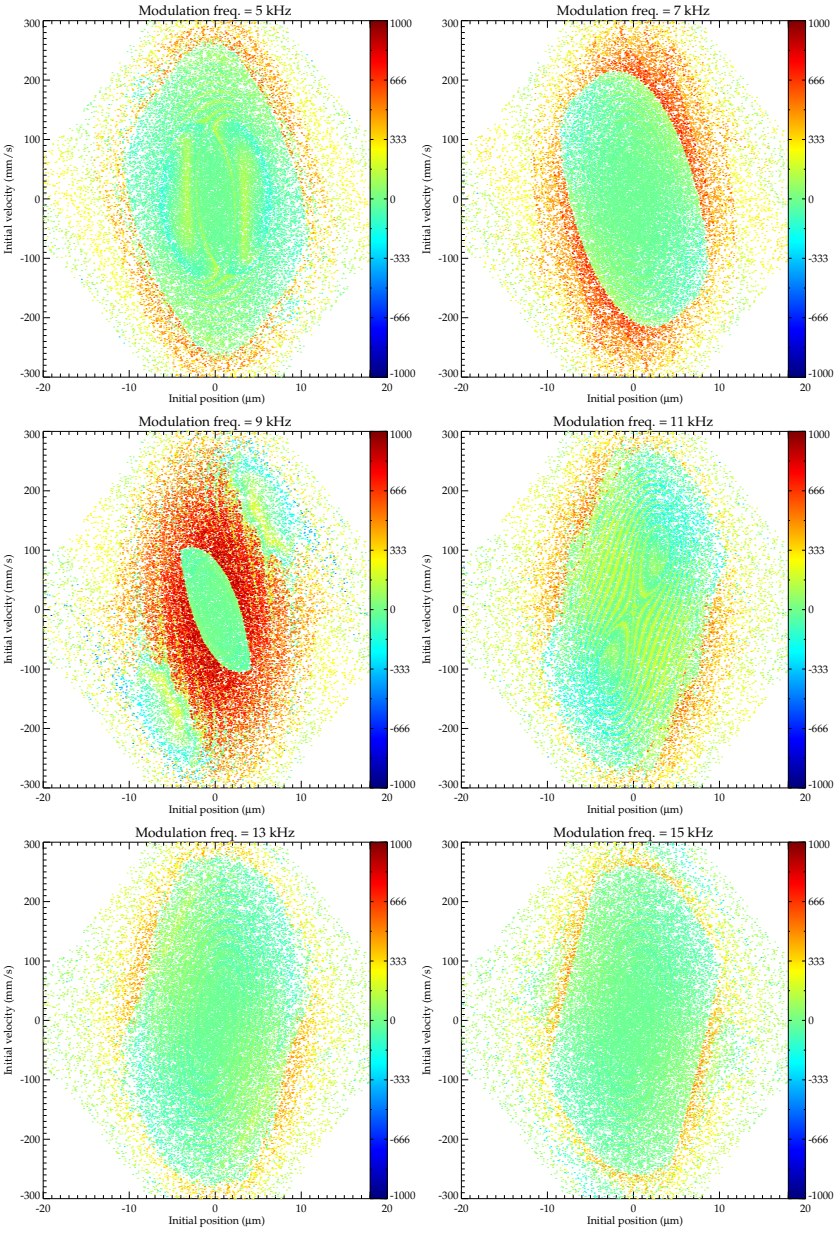

Figure C.6: Phase space plots of the atoms in a FORT whose depth is modulated at different frequencies as indicated above the individual plots. All images have the same colour scale that indicates the heating rate in μK/s. This is a colour print of Fig. 6.6 on page 85.

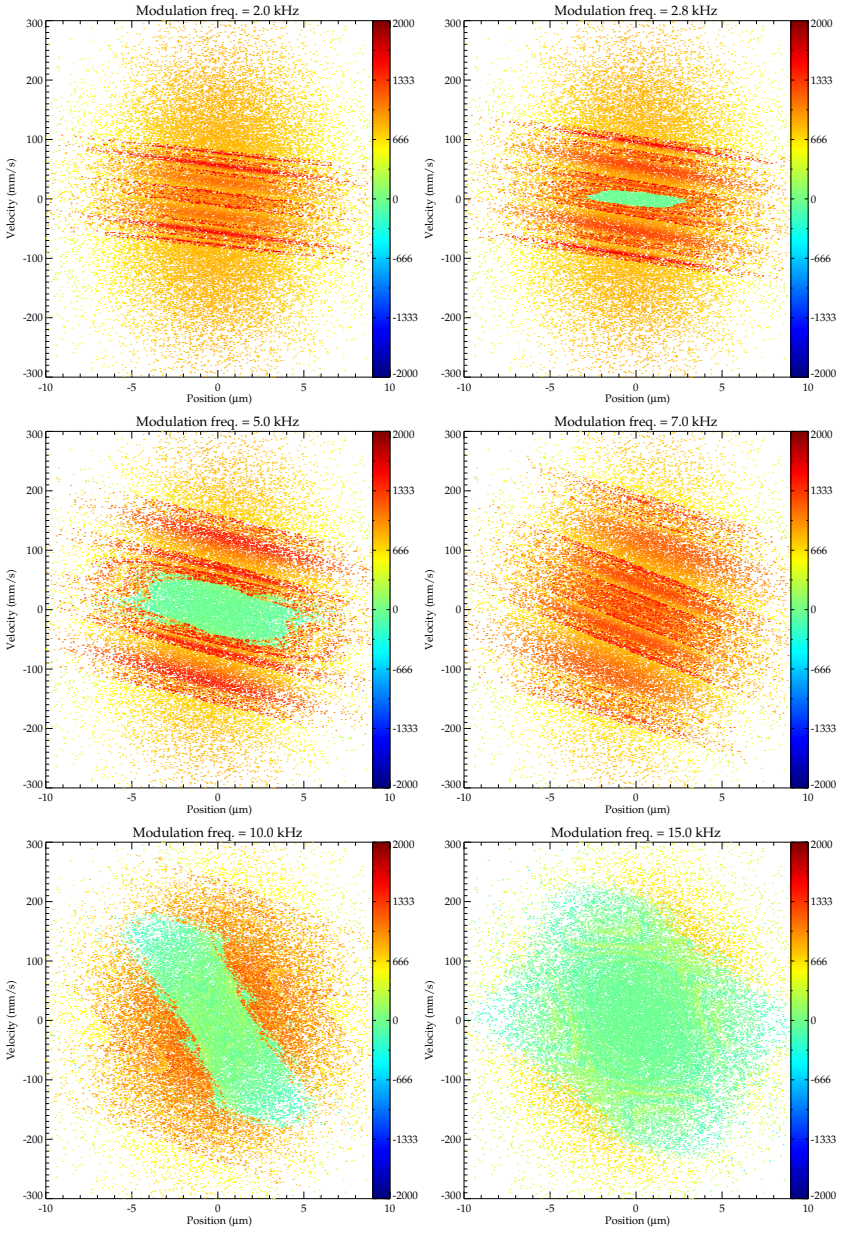

Figure C.7: Phase space plots of the atoms in a FORT whose depth is modulated at different frequencies as indicated above the individual plots. All images have the same colour scale that indicates the heating rate in µK/s. This is a colour print of Fig. 6.9 on page 89.

LIST OF ACRONYMS AND SYMBOLS

ACRONYMS

AO	analog output (of the DAQ card)
AOM	acousto-optic modulator
BEC	Bose-Einstein condensate
CFORT	circular FORT, FORT made with circularly polarised light
CW	continuous-wave (operational mode of a laser)
DAQ	data acquisition
DIO	digital input/output (of the DAQ card)
FORT	far-off-resonance trap, ODT made several nm from resonance
FPI	Fabry-Pérot interferometer
MOT	magneto-optical trap
ML	mode-locked (operational mode of a laser)
ODT	optical dipole trap
OI	optical isolator
PBS	polarising beamsplitter cube
PD	photodiode
QUEST	quasi-electrostatic trap, ODT made several hundred nm from resonance, where the atomic polarisability can be considered static
RTAI	Real-Time Application Interface for Linux
RWA	rotating wave approximation

SYMBOLS

δ laser detuning from the atomic resonance, $\omega - \omega_0$.

η ratio of $k_B T / U_0$ in the FORT.

f_{rep} repetition rate of the Mira laser, $f_{rep} = 76\,\text{MHz}$.

γ natural lifetime of rubidium (cf. Appendix B).

$\boldsymbol{k}$ wavevector of a laser, $k = 2\pi/\lambda$.

m atomic mass of rubidium (cf. Appendix B).

Ω the Rabi frequency.

P_{Mira} (time-averaged) Mira output power.

s_0 saturation parameter on resonance (cf. Eq. (3.28)).

T temperature of MOT or FORT.

U_0 the trap depth of the FORT (cf. Eq. (3.22)).

w_0 laser beam waist, the $1/e^2$ beam radius.

z_R Rayleigh range of a focused laser beam, $z_R = \pi w_0^2 / \lambda$.

BIBLIOGRAPHY

The references include a Digital Object Identifier (DOI) where available. The DOI provides a simple way to refer to a digital document. Simply add the DOI to the URL http://dx.doi.org/.

[1] A. Ashkin. *Acceleration and trapping of particles by radiation pressure*. Phys. Rev. Lett., **24**: 156–159, 1970. DOI: 10.1103/PhysRevLett.24.156. (Cited on page 1.)

[2] A. Ashkin. *Atomic-beam deflection by resonance-radiation pressure*. Phys. Rev. Lett., **25**: 1321–1324, 1970. DOI: 10.1103/PhysRevLett.25.1321. (Cited on page 1.)

[3] A. Ashkin. *Trapping of atoms by resonance radiation pressure*. Phys. Rev. Lett., **40**: 729–732, 1978. DOI: 10.1103/PhysRevLett.40.729. (Cited on page 1.)

[4] J.E. Bjorkholm, R.R. Freeman, A. Ashkin, and D.B. Pearson. *Observation of focusing of neutral atoms by the dipole forces of resonance-radiation pressure*. Phys. Rev. Lett., **41**: 1361–1364, 1978. DOI: 10.1103/PhysRevLett.41.1361. (Cited on page 1.)

[5] E.L. Raab, M. Prentiss, A. Cable, S. Chu, and D.E. Pritchard. *Trapping of neutral sodium atoms with radiation pressure*. Phys. Rev. Lett., **59**: 2631–2634, 1987. DOI: 10.1103/PhysRevLett.59.2631. (Cited on pages 1, 7, and 21.)

[6] M.H. Anderson, J.R. Ensher, M.R. Matthews, C.E. Wieman, and E.A. Cornell. *Observation of Bose-Einstein condensation in a dilute atomic vapor*. Science, **269**: 198–201, 1995. DOI: 10.1126/science.269.5221.198. (Cited on pages 1 and 7.)

[7] M.D. Barret, J.A. Sauer, and M.S. Chapman. *All-optical formation of an atomic Bose-Einstein condensate*. Phys. Rev. Lett., **87**: 010404, 2001. DOI: 10.1103/PhysRevLett.87.010404. (Cited on page 1.)

[8] S. Schlunk, A. Marian, P. Geng, A.P. Mosk, G. Meijer, and W. Schöllkopf. *Trapping of Rb atoms by ac electric fields*. Phys. Rev. Lett., **98**: 223002, 2007. DOI: 10.1103/PhysRevLett.98.223002. (Cited on page 1.)

[9] S. Chu, J.E. Bjorkholm, A. Ashkin, and A. Cable. *Experimental observation of optically trapped atoms*. Phys. Rev. Lett., **57**: 314–317, 1986. DOI: 10.1103/PhysRevLett.57.314. (Cited on page 2.)

[10] J.D. Miller, R.A. Cline, and D.J. Heinzen. *Far-off-resonance optical trapping of atoms*. Phys. Rev. A, **47**: R4567–R4570, 1993. DOI: 10.1103/PhysRevA.47.R4567. (Cited on pages 2, 13, and 43.)

[11] T. Takekoshi, J.R. Yeh, and R.J. Knize. *Quasi-electrostatic trap for neutral atoms*. Opt. Comm., **114**: 421–424, 1995. DOI: 10.1016/0030-4018(94)00638-B. (Cited on pages 2 and 13.)

[12] T. Takekoshi and R.J. Knize. *CO_2 laser trap for cesium atoms*. Opt. Lett., **21**: 77–79, 1996. URL: http://www.opticsinfobase.org/abstract.cfm?URI=ol-21-1-77. (Cited on pages 2 and 13.)

[13] J.D. Simon. *Ultrashort light pulses*. Rev. Sci. Instr., **60**: 3597–3624, 1989. DOI: 10.1063/1.1140516. (Cited on page 2.)

[14] S. Backus, C.G. Durfee III, M.M. Murnane, and H.C. Kapteyn. *High power ultrafast lasers*. Rev. Sci. Instr., **69**: 1207–1223, 1998. DOI: 10.1063/1.1148795. (Cited on page 2.)

[15] D.H. Steinmeyer, G.and Sutter, L. Gallmann, N. Matuschek, and U. Keller. *Frontiers in ultrashort pulse generation: Pushing the limits in linear and nonlinear optics*. Science, **286**: 1507–1512, 1999. DOI: 10.1126/science.286.5444.1507. (Cited on page 2.)

[16] G.D Reid and K. Wynne. *Ultrafast laser technology and spectroscopy*. In R.A. Meyers, editor, *Encyclopedia of Analytical Chemistry: Instrumentation and Applications*, pages 13644–13670. John Wiley & Sons, 2000. URL: http://bcp.phys.strath.ac.uk/the_group/r/uf/2000-EAC.pdf. (Cited on page 2.)

[17] T.H. Maiman. *Stimulated optical radiation in ruby*. Nature, **187**: 493–494, 1960. DOI: 10.1038/187493a0. (Cited on page 2.)

[18] L.E. Hargrove, R.L. Fork, and M.A. Pollack. *Locking of He-Ne laser modes induced by synchronous intracavity modulation*. Appl. Phys. Lett., **5**: 4–5, 1964. DOI: 10.1063/1.1754025. (Cited on page 2.)

[19] M. Hentschel, R. Kienberger, Ch. Spielmann, G.A. Reider, N. Milosevic, T. Brabec, P. Corkum, U. Heinzmann, M. Drescher, and F. Krausz. *Attosecond metrology*. Nature, **414**: 509–513, 2001. DOI: 10.1038/35107000. (Cited on page 2.)

[20] E. Goulielmakis, M. Schultze, M. Hofstetter, V.S. Yakovlev, J. Gagnon, M. Uiberacker, A.L. Aquila, E.M. Gullikson, D.T. Attwood, R. Kienberger, F. Krausz, and U. Kleineberg. *Single-cycle nonlinear optics*. Science, **320**: 1614–1617, 2008. DOI: 10.1126/science.1157846. (Cited on page 2.)

[21] Th. Udem, J. Reichert, R. Holzwarth, and T.W. Hänsch. *Accurate measurement of large optical frequency differences with a mode-locked laser*. Opt. Lett., **24**: 881–883, 1999. DOI: 10.1364/OL.24.000881. (Cited on pages 2 and 42.)

[22] D.J. Jones, S.A. Diddams, J.K. Ranka, A. Stentz, R.S. Windeler, J.L. Hall, and S.T. Cundiff. *Carrier-Envelope Phase Control of Femtosecond Mode-Locked Lasers and Direct Optical Frequency Synthesis*. Science, **288**: 635–639, 2000. DOI: 10.1126/science.288.5466.635. (Cited on page 2.)

[23] S.T. Cundiff, J. Ye, and J.L. Hall. *Optical frequency synthesis based on mode-locked lasers*. Rev. Sci. Instr., **72**: 3749–3771, 2001. DOI: 10.1063/1.1400144. (Cited on page 2.)

[24] Th. Udem, R. Holzwarth, and T.W. Hänsch. *Optical frequency metrology*. Nature, **416**: 233–237, 2002. DOI: 10.1038/416233a. (Cited on page 2.)

[25] C.P. Koch, R. Kosloff, and F. Masnou-Seeuws. *Short-pulse photoassociation in rubidium below the D_1 line*. Phys. Rev. A, **73**: 043409, 2006. DOI: 10.1103/PhysRevA.73.043409. (Cited on pages 2 and 43.)

[26] B.L. Brown, A.J. Dicks, and I.A. Walmsley. *The coherent effect of chirped femtosecond laser pulses on the formation of ultracold molecules in a magneto-optical trap*. Opt. Comm., **264**: 278—-284, 2006. DOI: 10.1016/j.optcom.2006.04.084. (Cited on pages 2, 7, and 43.)

[27] R. Wester, S.D. Kraft, M. Mudrich, M.U. Staudt, J. Lange, N. Vanhaecke, O. Dulieu, and M. Weidemüller. *Photoassociation inside an optical dipole trap: absolute rate coefficients and Franck–Condon factors*. Appl. Phys. B, **79**: 993–999, 2004. DOI: 10.1007/s00340-004-1649-5. (Cited on pages 2, 7, and 43.)

[28] D. Felinto, C.A.C. Bosco, L.H. Acioli, and S.S. Vianna. *Coherent accumulation in two-level atoms excited by a train of ultrashort pulses*. Opt. Comm., **215**: 69–73, 2003. DOI: 10.1016/S0030-4018(02)02230-7. (Cited on page 2.)

[29] D. Felinto, L.H. Acioli, and S.S. Vianna. *Accumulative effects in the coherence of three-level atoms excited by femtosecond-laser frequency combs*. Phys. Rev. A, **70**: 043403, 2004. DOI: 10.1103/PhysRevA.70.043403. (Cited on page 2.)

[30] V. Gerginov, C.E. Tanner, S. Diddams, A. Bartels, and L. Hollberg. *Optical frequency measurements of $6s\,^2S_{1/2} - 6p\,^2P_{3/2}$ transition in a ^{133}Cs atomic beam using a femtosecond laser frequency comb*. Phys. Rev. A, **70**: 042505, 2004. DOI: 10.1103/PhysRevA.70.042505. (Cited on page 2.)

[31] T.M. Fortier, Y. Le Coq, J.E. Stalnaker, D. Ortega, S.A. Diddams, C.W. Oates, and L. Hollberg. *Kilohertz-resolution spectroscopy of cold atoms with an optical frequency comb*. Phys. Rev. Lett., **97**: 163905, 2006. DOI: 10.1103/PhysRevLett.97.163905. (Cited on page 2.)

[32] M. Bellini, A. Bartoli, and T.W. Hänsch. *Two-photon fourier spectroscopy with femtosecond light pulses*. Opt. Lett., **22**: 540–542, 1997. DOI: 10.1364/OL.22.000540. (Cited on page 2.)

[33] S. Wolf and H. Helm. *Ion-recoil momentum spectroscopy in a laser-cooled atomic sample*. Phys. Rev. A, **62**: 043408, 2000. DOI: 10.1103/PhysRevA.62.043408. (Cited on page 2.)

[34] P.F. Barker and M.N. Shneider. *Optical microlinear accelerator for molecules and atoms*. Phys. Rev. A, **64**: 033408, 2001. DOI: 10.1103/PhysRevA.64.033408. (Cited on page 2.)

[35] N. Piovella, V. Beretta, G.R. M. Robb, and R. Bonifacio. *Photon echo in the super-radiant light scattering from a Bose-Einsteins condensate*. Phys. Rev. A, **68**: 021801, 2003. DOI: 10.1103/PhysRevA.68.021801. (Cited on page 2.)

[36] P. Strohmeier, T. Kersebom, E. Krüger, H. Nölle, B. Steuter, J. Schmand, and Andrä J. *Na-atom beam deceleration by a mode-locked laser*. Opt. Comm., **73**: 451–454, 1989. DOI: 10.1016/0030-4018(89)90460-4. (Cited on pages 2 and 6.)

[37] P. Strohmeier, A. Horn, T. Kersebom, and J. Schmand. *Na-beam cooling by a mode-locked laser*. Z. Phys. D, **21**: 215–219, 1991. DOI: 10.1007/BF01426376. (Cited on pages 2 and 6.)

[38] B. Nölle, H. Nölle, J. Schmand, and H.J. Andrä. *Atomic-beam deflection by double-π-pulse laser technique*. Europhys. Lett., **33**: 261–266, 1996. DOI: 10.1209/epl/i1996-00330-9. (Cited on pages 2 and 6.)

[39] A. Goepfert, I. Bloch, D. Haubrich, F. Lison, R. Schütze, R. Wynands, and D. Meschede. *Stimulated focusing and deflection of an atomic beam using picosecond laser pulses*. Phys. Rev. A, **56**: R3354–R3357, 1997. DOI: 10.1103/PhysRevA.56.R3354. (Cited on pages 2 and 6.)

[40] M. Mützel, D. Haubrich, and D. Meschede. *Nanoscale focusing of atoms with a pulsed standing wave*. Appl. Phys. B, **70**: 689–694, 2000. DOI: 10.1007/s003400050882. (Cited on pages 2 and 6.)

[41] T.G.M. Freegarde, J. Walz, and T.W. Hänsch. *Confinement and manipulation of atoms using short laser pulses*. Opt. Comm., **117**: 262–267, 1995. DOI: 10.1016/0030-4018(95)00172-5. (Cited on page 2.)

[42] A.P. Kazantsev. *The acceleration of atoms by light*. JETP, **39**: 784, 1974. (Cited on page 5.)

[43] X. Miao, E. Wertz, M.G. Cohen, and H. Metcalf. *Strong optical forces from adiabatic rapid passage*. Phys. Rev. A, **75**: 011402, 2007. DOI: 10.1103/PhysRevA.75.011402. (Cited on page 6.)

[44] J. Söding, R. Grimm, Y.B. Ovchinnikov, P. Bouyer, and C. Salomon. *Short-distance atomic beam deceleration with a stimulated light force*. Phys. Rev. Lett., **78**: 1420–1423, 1997. DOI: 10.1103/PhysRevLett.78.1420. (Cited on page 6.)

[45] M.R. Williams, F. Chi, M.T. Cashen, and H. Metcalf. *Bichromatic force measurements using atomic beam deflections*. Phys. Rev. A, **61**: 023408, 2000. DOI: 10.1103/PhysRevA.61.023408. (Cited on page 6.)

[46] M.T. Cashen and H. Metcalf. *Bichromatic force on helium*. Phys. Rev. A, **63**: 025406, 2001. DOI: 10.1103/PhysRevA.63.025406. (Cited on page 6.)

[47] M. Cashen, O. Rivoire, V. Romanenko, L. Yatsenko, and H. Metcalf. *Strong optical forces in frequency-modulated light*. Phys. Rev. A, **64**: 063411, 2001. DOI: 10.1103/PhysRevA.64.063411. (Cited on page 6.)

[48] I.D. Setija, H.G.C. Werij, O.J. Luiten, M.W. Reynolds, T.W. Hijmans, and J.T.M. Walraven. *Optical cooling of atomic hydrogen in a magnetic trap*. Phys. Rev. Lett., **70**: 2257–2260, 1993. DOI: 10.1103/PhysRevLett.70.2257. (Cited on page 7.)

[49] D.G. Fried, T.C. Killian, L. Willmann, D. Landhuis, S.C. Moss, D. Kleppner, and T.J. Greytak. *Bose-Einstein condensation of atomic hydrogen*. Phys. Rev. Lett., **81**: 3811–3814, 1998. DOI: 10.1103/PhysRevLett.81.3811. (Cited on page 7.)

[50] F. Shimizu, K. Shimizu, and H. Takuma. *Laser cooling and trapping of ne metastable atoms*. Phys. Rev. A, **39**: 2758–2760, 1989. DOI: 10.1103/PhysRevA.39.2758. (Cited on page 7.)

[51] G.R. Woestenenk. *Photoassociation of cold metastable helium atoms*. PhD thesis, Utrecht University, 2001. URL: http://igitur-archive.library.uu.nl/dissertations/1954684/inhoud.htm. (Cited on page 7.)

[52] M. van Rijnbach. *Dynamical spectroscopy of transient He_2 molecules*. PhD thesis, Utrecht University, 2004. URL: http://igitur-archive.library.uu.nl/dissertations/2004-0120-094105/inhoud.htm. (Cited on page 7.)

[53] J. Lawall, S. Kulin, B. Saubamea, N. Bigelow, M. Leduc, and C. Cohen-Tannoudji. *Three-dimensional laser cooling of helium beyond the single-photon recoil limit*. Phys. Rev. Lett., **75**: 4194–4197, 1995. DOI: 10.1103/PhysRevLett.75.4194. (Cited on page 7.)

[54] K. Honda, Y. Takahashi, T. Kuwamoto, M. Fujimoto, K. Toyoda, K. Ishikawa, and T. Yabuzaki. *Magneto-optical trapping of Yb atoms and a limit on the branching ratio of the $^1P_1$ state*. Phys. Rev. A, **59**: R934–R937, 1999. DOI: 10.1103/PhysRevA.59.R934. (Cited on page 7.)

[55] E. te Sligte, B. Smeets, K.M.R. van der Stam, R.W. Herfst, P. van der Straten, H.C.W. Beijerinck, and K.A.H. van Leeuwen. *Atom lithography of Fe*. Appl. Phys. Lett., **85**: 4493–4495, 2004. DOI: 10.1063/1.1818347. (Cited on page 7.)

[56] J.R. Guest, N.D. Scielzo, I. Ahmad, K. Bailey, J.P. Greene, R.J. Holt, Z.-T. Lu, T.P. O'Connor, and D.H. Potterveld. *Laser trapping of ^{225}Ra and ^{226}Ra with repumping by room-temperature blackbody radiation*. Phys. Rev. Lett., **98**: 093001, 2007. DOI: 10.1103/PhysRevLett.98.093001. (Cited on page 7.)

[57] Q. Beaufils, R. Chicireanu, T. Zanon, B. Laburthe-Tolra, E. Maréchal, L. Vernac, J.-C. Keller, and O. Gorceix. *All-optical production of chromium Bose-Einstein condensates*. Phys. Rev. A, **77**: 061601, 2008. DOI: 10.1103/PhysRevA.77.061601. (Cited on page 7.)

[58] H.L. Bethlem, G. Berden, F.M.H. Crompvoets, R.T. Jongma, A.J.A. van Roij, and G. Meijer. *Electrostatic trapping of ammonia molecules*. Nature, **406**: 491–494, 2000. DOI: 10.1038/35020030. (Cited on page 7.)

[59] F. Lang, P. van der Straten, B. Brandstätter, G. Thalhammer, K. Winkler, P.S. Julienne, R. Grimm, and J. Hecker Denschlag. *Cruising through molecular bound-state manifolds with radiofrequency*. Nature Physics, **4**: 223–226, 2008. DOI: 10.1038/nphys838. (Cited on page 7.)

[60] E.A. Shapiro, M. Shapiro, A. Pe'er, and J. Ye. *Photoassociation adiabatic passage of ultracold Rb atoms to form ultracold Rb_2 molecules*. Phys. Rev. A, **75**: 013405, 2007. DOI: 10.1103/PhysRevA.75.013405. (Cited on page 7.)

[61] E.A. Shapiro, M. Shapiro, A. Pe'er, and J. Ye. *Erratum: Photoassociation adiabatic passage of ultracold Rb atoms to form ultracold Rb_2 molecules [Phys. Rev. A 75, 013405 (2007)]*. Phys. Rev. A, **78**: 029903, 2008. DOI: 10.1103/PhysRevA.78.029903. (Cited on page 7.)

[62] S. Chu, L. Hollberg, J.E. Bjorkholm, A. Cable, and A. Ashkin. *Three-dimensional viscous confinement and cooling of atoms by resonance radiation pressure*. Phys. Rev. Lett., **55**: 48–51, 1985. DOI: 10.1103/PhysRevLett.55.48. (Cited on pages 7 and 19.)

[63] S.G. Crane, X. Zhao, W. Taylor, and D.J. Vieira. *Trapping an isotopic mixture of fermionic ^{84}Rb and bosonic ^{87}Rb atoms*. Phys. Rev. A, **62**: 011402, 2000. DOI: 10.1103/PhysRevA.62.011402. (Cited on pages 7 and 8.)

[64] J. Goldwin, S.B. Papp, B. DeMarco, and D.S. Jin. *Two-species magneto-optical trap with ^{40}K and ^{87}Rb*. Phys. Rev. A, **65**: 021402, 2002. DOI: 10.1103/PhysRevA.65.021402. (Cited on page 7.)

[65] S.R. Granade, M.E. Gehm, K.M. O'Hara, and J.E. Thomas. *All-optical production of a degenerate Fermi gas*. Phys. Rev. Lett., **88**: 120405, 2002. DOI: 10.1103/PhysRevLett.88.120405. (Cited on pages 7 and 13.)

[66] C. Thibault, F. Touchard, S. Büttgenbach, R. Klapisch, M. de Saint Simon, H.T. Duong, P. Jacquinot, P. Juncar, S. Liberman, P. Pillet, J. Pinard, J.L. Vialle, A. Pesnelle, and G. Huber. *Hyperfine structure and isotope shift of the D_2 line of $^{76-98}$Rb and some of their isomers*. Phys. Rev. C, **23**: 2720–2729, 1981. DOI: 10.1103/PhysRevC.23.2720. (Cited on page 8.)

[67] R. Guckert, X. Zhao, S.G. Crane, A. Hime, W.A. Taylor, D. Tupa, D.J. Vieira, and H. Wollnik. *Magneto-optical trapping of radioactive ^{82}Rb atoms*. Phys. Rev. A, **58**: R1637–R1640, 1998. DOI: 10.1103/PhysRevA.58.1637. (Cited on page 8.)

[68] D. Feldbaum, H. Wang, J. Weinstein, D. Vieira, and X. Zhao. *Trapping radioactive ^{82}Rb in an optical dipole trap and evidence of spontaneous spin polarization*. Phys. Rev. A, **76**: 051402, 2007. DOI: 10.1103/PhysRevA.76.051402. (Cited on page 8.)

[69] J.L. Roberts. *Bose-Einstein Condensates with Tunable Atom-atom Interactions: The First Experiments with ^{85}Rb BECs*. PhD thesis, JILA, 2001. URL: http://jilawww.colorado.edu/pubs/thesis/roberts/. (Cited on page 8.)

[70] D.R. Lide, editor. *Handbook of Chemistry and Physics*. CRC Press, 87th edition, 2006. (Cited on page 8.)

[71] A.M. van der Spek, J.J.L. Mulders, and L.W.G. Steenhuysen. *Vapor pressure of rubidium between 250 and 298 K determined by combined fluorescence and absorption measurements*. J. Opt. Soc. Am. B, **5**: 1478–1483, 1988. URL: http://www.opticsinfobase.org/abstract.cfm?URI=josab-5-7-1478. (Cited on page 8.)

[72] D.A. Steck. *Rubidium 85 D line data*, 2008. URL: http://steck.us/alkalidata/. (Cited on pages 8, 14, 19, and 104.)

[73] D.A. Steck. *Rubidium 87 D line data*, 2008. URL: http://steck.us/alkalidata/. (Cited on pages 8, 14, 19, and 105.)

[74] H.J. Metcalf and P. van der Straten. *Laser Cooling and Trapping*. Springer, 2002. (Cited on pages 9, 18, 21, and 107.)

[75] R. Grimm, M. Weidemüller, and Y.B. Ovchinnikov. *Optical dipole traps for neutral atoms*. Adv. At., Mol., Opt. Phys., **42**: 95–133, 2000. (Cited on pages 9, 10, 13, and 14.)

[76] D.A. Steck. *Quantum and atom optics*, 2008. URL: http://steck.us/teaching. (Cited on pages 9, 10, and 11.)

[77] J.P. Gordon and A. Ashkin. *Motion of atoms in a radiation trap*. Phys. Rev. A, **21**: 1606–1617, 1980. DOI: 10.1103/PhysRevA.21.1606. (Cited on page 9.)

[78] J. Dalibard and C. Cohen-Tannoudji. *Dressed-atom approach to atomic motion in laser light: the dipole force revisited*. J. Opt. Soc. Am. B, **2**: 1707–1720, 1985. URL: http://www.opticsinfobase.org/abstract.cfm?URI=josab-2-11-1707. (Cited on pages 9 and 13.)

[79] V.E. Lembessis and D. Ellinas. *Optical dipole trapping beyond the rotating wave approximation: the case of large detuning*. J. Opt. B, **7**: 319–322, 2005. DOI: 10.1088/1464-4266/7/11/002. (Cited on page 12.)

[80] T. Kuga, Y. Torii, N. Shiokawa, T. Hirano, Y. Shimizu, and H. Sasada. *Novel optical trap of atoms with a doughnut beam*. Phys. Rev. Lett., **78**: 4713–4716, 1997. DOI: 10.1103/PhysRevLett.78.4713. (Cited on page 13.)

[81] Y. Torii, N. Shiokawa, T. Hirano, T. Kuga, Y. Shimizu, and H. Sasada. *Pulsed polarization gradient cooling in an optical dipole trap with a Laguerre-Gaussian laser beam*. Eur. Phys. J. D, **1**: 239–242, 1998. DOI: 10.1007/s100530050088. (Cited on page 13.)

[82] T. Puppe, I. Schuster, A. Grothe, A. Kubanek, K. Murr, P.W.H. Pinkse, and G. Rempe. *Trapping and observing single atoms in a blue-detuned intracavity dipole trap*. Phys. Rev. Lett., **99**: 013002, 2007. DOI: 10.1103/PhysRevLett.99.013002. (Cited on page 13.)

[83] K.M. O'Hara, S.R. Granade, M.E. Gehm, and J.E. Thomas. *Loading dynamics of CO_2 laser traps*. Phys. Rev. A, **63**: 043403, 2001. DOI: 10.1103/PhysRevA.63.043403. (Cited on page 13.)

[84] P.F. Griffin. *Laser Cooling and Loading of Rb into A Large Period, Quasi-Electrostatic, Optical Lattice*. PhD thesis, Department of Physics, Durham University, 2005. URL: http://massey.dur.ac.uk/resources/pfgriffin/. (Cited on page 13.)

[85] J. Dalibard and C. Cohen-Tannoudji. *Laser cooling below the Doppler limit by polarization gradients: simple theoretical models*. J. Opt. Soc. Am. B, **6**: 2023–2045, 1989. URL: http://josab.osa.org/abstract.cfm?URI=josab-6-11-2023. (Cited on pages 13 and 21.)

[86] K.L. Corwin, S.J.M. Kuppens, D. Cho, and C.E. Wieman. *Spin-polarized atoms in a circularly polarized optical dipole trap*. Phys. Rev. Lett., **83**: 1311–1314, 1999. DOI: 10.1103/PhysRevLett.83.1311. (Cited on pages 14, 91, and 95.)

[87] B.H. Bransden and C.J. Joachain. *Physics of atoms and molecules*. Addison Wesley Longman, 1983. (Cited on page 14.)

[88] R.B.M. Clarke, T. Graf, and E. Riis. *Dipole traps with mode-locked lasers*. Appl. Phys. B, **70**: 695–700, 2000. DOI: 10.1007/s003400050883. (Cited on pages 14, 65, and 66.)

[89] P.D. Lett, W.D. Phillips, S.L. Rolston, C.E. Tanner, R.N. Watts, and C.I. Westbrook. *Optical molasses*. J. Opt. Soc. Am. B, **6**: 2084–2107, 1989. URL: http://www.opticsinfobase.org/abstract.cfm?URI=josab-6-11-2084. (Cited on pages 19 and 20.)

[90] D. Suter. *The physics of Laser-Atom Interactions*. Cambridge University Press, 1997. (Cited on page 20.)

[91] P.A. Molenaar. *Photoassociative reactions of laser-cooled sodium*. PhD thesis, Utrecht University, 1996. (Cited on page 27.)

[92] E.A. Donley, T.P. Heavner, F. Levi, and S.R. Jefferts. *Double-pass acousto-optic modulator system*. Rev. Sci. Instr., **76**: 063112, 2005. DOI: 10.1063/1.1930095. (Cited on page 31.)

[93] C.E. Wieman and T.W. Hänsch. *Doppler-free laser polarization spectroscopy*. Phys. Rev. Lett., **36**: 1170–1173, 1976. DOI: 10.1103/PhysRevLett.36.1170. (Cited on page 33.)

[94] T.W. Hänsch and B. Couillaud. *Laser frequency stabilization by polarization spectroscopy of a reflecting reference cavity*. Opt. Comm., **35**: 441–444, 1980. DOI: 10.1016/0030-4018(80)90069-3. (Cited on page 33.)

[95] G.P.T. Lancaster, R.S. Conroy, M.A. Clifford, J. Arlt, and K. Dholakia. *A polarisation spectrometer locked diode laser for trapping cold atoms*. Opt. Comm., **170**: 79–84, 1999. DOI: 10.1016/S0030-4018(99)00433-2. (Cited on page 33.)

[96] C.P. Pearman, C.S. Adams, S.G. Cox, P.F. Griffin, D.A. Smith, and I.G. Hughes. *Polarization spectroscopy of a closed atomic transition: applications to laser frequency locking*. J. Phys. B, **35**: 5141–5151, 2002. DOI: 10.1088/0953-4075/35/24/315. (Cited on pages 33 and 35.)

[97] Y. Yoshikawa, T. Umeki, T. Mukae, Y. Torii, and T. Kuga. *Frequency stabilization of a laser diode with use of light-induced birefringence in an atomic vapor*. Appl. Opt., **45**: 6645–6649, 2003. URL: http://www.opticsinfobase.org/abstract.cfm?URI=ao-42-33-6645. (Cited on pages 33 and 42.)

[98] M.L. Harris, C.S. Adams, S.L. Cornish, I.C. McLeod, E. Tarleton, and I.G. Hughes. *Polarization spectroscopy in rubidium and cesium*. Phys. Rev. A, **73**: 062509, 2006. DOI: 10.1103/PhysRevA.73.062509. (Cited on pages 33 and 42.)

[99] W. Demtröder. *Laser spectroscopy, Basic Concepts and Instrumentation*. Springer-Verlag, 2nd enlarged edition edition, 1996. (Cited on pages 33 and 35.)

[100] A.I. Ferguson, J.N Eckstein, and T.W. Hänsch. *Polarization spectroscopy with ultrashort light pulses*. Appl. Phys, **18**: 257–260, 1979. DOI: 10.1007/BF00885511. (Cited on page 33.)

[101] K.L. Corwin, Z.-T. Lu, C.F. Hand, R.J. Epstein, and C.E. Wieman. *Frequency-stabilized diode laser with the Zeeman shift in an atomic vapor*. Appl. Opt., **37**: 3295–3298, 1998. DOI: 10.1364/AO.37.003295. (Cited on page 42.)

[102] K.J. Weatherill. *A CO_2 Laser Lattice Experiment for Cold Atoms*. PhD thesis, Department of Physics, Durham University, 2007. URL: http://massey.dur.ac.uk/resources/kjweatherill/. (Cited on page 42.)

[103] G. Wasik, W. Gawlik, J. Zachorowski, and W. Zawadzki. *Laser frequency stabilization by doppler-free magnetic dichroism*. Appl. Phys. B, **75**: 613–619, 2002. DOI: 10.1007/s00340-002-1041-2. (Cited on page 42.)

[104] T. Petelski, M. Fattori, G. Lamporesi, J. Stuhler, and G.M. Tino. *Doppler-free spectroscopy using magnetically induced dichroism of atomic vapor: a new scheme for laser frequency locking*. Eur. Phys. J. D, **22**: 279–283, 2003. DOI: 10.1140/epjd/e2002-00238-4. (Cited on page 42.)

[105] T. Brabec, C. Spielmann, P.F. Curley, and F. Krausz. *Kerr lens mode locking*. Opt. Lett., **17**: 1292–1294, 1992. URL: http://www.opticsinfobase.org/abstract.cfm?URI=ol-17-18-1292. (Cited on page 42.)

[106] R.A. Cline, J.D. Miller, and D.J. Heinzen. *Study of Rb_2 long-range states by high-resolution photoassociation spectroscopy*. Phys. Rev. Lett., **73**: 632–635, 1994. DOI: 10.1103/PhysRevLett.73.632. (Cited on page 43.)

[107] R.A. Cline, J.D. Miller, and D.J. Heinzen. *Erratum: Study of Rb_2 long-range states by high-resolution photoassociation spectroscopy*. Phys. Rev. Lett., **73**: 2636, 1994. DOI: 10.1103/PhysRevLett.73.2636. (Cited on page 43.)

[108] *Operator's Manual for the Coherent MIRA Model 900-P Laser*. Coherent Laser Group, 3210 Porter Drive, P.O. Box 10042, Palo Alto, California 94303. (Cited on page 43.)

[109] T.A. Savard, K.M. O'Hara, and J.E. Thomas. *Laser-noise-induced heating in far-off resonance optical traps*. Phys. Rev. A, **56**: R1095–R1098, 1997. DOI: 10.1103/PhysRevA.56.R1095. (Cited on pages 44 and 77.)

[110] M.E. Gehm, K.M. O'Hara, T.A. Savard, and J.E. Thomas. *Dynamics of noise-induced heating in atom traps*. Phys. Rev. A, **58**: 3914–3921, 1998. DOI: 10.1103/PhysRevA.58.3914. (Cited on pages 44 and 77.)

[111] T. Ban, D. Aumiler, H. Skenderović, and G. Pichler. *Mapping of the optical frequency comb to the atom-velocity comb*. Phys. Rev. A, **73**: 043407, 2006. DOI: 10.1103/PhysRevA.73.043407. (Cited on page 46.)

[112] T. Ban, D. Aumiler, H. Skenderović, S. Vdović, N. Vujičić, and G. Pichler. *Cancellation of the coherent accumulation in rubidium atoms excited by a train of femtosecond pulses*. Phys. Rev. A, **76**: 043410, 2007. DOI: 10.1103/PhysRevA.76.043410. (Cited on page 46.)

[113] P. Vledder, M. Megens, and J.I Dijkhuis. *On the stability of the cavity modes of a mode locked Ti:Sapphire laser*. Internal Report. (Cited on page 46.)

[114] P.R. Jorden and A.P. Oates. *Scientific CCD Prospects for 1994 and Beyond*. In A.G.D. Philip, B. Hauck, and A.R. Upgren, editors, *New Developments in Array Technology and Applications*, volume 167 of *IAU Symposium*, pages 27–+, 1995. (Cited on page 50.)

[115] K. Singer, S. Jochim, M. Mudrich, A. Mosk, and M. Weidemüller. *Low-cost mechanical shutter for light beams*. Rev. Sci. Instr., **73**: 4402–4404, 2002. DOI: 10.1063/1.1520728. (Cited on page 51.)

[116] L.P. Maguire, S. Szilagyi, and R.E. Scholten. *High performance laser shutter using a hard disk drive voice-coil actuator*. Rev. Sci. Instr., **75**: 3077–3079, 2004. DOI: 10.1063/1.1786331. (Cited on page 52.)

[117] L.P. Maguire, S. Szilagyi, and R.E. Scholten. *Erratum: High performance laser shutter using a hard disk drive voice-coil actuator*. Rev. Sci. Instr., **78**: 019903, 2007. DOI: 10.1063/1.2409774. (Cited on page 52.)

[118] R.E. Scholten. *Enhanced laser shutter using a hard disk drive rotary voice-coil actuator*. Rev. Sci. Instr., **78**:026101, 2007. DOI: 10.1063/1.2437199. (Cited on page 52.)

[119] *The website of the RTAI project*. URL: http://www.rtai.org. (Cited on pages 55 and 56.)

[120] *The website of the Comedi project*. URL: http://www.comedi.org. (Cited on page 55.)

[121] H. Bruyninckx. *Real-time and embedded guide*. Technical report, Dept. of Mechanical Engineering, KU Leuven, 2002. URL: http://people.mech.kuleuven.be/~bruyninc/rthowto/. (Cited on page 56.)

[122] R. Bucher, S. Mannori, and T. Netter. *RTAI-Lab tutorial: Scilab, Comedi, and real-time control*, 2007. URL: http://www.rtai.org/RTAILAB. (Cited on page 56.)

[123] *The website of the free RTLinux project*. URL: http://www.rtlinuxfree.com. (Cited on page 56.)

[124] P. Sarolahti. *Real-time application interface*. Technical report, Department of Computer Science, University of Helsinki, 2001. URL: http://people.nokia.net/~sarolaht/papers/rtai.pdf. (Cited on page 56.)

[125] M.T. Jones. *Anatomy of the Linux kernel*. IBM DeveloperWorks, 2007. URL: http://www.ibm.com/developerworks/linux/library/l-linux-kernel/. (Cited on page 56.)

[126] T.P. Dinneen, C.D. Wallace, K.-Y.N. Tan, and P.L. Gould. *Use of trapped atoms to measure absolute photoionization cross sections*. Opt. Lett., **17**: 1706–1708, 1992. URL: http://www.opticsinfobase.org/abstract.cfm?URI=ol-17-23-1706. (Cited on page 60.)

[127] M.H. Shah, H.A. Camp, M.L. Trachy, G. Veshapidze, M.A. Gearba, and B.D. DePaola. *Model-independent measurement of the excited fraction in a magneto-optical trap*. Phys. Rev. A, **75**: 053418, 2007. DOI: 10.1103/PhysRevA.75.053418. (Cited on page 60.)

[128] C.D. Wallace, T.P. Dinneen, K.Y.N. Tan, A. Kumarakrishnan, P.L. Gould, and J. Javanainen. *Measurements of temperature and spring constant in a magneto-optical trap*. J. Opt. Soc. Am. B, **11**: 703–711, 1994. URL: http://www.opticsinfobase.org/abstract.cfm?URI=josab-11-5-703. (Cited on pages 61 and 63.)

[129] C.G. Townsend, N.H. Edwards, C.J. Cooper, K.P. Zetie, C.J. Foot, A.M. Steane, P. Szriftgiser, H. Perrin, and J. Dalibard. *Phase-space density in the magneto-optical trap*. Phys. Rev. A, **52**: 1423–1440, 1995. DOI: 10.1103/PhysRevA.52.1423. (Cited on page 61.)

[130] A. Vorozcovs, M. Weel, S. Beattie, S. Cauchi, and A. Kumarakrishnan. *Measurements of temperature scaling laws in an optically dense magneto-optical trap*. J. Opt. Soc. Am. B, **22**: 943–950, 2005. DOI: 10.1364/JOSAB.22.000943. (Cited on pages 61 and 63.)

[131] D. Hoffmann, P. Feng, R.S. Williamson, and T. Walker. *Excited-state collisions of trapped ^{85}Rb atoms*. Phys. Rev. Lett., **69**: 753–756, 1992. DOI: 10.1103/PhysRevLett.69.753. (Cited on pages 63 and 64.)

[132] A.G. Sinclair, E. Riis, and M.J. Snadden. *Improved trapping in a vapor-cell magneto-optical trap with multiple laser frequencies*. J. Opt. Soc. Am. B, **11**: 233–2339, 1994. URL: http://www.opticsinfobase.org/abstract.cfm?URI=josab-11-12-2333. (Cited on page 63.)

[133] B.P. Anderson and M.A. Kasevich. *Loading a vapor-cell magneto-optic trap using light-induced atom desorption*. Phys. Rev. A, **63**: 023404, 2001. DOI: 10.1103/PhysRevA.63.023404. (Cited on page 63.)

[134] C. Monroe, W. Swann, H. Robinson, and C.E. Wieman. *Very cold trapped atoms in a vapor cell*. Phys. Rev. Lett., **65**: 1571–1574, 1990. DOI: 10.1103/PhysRevLett.65.1571. (Cited on page 63.)

[135] D. Hoffmann, P. Feng, and T. Walker. *Measurements of Rb trap-loss collision spectra*. J. Opt. Soc. Am. B, **11**: 712–720, 1994. URL: http://www.opticsinfobase.org/abstract.cfm?URI=josab-11-5-712. (Cited on page 64.)

[136] C.D. Wallace, T.P. Dinneen, K.-Y.N. Tan, T.T. Grove, and P.L. Gould. *Isotopic difference in trap loss collisions of laser cooled rubidium atoms*. Phys. Rev. Lett., **69**: 897–900, 1992. DOI: 10.1103/PhysRevLett.69.897. (Cited on page 64.)

[137] S.D. Gensemer, V. Sanchez-Villicana, K.Y.N. Tan, T.T. Grove, and P.L. Gould. *Trap-loss collisions of ^{85}Rb and ^{87}Rb: Dependence on trap parameters*. Phys. Rev. A, **56**: 4055–4063, 1997. DOI: 10.1103/PhysRevA.56.4055. (Cited on page 64.)

[138] M. Shiddiq, E.M. Ahmed, M.D. Havey, and C.I. Sukenik. *Investigation of loading of pulsed and continuous-wave optical dipole force traps*. Phys. Rev. A, **77**:045401, 2008. DOI: 10.1103/PhysRevA.77.045401. (Cited on pages 65, 66, 67, 70, and 72.)

[139] S.J.M. Kuppens, K.L. Corwin, K.W. Miller, T.E. Chupp, and C.E. Wieman. *Loading an optical dipole trap*. Phys. Rev. A, **62**: 013406, 2000. DOI: 10.1103/PhysRevA.62.013406. (Cited on pages 65, 69, 70, 74, and 76.)

[140] K.L. Corwin. *A circularly-polarized optical dipole trap and other developments in laser trapping of atoms*. PhD thesis, University of Colorado, 1999. URL: http://jilawww.colorado.edu/pubs/thesis/corwin/. (Cited on pages 65 and 91.)

[141] J. Wu, R. Newell, M. Hausmann, D.J. Vieira, and X. Zhao. *Loading dynamics of optical trap and parametric excitation resonances of trapped atoms*. J. Appl. Phys., **100**:054903, 2006. DOI: 10.1063/1.2266164. (Cited on pages 67, 69, and 77.)

[142] M. Abramowitz and I.A. Stegun. *Handbook of Mathematical Functions with Formulas, Graphs, and Mathematical Tables*. Dover, New York, tenth gpo printing edition, 1964. ISBN 0-486-61272-4. URL: http://www.math.sfu.ca/~cbm/aands/frameindex.htm. (Cited on page 70.)

[143] S. Zhang and J. Jin. *Computation of Special Functions*. John Wiley and Sons, Inc., 1996. URL: http://jin.ece.uiuc.edu/specfunc.html. (Cited on page 70.)

[144] P.G. Petrov, D. Oblak, C.L. Garrido Alzar, N. Kjærgaard, and E.S. Polzik. *Nondestructive interferometric characterization of an optical dipole trap*. Phys. Rev. A, **75**: 033803, 2007. DOI: 10.1103/PhysRevA.75.033803. (Cited on pages 70 and 74.)

[145] S. Dürr, K.W. Miller, and C.E. Wieman. *Improved loading of an optical dipole trap by suppression of radiative escape*. Phys. Rev. A, **63**: 011401(R), 2000. DOI: 10.1103/PhysRevA.63.011401. (Cited on page 70.)

[146] M. Schulz. *Tightly confined atoms in optical dipole traps*. PhD thesis, Institut für Experimentalphysik, Innsbruck, 2002. URL: http://heart-c704.uibk.ac.at/publications/dissertation/schulz_diss.pdf. (Cited on pages 72, 74, and 77.)

[147] G. Roati, W. Jastrzebski, A. Simoni, G. Modugno, and M. Inguscio. *Optical trapping of cold fermionic potassium for collisional studies*. Phys. Rev. A, **63**: 052709, 2001. DOI: 10.1103/PhysRevA.63.052709. (Cited on pages 76 and 77.)

[148] R. Jáuregui. *Nonperturbative and perturbative treatments of parametric heating in atom traps*. Phys. Rev. A, **64**: 053408, 2001. DOI: 10.1103/PhysRevA.64.053408. (Cited on page 77.)

[149] S. Friebel, C. D'Andrea, J. Walz, M. Weitz, and T.W. Hänsch. *CO_2-laser optical lattice with cold rubidium atoms*. Phys. Rev. A, **57**: R20–R23, 1998. DOI: 10.1103/PhysRevA.57.R20. (Cited on page 77.)

[150] S. Friebel, R. Scheunemann, J. Walz, T.W. Hänsch, and M. Weitz. *Laser cooling in a CO_2-laser optical lattice*. Appl. Phys. B, **67**: 699–704, 1998. DOI: 10.1007/s003400050568. (Cited on page 77.)

[151] R. Jáuregui, N. Poli, G. Roati, and G. Modugno. *Anharmonic parametric excitation in optical lattices*. Phys. Rev. A, **64**: 033403, 2001. DOI: 10.1103/PhysRevA.64.033403. (Cited on page 77.)

[152] N. Poli, R.J. Brecha, G. Roati, and G. Modugno. *Cooling atoms in an optical trap by selective parametric excitation*. Phys. Rev. A, **65**: 021401, 2002. DOI: 10.1103/PhysRevA.65.021401. (Cited on pages 77 and 84.)

[153] K. Kim, H.-R. Noh, and W. Jhe. *Parametric resonance in an intensity-modulated magneto-optical trap*. Opt. Comm., **236**: 349–361, 2004. DOI: 10.1016/j.optcom.2004.03.040. (Cited on page 77.)

[154] J. Joykutty, V. Mathur, V. Venkataraman, and V. Natarajan. *Direct measurement of the oscillation frequency in an optical-tweezers trap by parametric excitation*. Phys. Rev. Lett., **95**: 193902, 2005. DOI: 10.1103/PhysRevLett.95.193902. (Cited on page 77.)

[155] L.D. Landau and E.M. Lifshitz. *Mechanics*. Course of Theoretical Physics. Pergamom, 3rd edition, 1976. (Cited on page 78.)

[156] E.I. Butikov. *Parametric excitation of a linear oscillator*. Eur. J. Phys., **25**: 535–554, 2004. DOI: 10.1088/0143-0807/25/4/009. (Cited on page 78.)

[157] M. Kumakura, Y. Shirahata, Y. Takasu, Y. Takahashi, and T. Yabuzaki. *Shaking-induced cooling of cold atoms in a magnetic trap*. Phys. Rev. A, **68**: 021401, 2003. DOI: 10.1103/PhysRevA.68.021401. (Cited on page 81.)

[158] E.A.L. Henn, K.M.F. Magalhães, S.R. Muniz, R.R. Silva, L.G. Marcassa, and V.S. Bagnato. *Variation of the mean kinetic temperature of magnetically trapped atoms by external shaking perturbation*. Laser Phys. Lett., **1**: 621–627, 2004. DOI: 10.1002/lapl.200410149. (Cited on page 84.)

[159] K.W. Miller, S Dürr, and C.E. Wieman. *rf-induced Sisyphus cooling in an optical dipole trap*. Phys. Rev. A, **66**: 023406, 2002. DOI: 10.1103/PhysRevA.66.023406. (Cited on page 91.)

[160] R.J. Temkin. *Excitation of an atom by a train of short pulses*. J. Opt. Soc. Am. B, **10**: 830–839, 1993. URL: http://www.opticsinfobase.org/abstract.cfm?URI=josab-10-5-830. (Cited on page 100.)

[161] E. Krüger. *Excitation of two-level atoms in mode-locked laser fields*. Z. Phys. D, **31**: 13–25, 1994. DOI: 10.1007/BF01426572. (Cited on page 100.)

[162] J.E. Sansonetti. *Wavelengths, transition probabilities, and energy levels for the spectra of rubidium (Rb I through Rb XXXVII)*. J. Phys. Chem. Ref. Data, **35**: 301–421, 2006. DOI: 10.1063/1.2035727. (Cited on page 104.)

[163] A.J. Olson, E.J. Carlson, and S.K. Mayer. *Two-photon spectroscopy of rubidium using a grating-feedback diode laser*. Am. J. Phys., **74**: 218–223, 2006. DOI: 10.1119/1.2173278. (Cited on page 104.)

[164] A. Marian, M.C. Stowe, D. Felinto, and J. Ye. *Direct frequency comb measurements of absolute optical frequencies and population transfer dynamics*. Phys. Rev. Lett., **95**: 023001, 2005. DOI: 10.1103/PhysRevLett.95.023001. (Cited on pages 104, 105, and 106.)

[165] M.J. Snadden, A.S. Bell, E. Riis, and A.I. Ferguson. *Two-photon spectroscopy of laser-cooled Rb using a mode-locked laser*. Opt. Comm., **125**: 70–76, 1996. DOI: 10.1016/0030-4018(95)00711-3. (Cited on page 104.)

[166] S.A. Lee, J. Helmcke, J.L. Hall, and B.P. Stoicheff. *Doppler-free two-photon transitions to Rydberg levels: convenient, useful, and precise reference wavelengths for dye lasers*. Opt. Lett., **3**: 141–143, 1978. URL: http://www.opticsinfobase.org/abstract.cfm?URI=ol-3-4-141. (Cited on pages 104 and 105.)

[167] A. Banerjee, D. Das, and V. Natarajan. *Precise frequency measurements of atomic transitions by use of a Rb-stabilized resonator*. Opt. Lett., **28**: 1579–1581, 2003. DOI: 10.1364/OL.28.001579. (Cited on pages 104 and 106.)

[168] M.P. Bradley, J.V. Porto, S. Rainville, J.K. Thompson, and D.E. Pritchard. *Penning trap measurements of the masses of ^{133}Cs, $^{87,85}Rb$, and ^{23}Na with uncertainties $\leq$ 0.2 ppb*. Phys. Rev. Lett., **83**: 4510–4513, 1999. DOI: 10.1103/PhysRevLett.83.4510. (Cited on pages 104 and 105.)

[169] D. Das and V. Natarajan. *Precise measurement of hyperfine structure in the $5\,^2P_{1/2}$ state of Rb*. Eur. Phys. J. D, **37**: 313–317, 2006. DOI: 10.1140/epjd/e2005-00313-4. (Cited on page 106.)

[170] A. Banerjee, D. Das, and V. Natarajan. *Absolute frequency measurements of the D_1 lines in ^{39}K, ^{85}Rb, and ^{87}Rb with $\sim$ 0.1 ppb uncertainty*. Europhys. Lett., **65**: 172–178, 2004. DOI: 10.1209/epl/i2003-10069-3. (Cited on page 106.)

[171] U.D. Rapol, A. Krishna, and V. Natarajan. *Precise measurement of hyperfine structure in the $5P_{3/2}$ state of ^{85}Rb*. Eur. Phys. J. D, **23**: 185–188, 2003. DOI: 10.1140/epjd/e2003-00069-9. (Cited on page 106.)

[172] S. Bize, Y. Sortais, M.S. Santos, C. Mandache, A. Clairon, and C. Salomon. *High-accuracy measurement of the ^{87}Rb ground-state hyperfine splitting in an atomic fountain*. Europhys. Lett., **45**: 558–564, 1999. DOI: 10.1209/epl/i1999-00203-9. (Cited on page 106.)

[173] J. Ye, S. Swartz, P. Jungner, and J.L. Hall. *Hyperfine structure and absolute frequency of the ^{87}Rb $5P_{3/2}$ state*. Opt. Lett., **21**: 1280–1283, 1996. URL: http://www.opticsinfobase.org/abstract.cfm?URI=ol-21-16-1280. (Cited on page 106.)

[174] G.P. Barwood, P. Gill, and W.R.C. Rowley. *Frequency measurements on optically narrowed Rb-stabilised laser diodes at 780 nm and 795 nm*. Appl. Phys. B, **53**: 142–147, 1991. DOI: 10.1007/BF00330229. (Cited on page 106.)

SAMENVATTING

Sinds het eind van de jaren tachtig van de vorige eeuw is het mogelijk om neutrale atomen af te koelen en op te sluiten in een val met behulp van laserlicht. Deze technieken hebben geleid tot een wereld aan nieuwe fysica en het vakgebied is dan ook in 1997 bekroond met een Nobelprijs. Het koelen van een gas met behulp van laserlicht is mogelijk doordat volgens de quantummechanica, afhankelijk van de situatie, licht zich voor kan doen als golf of als deeltje, een zogenaamd foton. Als licht van een welbepaalde golflengte (kleur), d.w.z. een welbepaalde energie, op een atoom geschoten wordt en de betreffende energie komt overeen met de overgang van een elektron van de ene toestand naar de andere, dan kan het atoom het foton absorberen. Door deze absorptie zal de impuls van het atoom veranderen met een waarde ter grootte van de impuls van het foton. Door dit vele malen te herhalen oefent het licht een kracht uit op het atoom. Aangezien er zeer veel fotonen nodig zijn om een atoom met een thermische snelheid af te remmen tot stilstand ligt het voor de hand om in dit soort experimenten gebruik te maken van een laser. Het licht uit een laser heeft immers een hoge intensiteit en de fotonen hebben een zeer welbepaalde energie. Met behulp van de moderne lasers is het mogelijk om atomen in een gas bij kamertemperatuur, waar ze een gemiddelde snelheid hebben in de orde van 300 meter per seconde, af te remmen tot enkele centimeters per seconde. Volgens het equipartitiebeginsel uit de statistische fysica kan de spreiding van de kinetische energie van een gas gerelateerd worden aan de temperatuur ervan (zie vgl. (3.33)). Dit betekent dat de afgeremde atomen een lage temperatuur hebben. Een snelheid van een tiental centimeters per seconde komt overeen met een temperatuur van honderd microKelvin. Dat is een tienduizendste graad boven het absolute nulpunt dat ligt op nul Kelvin ofwel $-273{,}15\,^{\circ}\mathrm{C}$. In 2001 werd de Nobelprijs uitgereikt aan de makers van de eerste Bose-Einstein condensaten, een materietoestand waar de temperatuur in de orde van honderd nanoKelvins ligt, een miljardste graad boven het absolute nulpunt. Ook in dit soort experimenten wordt gebruik gemaakt van laserkoelingstechnieken.

Naast de hierboven genoemde verstrooiingskracht die vooral effectief is als de golflengte van het licht in de buurt van de atomaire overgang ligt, kan licht nog een tweede kracht uitoefenen op atomen. De zogenaamde dipoolkracht maakt gebruik van de polariseerbaarheid van atomen die zich in een elektrisch veld bevinden. Deze polariseerbaarheid zorgt voor een verschuiving van de elektronische energieniveaus van een atoom, de zogenaamde Stark-verschuiving. Deze verschuiving is afhankelijk van de verstemming van het veld ten opzichte van de atomaire overgang en de intensiteit van het veld. Een gradiënt in het veld

levert een gradiënt op in de potentiaal en daarmee een kracht. Aangezien licht een elektromagnetisch veld is, betekent dit dat atomen gevangen kunnen worden met behulp van laserlicht van de juiste golflengte. De vergelijkingen (3.15) laten zien dat de kracht aantrekkend is als de frequentie van het licht lager is dan die van de atomaire overgang en afstotend bij een hogere frequentie. Verder blijkt uit deze vergelijkingen dat de fotonverstrooiing sneller afvalt als functie van de verstemming dan de diepte van de optische potentiaal. Dus op middelgrote tot grote verstemmingen is het mogelijk om atomen te vangen in een gefocusseerde laserbundel met een negatieve verstemming (zie fig. 3.1 voor een afbeelding van de potentiaal). Vallen die op dit principe gebaseerd zijn en een verstemming van een paar tot enkele honderden nanometers hebben, worden ververstemde vallen (far-off-resonance traps (FORTs) in het Engels) genoemd. De wolk van atomen gevangen in een FORT heeft een lengte van ongeveer een halve millimeter en een straal van een tiende millimeter (zie de voorkant van dit proefschrift). Het nadeel van een FORT is dat er geen koeling in deze val plaatsvindt en aangezien een FORT typisch enkele honderden tot enkele duizenden microKelvin diep is betekent dit dat er zeer weinig atomen uit een gas op kamertemperatuur gevangen kunnen worden.

Om dit probleem het hoofd te bieden wordt de FORT geladen met atomen uit een ander type val waarin wel koeling mogelijk is. Dat is de magneto-optische val of MOT (magneto-optical trap in het Engels), de meest gebruikte val voor neutrale atomen. Deze val bestaat uit zes laserbundels, steeds twee tegenovergesteld gerichte bundels per coördinaat-as, en een magnetisch veld met een lineaire gradiënt in de ruimte. Hierin kunnen atomen worden gevangen en gekoeld tot een temperatuur van ongeveer honderd microKelvin, wat overeenkomt met een snelheid van zo'n twaalf centimeter per seconde (zie fig. 4.25).

Vooralsnog wordt bij de meeste experimenten met koude atomen gebruik gemaakt van lasers met een continue intensiteit. Al sinds het ontstaan van de laser in de jaren zestig wordt er echter veel onderzoek gedaan naar en met gepulste lasers. Voordelen van hedendaagse gepulste lasers zijn het hoge outputvermogen (alle energie die er anders continu uitstroomt kan nu opgespaard worden en in een puls naar buiten gebracht worden) en de extreem korte duur van de pulsen. Heden ten dage zijn pulsduren van enkele femtoseconden, d.w.z. een biljardste deel van een seconde, gemeengoed. Dergelijke korte pulsen hebben als voordeel dat processen die op deze tijdschalen plaatsvinden kunnen worden gevolgd door "foto's" te maken met behulp van het laserlicht. Ook probeert men bijvoorbeeld om hiermee optische switches te maken voor glasvezelcommunicatie. In onze opstelling wordt gebruik gemaakt van een laser die pulsen genereert van ongeveer een picoseconde, d.w.z. een biljoenste seconde.

De achterliggende gedachte voor het onderzoek beschreven in dit proefschrift is het maken van een atoomval met gepulst laserlicht. Met behulp van moderne frequentieverdubbelingskristallen zou het mogelijk kunnen zijn om andere

chemische elementen te vangen, waarvoor nog geen lasers beschikbaar zijn. Ook zou een gepulste val atomen efficiënter kunnen vangen. Beschouw hiervoor een atoom dat zich bevindt tussen twee tegengesteld gerichte gepulste laserbundels. Het laserlicht heeft een dusdanige intensiteit, verstemming en pulsduur dat een atoom dat geraakt wordt door de puls volledig in de aangeslagen toestand terecht komt. Zo'n puls wordt een π-puls genoemd. De timing van de pulsen van beide kanten is zodanig dat de pulsen in het midden van de opstelling overlappen. Hierdoor zal een atoom dat links van het midden beweegt eerst geraakt worden door een puls uit de linker bundel (zie figuur 2.1a) en in de aangeslagen toestand terecht komen door de absorptie van een foton. De impulsverandering door deze absorptie zorgt ervoor dat snelheid van het atoom in de richting naar het centrum van de val toeneemt. Aangezien de tijd tussen twee opeenvolgende pulsen korter is dan de levensduur van de aangeslagen toestand is het atoom nog in die toestand als de puls van de andere kant komt (zie fig. 2.1b). Omdat ook dit een π-puls is, zal deze het atoom in één keer naar de grondtoestand brengen. Dit proces, gestimuleerde emissie, gebeurd onder uitzending van een foton in dezelfde richting als de puls, d.w.z. van het centrum af. De impulsoverdracht behorend bij dit proces levert wederom een verandering van de snelheid in de richting van het centrum op. De impuls van het atoom in de richting van het centrum is toegenomen met twee keer de fotonimpuls. Het atoom bevindt zich nu weer in de grondtoestand en is weer klaar voor de volgende set pulsen (zie fig. 2.1c). Uiteraard geldt dit proces, *mutatis mutandis*, ook voor atomen die zich ter rechter zijde van het centrum bevinden. Kortom, ongeacht de locatie van de atomen, zullen deze altijd een kracht ondervinden die gericht is naar het centrum van de opstelling, daar waar de pulsen overlappen. Aangezien er niet hoeft te worden gewacht op het spontane verval van de aangeslagen toestand naar de grondtoestand, hetgeen relatief lang duurt, is deze methode zeer efficiënt voor het vangen van atomen.

Als opstap richting het uitvoeren van bovengenoemd experiment hebben wij besloten om een FORT te gebruiken omdat dit een compact en relatief eenvoudig systeem is. Bovendien kan onze gepulste laser eenvoudig schakelen tussen continue en gepulste output. Daarnaast verwachten we dat als het bovenstaande compressieschema werkt, we dit onmiddellijk zullen zien aan de grootte van de FORT wolk. Het werk dat in dit proefschrift beschreven wordt omvat een onderzoek naar verschillende eigenschappen van atomen gevangen in een FORT gemaakt met een continue laser en atomen in een gepulste FORT. Voor onze experimenten hebben we gebruik gemaakt van de twee in de natuur voorkomende isotopen van rubidium, ^{85}Rb en ^{87}Rb. Rubidium is bij kamertemperatuur een zacht, zilverkleurig metaal. Het reageert zeer heftig met zuurstof en water en wordt dan ook in een inerte argon atmosfeer bewaard.

Dit proefschrift bestaat uit de volgende onderdelen. Na een inleiding en een motivatie worden in hoofdstuk 3 de theoretische concepten van het vangen

en koelen van atomen in optische vallen uitgelegd. In hoofdstuk 4 wordt de opstelling waarmee de experimenten gedaan zijn uitvoerig behandeld, te beginnen met de vacuümopstelling. De experimenten worden in een ultrahoog vacuüm gedaan, de druk is er twaalf ordes van grootte lager dan de omgevingsdruk. Rubidiumdamp wordt vanuit een oventje de vacuümkamer ingelaten (zie fig. 4.1). De lasersystemen met bijbehorende optica zijn de volgende onderdelen die beschreven worden. Naast enkele basisgegevens wordt uitgelegd hoe de polarisatiespectroscopie-techniek gebruikt wordt om de frequentie van het licht van de diodelasers te stabiliseren. Deze relatief nieuwe en nog weinig gebruikte techniek biedt enkele grote voordelen in vergelijking met de traditionele verzadigingsspectroscopie en vergelijkbare technieken. Daarna wordt de optica beschreven die gebruikt is om de afbeeldingen van de atomen in de MOT en de FORT te maken, gevolgd door een beschrijving van de door ons ontwikkelde bundelsluiters op basis van modeltreinwissels. Ook wordt de werking uitgelegd van het zelfgeschreven aansturingsprogramma. Met dit programma is het mogelijk om met goedkope hardware toch nauwkeurige submilliseconde timing van de verschillende experimentstadia te realiseren. Dit wordt mogelijk gemaakt door gebruik van een aangepaste Linux-kernel, welke strikte timingcondities garandeert en alle overige processen op de computer een ondergeschikte rol geeft. Dit leidt tot een gemengd systeem waarin tijdkritische applicaties kunnen draaien naast gewone programmatuur. Tenslotte worden metingen van enkele karakteristieke waarden van onze MOT beschreven.

In de daaropvolgende hoofdstukken komen vervolgens verschillende aspecten van de continue en gepulste FORTs aan de orde. Allereerst wordt in hoofdstuk 5 beschreven hoe het aantal atomen dat in een FORT geladen wordt afhangt van het vermogen van de FORT laserbundel. Dit blijkt in ons geval niet te verklaren door gebruik te maken van een eenvoudig model waarin wordt aangenomen dat alle atomen die zich binnen het FORT volume bevinden en die een energie hebben die kleiner is dan de valdiepte, zullen worden gevangen. Dit is niet geheel verrassend aangezien dit eenvoudige model geen recht doet aan enkele experimentele randvoorwaarden en de complexe processen zoals het botsen van gevangen atomen onderling en de in- en uitflux van atomen in het FORT volume. Ook hebben we bestudeerd hoe het aantal atomen dat in een FORT wordt geladen afhangt van de laadtijd. Hieruit blijkt dat indien de timingcondities zorgvuldig gekozen worden er zelfs meer atomen in een gepulste FORT geladen kunnen worden dan in een continue FORT. Daarnaast blijkt dat twee-deeltjesverval domineert tijdens het laden.

De levensduur van de FORT, d.w.z. het aantal atomen in de val als functie van de tijd is ook een belangrijk gegeven (zie fig. 5.6). Atomen kunnen uit de val verdwijnen door bijvoorbeeld botsingen met atomen die niet gevangen zijn. Ook het verstrooien van fotonen uit de FORT laser leidt tot verliezen. Het blijkt dat deze verliezen voor een continue FORT niet afhankelijk zijn van het vermogen van de

FORT laser. Voor een gepulste FORT zien we echter dat vanaf een bepaald vermogen deze verliezen toenemen. Dit is zoals verwacht omdat bij een gepulst experiment de fractie van het aantal atomen dat zich in de aangeslagen toestand begint sterker stijgt dan in het continue geval. Naast voornoemde verliezen zijn er ook twee-deeltjes verliezen mogelijk. Deze worden onder andere veroorzaakt door fotoassociatie, het proces waarbij twee gevangen atomen door middel van een foton aan elkaar gebonden worden en een molecuul vormen. Doordat moleculen een andere interne structuur hebben dan losse atomen, kunnen ze niet in de FORT of MOT gevangen worden. Het golflengtegebied waarin onze experimenten gedaan zijn, bevat veel mogelijkheden voor zulk soort processen. De levensduur van de FORT is dan ook sterk afhankelijk van de golflengte. Verder blijkt dat de twee-deeltjesverliezen niet afhankelijk zijn van het vermogen van de laser.

Tenslotte is de temperatuur van de atomen in de FORT bepaald. Hiertoe wordt de val geladen, waarna de laserbundel gedurende een variabele tijd wordt uitgeschakeld. Gedurende deze expansietijd zullen de atomen uit elkaar vliegen (en langzaam naar beneden vallen), hoe heter de wolk, hoe sneller de expansie is. Vervolgens wordt de wolk atomen met behulp van de MOT laserbundels belicht. Het door de atomen uitgezonden fluorescentielicht wordt door een CCD camera opgevangen. Uit de toename van de grootte van de wolk als functie van de expansietijd kan de temperatuur worden bepaald (zie de figuren 5.9 en 5.10). De temperatuur van de atomen in de FORT blijkt een vaste fractie van de diepte van de val te zijn, hoe dieper de val, hoe heter de atomen.

In hoofdstuk 6 wordt beschreven wat er gebeurt met atomen in een FORT waarvan de valdiepte een klein beetje gemoduleerd wordt. Het is namelijk zo dat atomen in FORT heen en weer bewegen met een frequentie die afhangt van de grootte van het focus van de laser bundel. Hoe kleiner het focus, hoe hoger de oscillatiefrequentie. Als nu de frequentie van de valdiepte-modulatie twee maal de typische frequentie is van de atomen, dan zal de modulatie leiden tot een exponentiele groei van de energie van de atomen, de zogenaamde parametrische excitatie. Door deze excitatie zullen atomen zoveel energie winnen dat ze uit de val ontsnappen. Door de modulatiefrequentie te variëren en te zoeken naar een dip in het aantal atomen in de val kan de grootte van het focus van de bundel bepaald worden. Hierbij moet wel rekening worden gehouden met het feit dat een FORT geen harmonische val is en de frequentie waarmee een atoom in de val oscilleert afhangt van zijn energie. Hoe hoger de energie, hoe lager de frequentie (zie figuur 6.1). Uit de metingen blijkt verder dat de temperatuur van de atomen in de gemoduleerde val afhangt van de frequentie. Bij frequenties vlak onder de verwachte excitatiefrequentie is de temperatuur namelijk hoger, terwijl bij nog wat lagere frequenties de wolk kouder is geworden. Dit kan verklaard worden door de anharmoniciteit van de FORT. De atomen met de hoogste energie hebben immers de laagste frequentie. Als deze dus verwijderd worden zal de gemiddelde temperatuur van de atomen in de val dalen. Bij iets hogere

frequenties worden juist de laagenergetische atomen onderin de val opgewarmd met als gevolg een stijging van de gemiddelde temperatuur. Om een en ander beter te kunnen begrijpen hebben we een computersimulatie gemaakt van het proces van parametrische excitatie. De simulatie reproduceert de resultaten van de metingen goed. Bovendien blijkt dat ongeacht de frequentie er altijd atomen zijn die gekoeld worden. Op de excitatiefrequentie is echter het aantal atomen dat verwarmd wordt vele malen groter (zie fig. 6.6).

In een vergelijkbaar experiment hebben we de modulatie niet klein gehouden maar juist opgevoerd naar 100 %, de val werd dus met een in te stellen frequentie aan en uit gezet. Dit is in principe een zeer traag gepulste val en is daarom relevant voor ons onderzoek. Beschouw het volgende model voor dit experiment. Een atoom dat op zeker moment gevangen is in de val zal slechts gevangen blijven indien zijn snelheid (en dus zijn temperatuur) zodanig is dat hij na een halve periode, als de val weer aan gaat, aan de overkant van de val is. Is de snelheid groter dan deze maximum snelheid, dan heeft hij het gebied van de val verlaten voordat de val weer aan is en wordt niet meer gevangen. Uiteraard is het ook zo dat atomen met een snelheid die twee keer langzamer is dan de maximale invangsnelheid, gevangen zullen worden omdat de val dan twee keer uit en weer aan is geweest in de tijd die het atoom nodig had om de andere kant van de val te bereiken (dit geldt natuurlijk voor alle snelheden die een geheel aantal maal een half keer de maximum invangsnelheid zijn). De metingen laten echter zien dat de frequentie waarbij atomen worden gevangen significant hoger ligt dan uit het bovenstaande eenvoudige model kan worden afgeleid (zie fig. 6.7). De oorzaak hiervan is niet duidelijk. De resultaten van de simulaties vertonen echter wel het verwachte gedrag, daarom vermoeden we dat de oorzaak van deze discrepantie in het experiment zit.

Tenslotte wordt in hoofdstuk 7 gekeken naar het aantal atomen dat in een FORT gevangen wordt als functie van de polarisatie van het licht uit de FORT laser (zie fig. 7.4). Normaliter worden FORTs gemaakt met lineair gepolariseerd licht. Het is ook mogelijk gebleken om een FORT te maken met circulair gepolariseerd licht. Uit onze metingen blijkt echter dat dit niet geldt voor een gepulste FORT wanneer de golflengte van het licht tussen de twee D-lijnen van het rubidium atoom ligt. Voor golflengtes boven de D_1 lijn geldt deze beperking niet. Dat komt doordat de interne structuur van een atoom, de oorzaak van de polarisatieafhankelijkheid, er minder en minder toe doet naarmate de verstemming van het licht groter wordt. Verder valt op dat het aantal atomen dat gevangen wordt in de gepulste val minder hoog ligt dan in de continue val. Ook de "dalen" tussen de gebieden met lineair gepolariseerd licht blijven dieper in het gepulste geval. Dit kan verklaard worden door de veel grotere fotonverstrooiing van de gepulste laser, veroorzaakt door de grote piekintensiteit van de pulsen.

CURRICULUM VITÆ

Op 25 november 1977 werd de auteur van dit proefschrift geboren in de stad Harderwijk. Het Voortgezet Wetenschappelijk Onderwijs werd doorlopen aan het Christelijk College Groevenbeek te Ermelo in de jaren 1990 tot 1996. In september 1996 begon hij aan zijn studie Natuurkunde aan de Universiteit Utrecht, welke in juni 2002 succesvol werd afgerond met het behalen van het doctoraaldiploma in de Experimentele Natuurkunde op het onderwerp "*Building a Rubidium MOT Using Polarisation Spectroscopy Stabilised Diode Lasers*". Hierbij werd hij begeleid door drs. Erik van Ooijen en prof.dr. Peter van der Straten uit de groep Atom Optics & Ultrafast Dynamics.

Aansluitend werd onder leiding van de hoogleraren Jaap Dijkhuis en Peter van der Straten binnen dezelfde groep begonnen met het onderzoek resulterend in dit proefschrift. Gedurende de periode 2002-2006 was de schrijver lid van de Debye AIO Commissie, waarin hij in de laatste drie jaar de functie van secretaris bekleedde. Behalve op de verschillende jaarlijkse conferenties in eigen land, werd het onderzoek beschreven in dit proefschrift ook gepresenteerd op de Young Researcher Meeting 2005 van het Cold Molecules netwerk in Freiburg, Duitsland.

Gedurende het promotieonderzoek begeleidde Lennart een viertal studenten voor hun klein onderzoek of bachelor onderzoek en een groot-onderzoekstudent. Ook hebben twee koppels studenten enkele dagen met zijn opstelling metingen verricht voor een van hun vakken. Verder gaf hij werkcollegeonderwijs voor het vak Atoom- en Molecuulfysica en begeleidde hij de cursussen Programmeren in LabVIEW, Programmeren in Mathematica en Inleiding in het Computergebruik. Daarnaast heeft hij meegewerkt aan het project voor het schrijven van aansturingssoftware voor de datalogger van de Wetenschapswinkel Natuurkunde.

DANKWOORD

En zo is er dan een einde gekomen aan een tijdperk(je). Na jaren van hard werken ligt hier het resultaat van de leuke, minder leuke, lange en soms zelfs korte dagen die een promovendus in lab en studeerkamer doorbrengt. Ik heb veel geleerd. Over fysica, maar zeker ook over mezelf.

Hoe contactgestoord fysici volgens de vooroordelen ook zouden zijn, een promotieonderzoek doe je niet alleen. De steun van velen is onontbeerlijk en zoals generaties promovendi voor mij, hoop ik dan ook dat ik op de volgende pagina's niemand vergeten ben.

Zonder mijn promotoren Jaap Dijkhuis en Peter van der Straten was dit boekje er überhaupt niet geweest. Dank jullie wel voor alle hulp, discussies, tips, goede ideeën, nou ja, teveel om op te noemen. Ik weet dat ik vaak eigenwijs was, zoals een goed fysicus betaamt, maar dat wil niet zeggen dat ik niks met jullie aanwijzingen deed. Peter, met jou wil ik nog wel eens een oventje van nieuw rubidium voorzien, met of zonder brandgaten en -wonden. Op het vlak van computersimulaties heb ik veel van je geleerd en je hebt me zelfs weten te overtuigen van de kracht van FORTRAN, daarmee *"kunnen we eindelijk alles uitrekenen!"*. Voor een shotje motivatie kun je altijd bij Jaap terecht. Zelfs als je zelf niet tevreden bent over een resultaat zorgt hij er wel voor dat je toch nog *"goud in handen hebt"*.

Peter van Capel, kamergenoot vanaf het begin, zelfs nog voordat je zelf het pad van de promovendus ging bewandelen. Bedankt voor je gezelligheid, relativeringsvermogen en heldere kijk op zowel de fysica als de politiek. Ik hoop dat je werk maakt van *Deskundigen nu!*, dat komt het vaderland vast en zeker ten goede. Veel succes bij TNO, waar je hopelijk minder uren maakt dan ik hier van je gewend ben.

Tijdens een promotieonderzoek komen er heel wat studenten voor korte of langere tijd in je lab. Robert, als groot-onderzoekstudent kwam je binnen. Jouw bijdrage aan mijn onderzoek is groot geweest, ook later toen je collega werd. Je hebt mijn muzikale opvoeding met veel plezier en toewijding ter hand genomen. Bijna elke week lag er wel een nieuw CDtje op mijn bureau dat "echt heel goed" was, met de te verwachten devaluatie tot gevolg. Toch zouden Nada Surf, Tanzwut, Moss en vele anderen zonder jou niet zo makkelijk hun weg naar mijn CD-rek gevonden hebben. Om maar in jouw stijl te blijven (met dank aan Bob):

> You talk of situations,
> Listen CDs, repeat quotations,
> Draw conclusions on the wall.

Veel succes met jouw laatste loodjes! Voor hun klein onderzoek en bacheloronderzoek waren er Charlotte Rosenbaum, Martien *"Spiderwoman"* den Hertog, Erik *"Erikje"* Bakker en Thomas *"Spartasjaal"* Habets. Allemaal bedankt voor jullie bijdrage aan de Groep Karssen, zowel qua fysica als voor de gezelligheid. Dat geldt ook voor de verschillende studenten die voor een vak enkele dagen metingen kwamen doen.

Natuurlijk was ik niet de enige promovendus die op de tweede van het Ornsteinlab rondliep. In den beginne waren daar Michiel, in wiens opstelling de kaboutertjes elke nacht de spiegels verdraaiden; Dries die altijd wist wat er de avond tevoren op Discovery was uitgezonden; Erik die liever over iets anders dan natuurkunde praatte (vrouwen?). We weten heus wel dat je aan de andere kant van de aardkloot stiekem toch over natuurkunde praat. Otto en Dmitry, jullie waren van de andere kant van de gang. Maar... ik eigenlijk ook... The new team consisted of Shan, who drank beer just to humour Dmitry (and even liked it a little); and of Louise who is always in for a drink, a dance or wearing strange hats. Daarnaast was er Richard, de man van reizen, steeksleutels en satésaus. En ook degene die het aandurfde om zijn Italiaanse prof te vertellen dat die zijn sportwagen maar moest verkopen als de financiering krap werd. En tenslotte is er Silvio, für wen alles immer funktioniert, weil es für Robert und mich immer arbeiten soll. Het is wel spannend om een maand lang een huisgenoot te hebben die zijn eten met een bijl te lijf gaat. Ook voor jullie geldt: veel succes met het temmen der atomen! Marijn, als laatste der Mohikanen Jaaps, veel succes met het ontwarren van je nanodraden.

Soms waren ook postdocs van de partij, van wie ik veel geleerd heb: echte muntthee drinken van Driss, dat het altijd tijd voor bier is van Dmitry Turchinovich en van Johnny dat "even snel" niet altijd ideaal is. Maar wel snel!

Zonder de hulp van onze technici Frits, Paul, Cees, Jitse en Hans zou het onmogelijk (en bijzonder ongezellig) geweest zijn om dit project tot een goed einde te brengen. Op het gebied van elektronica, constructie, vacuüm en hulp bij laserproblemen zijn jullie de besten! Clarien, Henk, Nico en Jan van 't cryogeen, en de IGF-technici ook dank voor jullie bijdragen aan mijn onderzoek.

> I count myself in nothing else so happy
> As in a soul remembering my good friends
>
> (W. Shakespeare, *Richard II* act 2, sc. 3)

Roel & Jaimi, Rob & Linda, samen zijn we tot grote hoogten geklommen. Luisterend naar Neil, Bob, Kurt en al die andere helden hebben we van vele biertjes genoten, maar over het belang van kwaliteit boven kwantiteit zullen we het wel nooit eens worden.

Paul & Annemiek, Erwin & Suzanne, ook jullie bedankt voor de hechte vriendschap en goede raad op gezette tijden. En natuurlijk ook voor de gezellige klimen eetavondjes, dat kan nu weer wat vaker.

Niels, ook al zien we elkaar noodgedwongen maar eens in de paar jaar, afstand verandert gelukkig niks aan vriendschap. 't Is mijn beurt, ik weet het.

Cindy, het was heerlijk om je te leren kennen. We hebben een heel fijne tijd gehad. Lekker van elkaars cultuur genieten en lachen om de onverwachte verschillen. Ik heb in mijn tweede vaderland jeugdherinneringen teruggevonden en vele nieuwe gemaakt. Dankzij u heb ik leren genieten van goei pinkes en oesters mei champagne. En ge weet, tegen mij hoeft ge geen u te zeggen.

Chère Eva, toi aussi merci pour tout. Nous avons eu beaucoup de plaisir en faisant du Rock & Roll ou en parlant Français. Hopelijk krijg ik in Rwanda weer de kans om m'n Frans bij te spijkeren. Ik wens je heel veel plezier met je nieuwe baan.

Voor een goede start in het leven is het belang van een warm nest niet te onderschatten. Opa en oma Hagoort, oma Karssen, jullie hebben altijd met veel interesse mijn leven gevolgd en mij gestimuleerd er het meeste uit te halen. Jammer dat jullie er niet meer allemaal zijn om dit mee te mogen maken. Papa en mama, jullie adviezen en de niet aflatende steun hebben veel voor me betekend in de soms moeilijke tijden. Wat er ook gebeurde, er was altijd een plek om bij te komen en alles los te laten. Lieve zusjes, jullie ook bedankt voor de vele gezellige telefoontjes en chats. Ik denk dat we elkaar de afgelopen jaren nog beter zijn gaan kennen.

Lieve Lean, zo hoor je vier jaar niks van elkaar en zo kun je met een e-mail en een SMS ineens weer contact hebben. En ben je na acht jaar weer samen. Leuk, hoe levens soms kunnen lopen. Je vrolijke lach en nuchtere kijk op de wereld zijn goud waard. Ik ben blij dat we samen de eindspurt gelopen hebben. Nu is er weer tijd voor (meer) leuke dingen. En nog even en dan hebben we naast een doctor ook een dokter in de zaal.

COLOPHON

This thesis was typeset with LaTeX 2ε using Hermann Zapf's *Palatino* and *Euler* type faces (Type 1 PostScript fonts *URW Palladio L* and *FPL* were used). *Bera Mono* was used for monospaced text. The PDF version was generated using pdfLaTeX.

The typographic style was inspired by Robert Bringhurst's ideas on typography as worked out in André Miede's ClassicThesis package (available for LaTeX via CTAN as "`classicthesis`"), with many customisations by the author.

The figures were made with the Interactive Data Language (IDL), XFig, POV-Ray and Mathematica using routines written by the author. BibTeX was used to generate the bibliography. The cover was designed in Adobe's Photoshop CS3. The images on the back cover are those of the FORT temperature measurement of Fig. 5.9 on page 75 showing the cloud of atoms after increasing expansion times. The image on the front cover is an enlargement of the central section of the first shot.

The manuscript was printed by PrintPartners Ipskamp, Enschede.